Direction-sensitive direct dark matter search experiment with a gaseous TPC

HIRONOBU NISHIMURA

DEPARTMENT OF PHYSICS, FACULTY OF SCIENCE,
KYOTO UNIVERSITY

Kitashirakawa Oiwake-cho, Sakyo-ku, Kyoto, 606-8502, Japan

This thesis was submitted to the Department of Physics, Graduate School of Science, Kyoto University in partial fulfillment of the requirements for the degree of Doctor of Philosophy in physics.

JANUARY 5, 2009

Abstract

A lot of observational results indicate the existence of dark matters in the universe. Weakly Interacting Massive Particle (WIMP) is one of the leading candidates of the dark matter. Some theories predict that WIMPs can be directly detected via elastic scatterings with nuclei in detectors. Many dark matter search experiments have been performed so far and one of them claimed the detection of the dark matter signal, but no experiments have never suported its result. We need other methods which should provide more reliable signals of the dark matter. The direction-sensitive method is one of them.

NEWAGE is one of the direction-sensitive direct dark matter search projects. A time projection chamber with a micro-pattern gas device (μ-TPC) was developed as a proto type direction-secsitive dark matter detector, (NEWAGE-0.3a detector). We measured the performance of the NEWAGE-0.3a detector and operated it in an undergroound labolatory. We performed a dark matter search run after background studies and an optimization of operation parameters. We obtained a 90% C.L. spin-dependent WIMP-proton cross-section limit of 5.4×10^3pb for a WIMP mass of 150 GeV/c^2 with a directional analysis.

Contents

Chapter 1

Introduction

Recent results from Cosmic Microwave Background (CMB)[1], Large Scale Structure (LSS) and Type Ia supernovae observations have established a standard model of cosmology. The model favors a flat universe consisting of more than 70 % dark energy, about 22 % dark matter, and the remainder of the ordinary (Baryon) matter, as shown in Figure 1.1. Answering
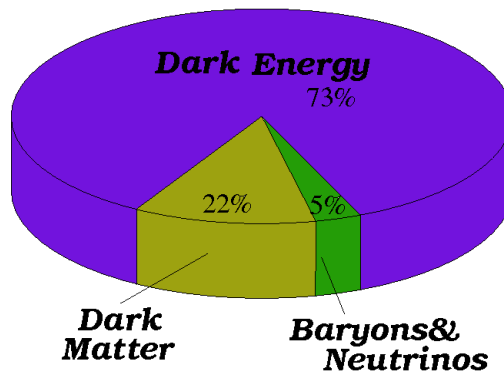
Figure 1.1: Composition of the universe. The universe consists of 73% dark energy, 22% dark matter and 5% ordinary matter.

the questions "what is the dark energy" and "what is thw dark matter" became one of the most challenging tasks for physicists in recent year. This thesis and underlying experiment are intended as an exploration of the dark matter problem. A discovery of the dark matter particle will become both a strong support of the cosmological observations and predictions, and a piece of evidence for new physics beyond the standard model of the particle physics.

In this chapter, we first introduce the problem of the missing mass in the universe and evidence from cosmological observations that suggest a large amount of matter in the

universe is dark. We then describe some theoretical explanations and models that may be used to explain the mysterious dark matter problem focusing on candidates for the dark matter.

1.1 Dark matter problem

Existence of the dark matter is suggested by some astrophysical observations; cosmological observations and its theory, galaxy claster observcations, galaxy rotation curves, and so on. We review some of them and a distribution model of the dark matter in this section.

1.1.1 Cosmological dark matter

In recent years, cosmological parameters such as the Hubble constant H_0, the mass density parameter $\Omega_{\rm m}$, the baryon density parameter $\Omega_{\rm b}$ and the total density parameter Ω_0 have been precisely measured. In the cosmological model, the density parameters are defined as the ratio of the density to the critical density $\rho_c = 1.05 \times 10^{-5} h^2$ GeVcm^{-3}, as shown in Eq.(1.1).

$$\Omega_i \equiv \frac{\rho_i}{\rho_c} = \frac{8\pi G}{3H_0{}^2}\rho_i \tag{1.1}$$

Here $h \equiv H_0/(100[{\rm km/sec/Mpc}])$ and $G = 6.71 \times 10^{-39} \hbar c({\rm GeV/c}^2)^{-2}$ is the gravitational constant. The total density parameter of the Universe, Ω_0, is directly related to its present curvature. A flat Universe has $\Omega_0 = 1$, an open Universe has $\Omega_0 < 1$, and a closed Universe has $\Omega_0 > 1$. These parameters were restricted by cosmic microwave background (CMB) radiation measurements, observations of the Type Ia supernova, and the cluster galaxies.

The CMB radiation is the radiant left over from the big bang when the universe was cool. The radiation is highly uniform across the sky, but there are tiny fluctuations (also called anisotropy) associated with fluctuations of the matter density in the early universe. The NASA's COBE satellite firstly detected this anisotropy in 1992, and the Wilkinson Microwave Anisotropy Probe (WMAP) reported a more accurate result [1]. The WMAP results determined the cosmological model parameters as the matter density of the universe $\Omega_{\rm m}h^2 = 0.1326 \pm 0.0063$, and the Hubble constant $h = 0.719 \pm 0.026$. In addition, the WMAP data and the deuterium observation data agree on the baryon density is

$$\Omega_{\rm b}h^2 = 0.02273 \pm 0.00062, \tag{1.2}$$

based on the Big Bang nucleosynthesis(BBN) [2]. This means that non-baryonic dark matter is required beyond any doubt. The measurements and observations of the distance-redshift relation of Type Ia supernovae found that the expansion of the Universe is accelerated. This acceleration suggests an unknown type of energy, dark energy. The Type Ia supernovae observation data [3] suggests a total energy density Ω_Λ, which is the dark energy, around 0.7 and the mass density Ω_m around 0.3 for a flat $(\Omega_\Lambda + \Omega_m = 1)$ cosmology.

The gravitational instability and small fluctuations of the initial density field of the Universe cause the formation of a large-scale structure and the galaxy distribution in today's Universe. Thus the measurement of the distribution of galaxy clusters can be used to determined the mass density of the universe, and this is particularly investigated by the Sloan Digital Sky Surveys (SDSS)[5]. Combined with the CMB anisotropy measurement by WMAP, SDSS results favor a low-density Universe with $\Omega_m \sim 0.30 \pm 0.04$.

Combining the high-redshift supernova survey, the galaxy cluster observations and the cosmic microwave background measurements, the normalized mass and energy density Ω_m

and Ω_Λ nicely converge in the cosmological parameter space as shown in Fig. 1.2, which indicates an inflationary and flat cosmological models.
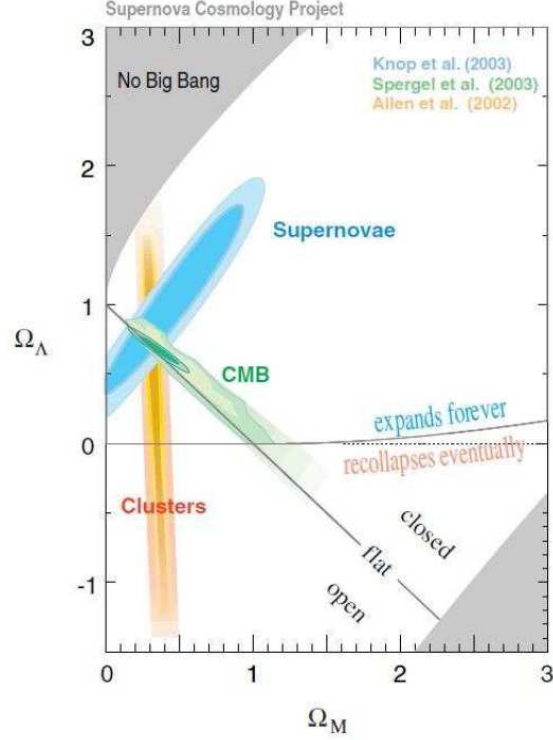
Figure 1.2: Cosmological parameter space from high-redshift supernova survey [3], galaxy cluster observation [4] and cosmic microwave background measurement.

1.1.2 Galaxy rotational curves and dark matter

The clearest evidence for the existence of the dark matter is observed by the difference between the matter distribution implied by the observed luminosity and that implied by the rotation velocity, v_c, of the spiral galaxies.

The rotation velocity distribution of a spiral galaxy expected from Kepler's law is

$$\frac{[v_c(r)]^2}{r} = G\frac{M(r)}{r^2} \tag{1.3}$$

where r is the radial distance from the center of the galaxy, and $M(r)$ is the total mass within the radius r. Since the orbital velocity can be measured by the Doppler shifts of the spectrum of the stars, the 21 cm line of the HI gas (neutral hydrogen gas) and 3.6 mm line of the CO gas, the mass distributions of the spiral galaxies are estimated from Eq.(1.3). On the other hand, the luminous matter is found concentrated near the center of the galaxy. If the total mass of the galaxy concentrate near the luminous core of the galaxy, v must fall like $r^{-1/2}$. The measured velocities, however, remain constant out to the distance as far as

can be measured in almost all cases. This implies that $M(r) \propto r$ at a large radius, and there exists a large amount of matter of a non-luminous mass which exceeds the luminous one.

Fig. 1.3 shows the rotational curve of the spiral galaxy NGC6503 [6]. The luminous disk extends no further than approximately 5 kpc from the center of the galaxy. If the luminous matter concentrated within this radius, the rotational curve would drop at large radius. From the discrepancy between the observed rotational curve and that expected from the luminous disk and gas, the existence of a dark halo is inferred. Based on this method, the typical mass density of the dark halo is estimated to be

$$\Omega_{\text{halo}} \geq 0.1 \tag{1.4}$$

On the other hand, the mass density of the luminous part of the galaxy is estimated to be,

$$\Omega_{\text{luminous}} \leq 0.01 \tag{1.5}$$

Thus the comparison between Eq. (1.4) and (1.5) indicates that the dark matter exists at the scale of a single galaxy. Some searches for baryonic non-luminous objects appeared that there are some non-luminous mass in the galaxies but not enough to explain the galactic rotations.
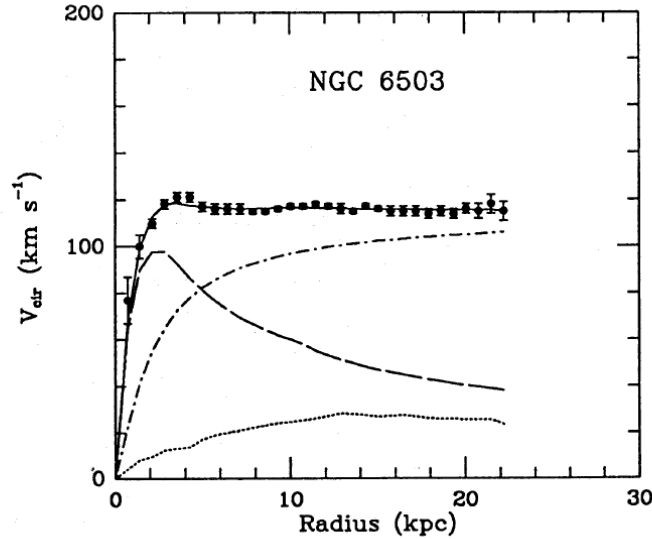
Figure 1.3: Rotation curve of the spiral galaxy NGC6503 [6]. The points indicate the measured rotation velocities as a function of the distance from the galactic center. The dashed and dotted curves are the contribution to the rotation velocity from the observed disk and gas, respectively. The dash-dotted curve is the contribution from the dark halo. The solid line is a sum of them.

1.1.3   Local halo density and isothermal halo

Although the determination of a halo model in our Galaxy is currently a very active topic in astrophysics, both a local halo density, ρ_0, and the dark matter velocity distribution

represent a significant systematic uncertainty. Therefore, the dark matter direct detection community uses the simplest reasonable model, the isothermal halo model.

In determining ρ_0 and v_0, the galactic rotational curve is the most important observational quantity. The rotational curve of our Galaxy cannot be measured with a same precision as that of an external spiral galaxy, for instance NGC6503 in Fig. 1.3. However, assuming that our Galaxy is an ordinary spiral galaxy like NGC6503, the rotation velocity of our Galaxy increases linearly from zero at the center to roughly $v_{\rm c}$ =220 km/s in the solar neighborhood and remains roughly flat all the way out to $\sim$ 25 kpc [7]. The observed rotational curve for our Galaxy is shown in Fig. 1.4.

In the isothermal halo, the shape of the rotational curve could be explained by assuming that the density distribution of the dark halo is

$$\rho(r) = \frac{\rho_0}{1 + r^2/r_0{}^2} \tag{1.6}$$

where ρ_0 and r_0 are fitting parameters. Using the observed rotation velocity in the solar neighborhood, the local density of the halo dark matter is estimated to be

$$\rho(r) \sim 0.3 \text{GeVc}^{-2}\text{cm}^{-3} \tag{1.7}$$

with an uncertainty of a factor two or even more [8].

The following values are adopted in this thesis as in many dark matter search experiments.

$$\rho(r) \sim 0.3 \text{GeVc}^{-2}\text{cm}^{-3} \tag{1.8}$$
$$v_0 \sim v_{\rm c} \sim 220 \text{km/s}$$
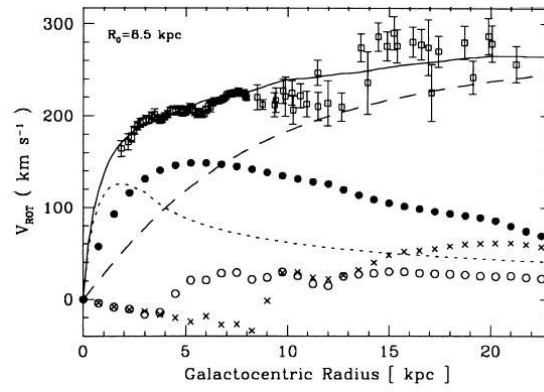
Figure 1.4: Rotation curve of our Galaxy [7]. Square points with error bars indicate measured rotation velocities as a function of distance from the galactic center. The different lines represent the contributions from the bulge (dotted), the disk(filled circles), the HI layer (crosses), the H_2 layer (circles) and from the dark halo (dashed). The solid line represents the sum of the contributions.

1.2 Dark matter candidate

The cosmological and galactic observations indicated that non-baryonic dark matters exist with a density parameter of $\Omega_{\mathrm{DM}} \sim 0.2-0.3$ since Ω_{b} (~ 0.022) is much less than Ω_{m} (0.132). Two types of non-baryonic dark matter candiates are considered. One is the Hot Dark Matter(HDM), which travels with relativistic velocity. Another one is the Cold Dark Matter (CDM), which travels with non-relativistic velocity. The best candidate for the identity of the HDM is the neutrino, however, galactic cluster observations and WMAP results restricted the neutrino density to $0.003 \leq \Omega_\nu \leq 0.10$[9]. On the other hand, physicists have suggested many candidates of the CDM based on various theories. In this section, we review two plausible CDM candiates; axion, and WIMP.

1.2.1 Axion

The axion was originally proposed as a neutral new light pseudo-scalar boson to solve the CP conservation problem of strong interactions [10]. The CP invariance of strong interactions is violated in the context of the quantum chromodynamics (QCD) theory, which was not observed by any experiments. Although the theories do not predict the axion mass, laboratory experiments and implications from astrophysical and cosmological effects have excluded the most of the mass range, leaving only two windows, 10^{-6} eV $\leq m_a \leq 10^{-3}$ eV and 2 eV $\leq m_a \leq 5$ eV, for further explorations. The axion with its mass in the lighter window could be a candidate of the CDM and one with its mass in the heavier windows could be produced in the Sun (the Solar axion).

The CDM axion, has been searched with the Sikivie radio frequency cavity technique. The most recent experiment searched the axion mass range of $2.3~\mu\mathrm{eV} \leq m_a \leq 3.4\mu\mathrm{eV}$ and obtained no positive signal of the CDM axion[11].

The Solar axion has been searched with superconducting magnet telescopes using the inverse Primakoff effect [12] ($a \underset{\leftarrow}{\overset{\rightarrow}{}} 2\gamma$). Recent results from the CERN Axion Solar Telescope [13] and Tokyo helioscope group[14] imply upper limits on the axion-photon coupling, $g_{a\gamma} < 1.16 \times 10^{-10}\mathrm{GeV}^{-1}$ at 95% C.L. for the axion mass of $m_a \leq 0.02$ eV, and $g_{a\gamma} < 5.6 - 13.4 \times 10^{-10}$ GeV^{-1} for the axion mass of $0.84 < m_a < 1.00$ eV, respectively (Figure 1.5).

1.2.2 WIMP

The widely discussed the non-baryonic dark matter candidatse are Weakly Interacting Massive Particles (WIMPs). "Weakly interacting" means that these particles interact only via gravity and any weaker force than electromagnetic force, "Massive" means sufficiently massive to solve the structure-formation problem brought on by a baryons-only, or even a neutrinos and baryons, the Universe. This would require a WIMP mass of at least 1 keV. Incidentally, the particle physics provides some good generic rationale for the existence of WIMPs. Supersymmetry (SUSY), a well-motivated and presently most-favored extension from the Standard Model of the particle physics, implies WIMPs. The details of the SUSY dark matter are described in Section 1.3. On the other hand, theories of the universal extra dimensions in which Kaluza-Klein parity is conserved provide a second possible class known as the lightest Kaluza-Klein particle (LKP)[16, 17, 18].

1.3 SUSY dark matter - LSP neutralino

The lightest new particle in the SUSY, neutralino, is the most plausible candidate of the dark matter because there are much more agreements between the expected property of the
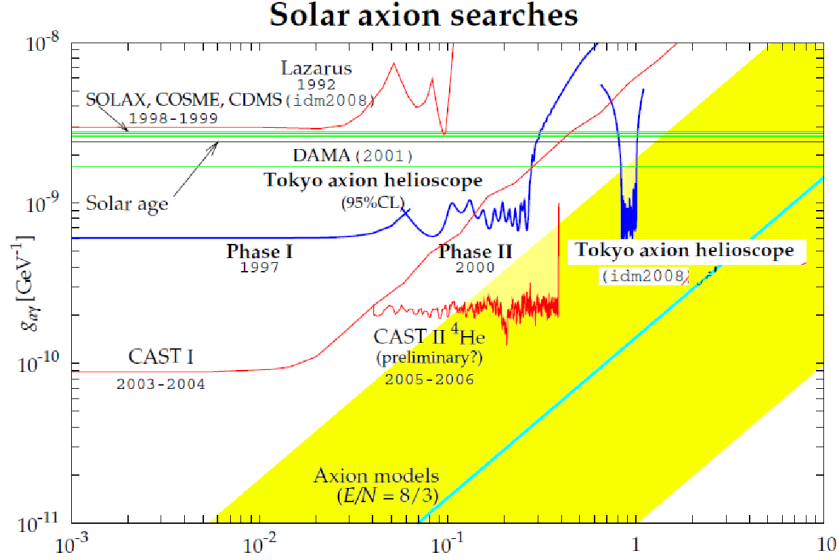
Figure 1.5: Solar axion search results. 95% C.L exclusion lines of each experiment to the axion-photon coupling constant as a function of the axion mass are shown. Region above the limit lines are excluded and yellow region is the theoretical allowed region for axion.

neutralino and the cosmological requirement than other candidates and the proper rationale of the existence of the neutralino.

1.3.1 SUSY

The standard model (SM), which is a non-Abelian gauge theory based on the gauge group $SU(3)_{color} \times SU(2)_{left} \times U(1)_{hypercharge}$ of strong, electromagnetic and weak interactions acting on the quark and lepton multiplet, is an extraordinarily successful theory, and describes all experimental results on the interactions between elementary particles with a surprising accuracy. However, the SM has its natural drawbacks and unresolved problems. Some of the problems are listed below.

- The SM has a large number of free parameters.

- There is the strong CP problem in the SM.

- The SM is not unified with gravity.

- The flavor mixing and the number of generations are arbitrary in the SM.

- The hierarchy problem occurs in the SM.

- The grand unification is not realized.

SUSY theory introduces hypothtical "symmetrical" particles and solve the "hierarchy problem". SUSY presupposes that each elementary particle with a spin j in the SM has a supersymmetric partner with a spin $|j - 1/2|$ as shown in Table 1.1

From precise measurements of the coupling constants and the solution of the renormalization group equations for the evolution of the coupling constants, the possibility of the

Normal particles			SUSYparticles		
Symbol	Name	Spin	Symbol	Name	Spin
$q = u, c, t$	up quarks	1/2	$\tilde{q}_u^1, \cdots, \tilde{q}_u^6$	up squarks	0
$q = d, s, b$	down quarks	1/2	$\tilde{q}_d^1, \cdots, \tilde{q}_d^6$	down squarks	0
$l = e, \mu, \tau$	leptons	1/2	$\tilde{l}_1, \cdots, \tilde{l}_6$	sleprtons	0
ν_e, ν_μ, ν_τ	neutrinos	1/2	$\tilde{\nu}_1, \tilde{\nu}_2, \tilde{\nu}_3$	sneutrinos	0
g	gluons	1	$\tilde{g}$	gluinos	1/2
$W^\pm$	W bosons	1	$\tilde{\chi}_1^\pm, \tilde{\chi}_2^\pm$	charginos	1/2
$H^\pm$	charged Higgs	0			
γ	photon	1			
Z^0	Z boson	1			
$h^0(H_2^0)$	light scaler Higgs	0	$\tilde{\chi}_1^0, \cdots, \tilde{\chi}_4^0$	neutralinos	1/2
$H^0(H_1^0)$	heavy scaler Higgs	0			
$A^0(H_2^0, P_0)$	pseudoscaler Higgs	0			

Table 1.1: SUSY particles

unification with the gravity within the SM was excluded. On the other hand, SUSY particles affect the slope of the couplings, and unification of the coupling constants is realized at 10^{16}GeV/c^2 in the case of SUSY breaking scale, $M_{\text{susy}} \sim 1$ TeV/c^2 as shown in Fig. 1.6. In general, M_{susy} must be in the range from 100 GeV/c^2 to about 10 TeV/c^2 to provide this unification.

1.3.2 Neutralino

In the minimum supersymmetric extension of the standard model (MSSM), where the standard model is extended with only an extra Higgs doublet and partners required to form supersymmetric multiplets, the interactions of SUSY particles with ordinary particles are governed by "R-parity". The R-parity is given by

$$R = (-1)^{3B+L+2S}, \tag{1.9}$$

where B is the baryon number, L is the lepton number and S is the spin. The supersymmetric particles are assigned odd R-parities and the ordinary particles are assigned even R-parities. Conservation of the R-parity has following two consequences.

- The supersymmetric particles are created in pairs.

- The lightest supersymmetric particle (LSP) is stable.

The lightest neutralino ($\chi \equiv \tilde{\chi}_1^0$), the lowest-mass linear combination of the photino ($\tilde{\gamma}$), the zino ($\tilde{Z}$) and the higgsinos ($\tilde{H}_1, \tilde{H}_2$), is the leading candidate for the LSP and also for the non-baryonic cold dark matter. The photino and zino are expressed with the superpartners of gauge bosons (Gauginos), Bino ($\tilde{B}$) and Wino ($\tilde{W}$) as

$$\tilde{\gamma} = \cos\theta_W \tilde{B} + \sin\theta_W \tilde{W}_3 \quad \tilde{Z} = -\sin\theta_W \tilde{B} + \cos\theta_W \tilde{W}_3. \tag{1.10}$$

13
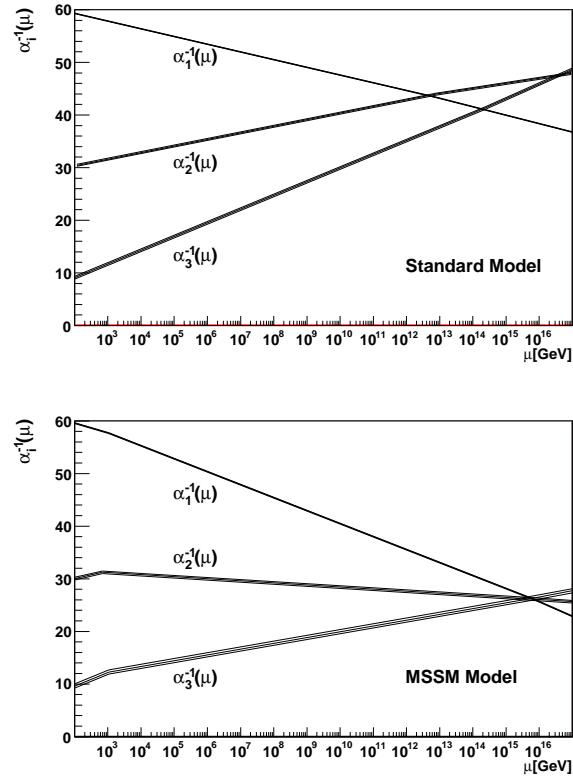
Figure 1.6: Running of couplings in the Standard Model(SM) (top) and in the Minimal Supersymmetric Standard Model (MSSM) (bottom). α_1, α_2 and α_3 are the $U(1)$ hypercharge, $SU(2)$ electroweak and $SU(3)$ strong couplings, respectibely. Only in the bottom case the unification of the coupling constants is realized. [19]

Thus, χ can be written as

$$\chi = a_1 \tilde{B} + a_2 \tilde{W}_3 + a_3 \tilde{H}_1 + a_4 \tilde{H}_2. \tag{1.11}$$

The neutralino mass matrix is written as

$$\begin{pmatrix} M_1 & 0 & -M_Z \cos\beta \sin\theta_W & M_Z \cos\beta \cos\theta_W \\ 0 & M_2 & M_Z \sin\beta \sin\theta_W & -M_Z \sin\beta \cos\theta_W \\ -M_Z \cos\beta \sin\theta_W & M_Z \sin\beta \sin\theta_W & 0 & -\mu \\ M_Z \cos\beta \cos\theta_W & -M_Z \sin\beta \cos\theta_W & -\mu & 0 \end{pmatrix} \tag{1.12}$$

where M_1 and M_2 are the respective mass parameters of U(1) and SU(2) gaugino, μ is the higgsino mass parameter, $\sin^2 \theta_W$ is the weak mixing angle, M_Z is the Z bozon mass and $\tan\beta \equiv v_2/v_1$, where v_1 and v_2 are the vacuum expectation values of the two Higgses. If we assume the grand unification, $M_1 = (5/3)M_2 \tan^2 \theta_W \sim 0.5 M_2$ is obtained, thus the neutralino mass matrix is characterized by three parameters: μ, M_2 and $\tan\beta$. In general, three basic configurations exist:

- Gaugino dominated: If M_1, $M_2 \ll \mu$, then the lightest neutralino is primarily the gaugino.

- Higgsino dominated : If $\mu \ll M_1, M_2$, then the lightest neutralino is primarily the higgsino.

- Mixed: If $M_1 \sim \mu$, then the neutralino is a roughly equal mixture of the gaugino and the higgsino.

It should be noted that the bino, wino and higgsino have different interactions, so the composition affects both the annihilation cross section and thus the relic density as well as the cross section for the neutralino-quark scattering.

1.4 Review of neutralino search experiment

There have been three types of neutralino search experiments: direct search experiments, indirect searches, and searches by accelerator experiments. We will review these experiments in this section.

1.4.1 Direct search

If the neutralino, WIMPs, exist as the dark matter, the earth encounters the dark matter halo with the relative speed of our solar system against that of the Galaxy. The WIMPs from the halo can elastically scatter off the target nucleus of a detector in the laboratory. Thus, the WIMPs can directory be detector as nuclear recoil signals. These signals are expcted to provide information on the dark matter mass and the neutralino-quark cross sections with some astrophysical assumptions (See Chapter 2).

The WIMP recoil event is very rare and the expected energy spectrum has a non-characteristic spectrum of a simple exponential spectrum, while the ambient γ-rays and neutrons make background events with energy similar to that from WIMPs. Thus the main challenge of the direct detection of dark matter experiments is the reduction and the discrimination of background events. Recently, the direct detection of dark-matter experiments are among the most exciting experimental physics around the world. These experiments require

	annihilation channels
$\chi\chi \rightarrow$	$f\bar{f}$
	$W + W^-$
	$Z^0 Z^0$
	$W^+ H^-, W^- H^+$
	$Z^0 A^0$
	$Z^0 H^0, Z^0 h^0$
	$A^0 A^0, H^0 H^0, h^0 h^0, H^0 h^0$
	$A^0 H^0, A^0 h^0$
	H^+, H^-
	$gg, q\bar{q}g$
	$Z^0 \gamma, \gamma\gamma$

Table 1.2: The annihilation channel of the neutralino [15]. f and $\bar{f}$ are the standard model neutrinos, leptons and quarks, and A^0 are axions.

a very low background environment, thus they are usually located in deep underground laboratories. This thesis represents one of this type of experiments.

We will discuss the expected the WIMP event rate in Chapter 2 and the variety of detectors that currently search for the WIMP dark matter in Chapter 3.

1.4.2 Indirect search

The dark matter, neutralinos, is expected to be trapped in the core of the Galactic, the center of the Earth, and the Sun or may locally concentrate by some other reasons. In such a neutralino concentration area, the annihilation of the neutralino may often occur and produce γ-rays and also other particles since the neutralino is a majonara fermion. The annihilation process has many channels as listed in Table 1.2 [15]. The detection of the annihilation products, such as γ- rays, positrons, anti-protons and neutralinos, etc., from specific directions and locations will provide indirect information on the dark matter.

Gamma ray γ-rays may result from annihilation $\chi\chi \rightarrow \gamma\gamma$ or $\chi\chi \rightarrow Z\gamma$ [15]. The rates of these processes are difficult to be estimated because of the uncertainties in SUSY parameters and halo density profiles. However, the γ-ray intensity from the neutralino annihilation in the galactic halo has a characteristic direction dependence.

The Energetic Gamma Ray Experiment Telescope (EGRET) on the Compton Gamma Ray Observatory has observed an about 60% higher integrated intensity for γ-rays from the galactic plane above 1 GeV than a model calculation of the emission based on the dynamic balance and the realistic interstellar matter and the photon distributions [28]. On the other hand, Elsaesser and Mannheim compared the extragalactic γ-ray background from EGRET data with high-resolution simulations of the cosmic structure formation, and found a best fit value of neutralino mass around 515^{+110}_{-75} GeV [29]. But it appeared that the result of [29] had a systematic uncertainty in the high energy region. The next generation γ-ray observatory GLAST (Gamma-Ray Large Area Space Telescope) was launched in June, 2008 and renamed as "Fermi". Fermi satelite is expected to reach a sensitivity of 2×10^{-9} photons cm^{-2}s^{-1}, which is 30 times better than EGRET, for γ-rays in enegy range of 100 MeV to 300 GeV after two year's observation [30] .

Antimatter   Self annihilation of WIMPs will also produce particles such as positron (e^+), antiprotons $(\bar{p})$, antideuterons $(\bar{D})$ and other heavy anti-nuclei. The measured antiproton or antideuteron spectrum can provide information on the light neutralino and can be used to put stringent constrains on the supersymmetric configuration [20, 21].

The searches for antiprotons or antideuterons have been performed by the Balloon-borne Experiment with Superconducting Spectrometer (BESS). Fir the antiprotons searche, they found the effect of the solar modulation to the antiproton spectrum was large and have never achieved the dark matter contribution[22]. For the cosmic antideuteron search, no candidates of antideuteron was found from data during four balloon flights from 1997 to 2000. An upper limit of $1.9 \times 10^{-4} (\mathrm{m}^2 \mathrm{s}$ sr GeV/nucleon$)^{-1}$ at the 95% confidence level was derived for the differential flux of cosmic-ray antideutrons at the top of the atmosphere with energy range of 0.17 and 1.15 GeV/nucleus [23].

The satellite projects of PAMELA[24] has be performing in the outer space orbits from 2006. The PAMELA detector has a superconducting spectrometer and calorimeters. The PAMELA collaboration reported a result of the measurement of the positron abundance in the cosmic ray up to 100 GeV[25], that the positron fraction increased in the energy range above 10 GeV (Figure. 1.7). According to [26], the annihilation of neutralino may affects the amount of the cosmic positron in the energy region above 10 GeV.

The next generation antimatter detector GAPS (the General Antiparticle Spectrometer) identifies antimatter through the characteristic X-rays emitted by antimatter when it is captured in the target and forms an exotic atoms. Its sufficient sensitivity to detect antideuterons will probe the SUSY parameter space for a sensitive indirect dark matter search [27].
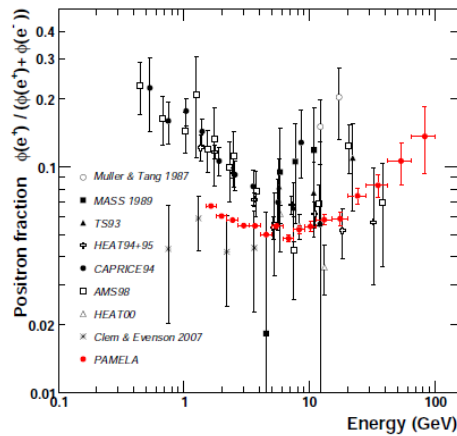
Figure 1.7: Positron fraction measured by PAMELA (red points and error bars)[25]. Black marks show results of other experiment measurements.

Muon neutrino   Neutralinos scatter elastically off nuclei in the Earth, the Sun and the Galactic Center. If neutralinos velocities become less than the escape velocity in the process, they are gravitationally trapped in the core of them. The accumulated neutralinos can self-annihilate and produce various particles. Among the products, energetic muon neutrinos can escape from the core and should be detected by the neutrino detectors on the Earth. The energetic neutrinos will undergo charged current interactions in the rock below the detector or within the detector. Therefore, neutralinos are indirectly detectable as upward-going muons. Since the energies of these muons will be typically 1/3 to 1/2 of the neutrino mass, they cannot be confused with ordinary neutrinos [31].

Fluxes predicted for such muon neutrino events in SUSY models seem to fall for the most part between 10^{-6} and 10^{-2} events/m^2/yr. Several experiments are ongoing and have set limits on the flux of upward-going muons from the Earth. The tightest limits have been reported by the Super-Kamiokande Collaboration [31]. The new generation neutralino telescopes such as IceCube [32] and ANTARES [33] are under development.

1.4.3   Search by accelerator experiment

The neutralino searches have been also performed by accelerator experiments (LEP2 performed at CERN [34], for instance). Neutralinos could be produced in an e^+e^- collider through an s-channel virtual Z, or by a t-channel scalar electron (selectron, $\tilde{e}$) exchange as bellow.

$$e^+e^- \to \tilde{\chi}_1^0\tilde{\chi}_2^0 \text{ or } \tilde{\chi}_2^0\tilde{\chi}_2^0 \tag{1.13}$$

. Produced the$\tilde{\chi}_2^0$ will decay into

$$\tilde{\chi}_2^0 \to \tilde{\chi}_1^0 Z^* \to \tilde{\chi}_1^0 f\tilde{f} \quad \text{or} \quad \tilde{\chi}_2^0 \to \tilde{\chi}_1^0 \gamma. \tag{1.14}$$

The signature is a missing energy due to the undetected $\tilde{\chi}_0^1$ and one or two photons, two or four leptons, or one to four hadronic jets. Constrained Minimal Supersymmetric Standard Model (CMSSM) motivated by Grand Unified Theory (GUT) is often used for the analysis to simplify physics interpretations. The lower limit to $M_{\tilde{\chi}_1^0}$ mass for a certain parameter set is 40 GeV c^{-2} [34]. However, searches for neutralino with lighter masses are still needed because it is probable the GUTs may not work and neutralinos with a mass of a few GeV c^{-2} can exist [35].

Neutralino could also be produced in a pp collider through various channels. Tevatron collider searched for the neutralino at the maximum collision energy of 2 TeV. They reported the limit of neutalino life time [36]. The Large Hadron Collider (LHC), which has started in September 2008 and will be operated at the maximum collision energy of 14 TeV, is expected to produce many SUSY particles. Detectable neutralino events are expected from the production of the heavier SUSY particles, which in turn decay via a multi-step cascade to the stable LSP. The LSP could be identifid by a missing mass of those interaction. The LHC experiment will find a neutralino or give a much more stringent constrain to the neutralino parameters [37].

Chapter 2

Direct detection of neutralino

Neutralinos can be detected via elastic scatterings with ordinary matters. SUSY theory predicts two types of the interactions, namely spin-independent(SI) and spin-dependent(SD) interactions. Feynman diagrams of the spin-independent and the spin-dependent neutralino-quark elastic scatterings are shown in Figure 2.1 and Figure 2.2, respectively. Many experiments have been performed to reveal the existence of the WIMPs assuming these interactions. In this chapter, the theoretical framework of the direct detection of neutralino is described based on ref. [38].

2.1 Dynamics of the Earth, the Sun and the neutralino

The motions of galaxies indicate that the dark matters exist as dark halo in the galalxies. Thus the dark matter direct detection rate strongly depends on a realtive motion between the detector on the Earth and the dark matter. In this section we discribe relative motions of the Earth, the Sun and the neutralino dark matter with respect to our Galaxy. The detector velocity on the Earth in the Galactic rest frame can be expressed as;

$$\mathbf{v}_{\mathrm{E}} = \mathbf{v}_{\mathrm{c}} + \mathbf{v}_{\mathrm{LSR}} + \mathbf{v}_{\mathrm{ES}}, \tag{2.1}$$

where $\mathbf{v}_{\mathrm{c}}$ is the rotational velocity around the Galactic Center, $\mathbf{v}_{\mathrm{LSR}}$ is the solar system's velocity with respect to the Local Standard of Rest, and $\mathbf{v}_{\mathrm{ES}}$ is the earth's velocity with respect to the Sun. The velocity of the Sun ($\mathbf{v}_{\mathrm{SUN}} = \mathbf{v}_{\mathrm{c}} + \mathbf{v}_{\mathrm{LSR}}$) can be found from the equatorial coordibatres of the Galactic Center (Sagitarius A*, 17h45m37.199s
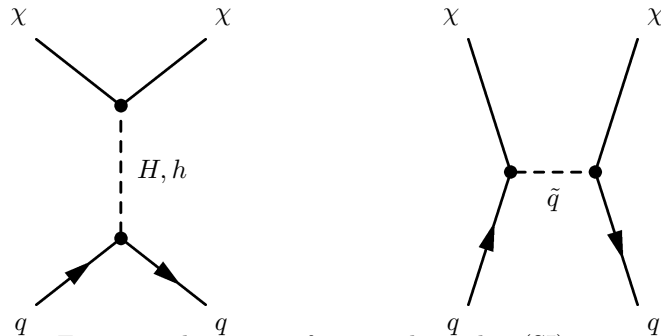
Figure 2.1: Feynman diagrams of spin-independent(SI) interactions between a neutralino and a quark.

19
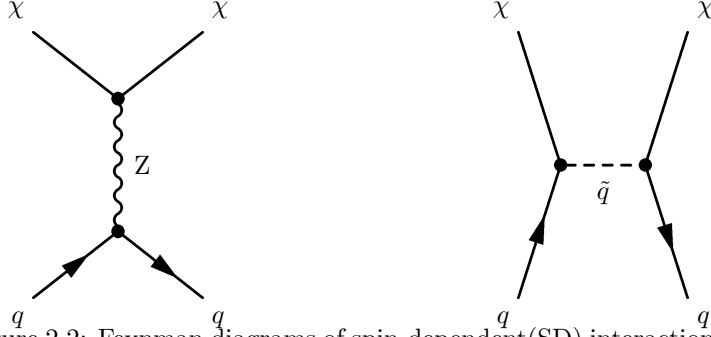
Figure 2.2: Feynman diagrams of spin-dependent(SD) interactions between a neutralino and a quark.

R.A., $-28°56'10.23"$ decl.(J2000.0)) and of the Galactic North Pole (12h51m26.275s R.A., $+27°07'41.7"$ decl. (J2000.0)). They identify a point in the celestial sphere with equatorial coordinates of 21h12m01,053s R.A., $+48°19'46.71"$ decl(J2000.0), which is the direction of the constellation Cygnus. Since the component of $\mathbf{v}_{\mathrm{LSR}}$ parallel to the galactic rotation is 12 km/s, the absolute value of $\mathbf{v}_{\mathrm{SUN}}$ is considered to be $\sim$230 km/s. On the other hand, the component of $\mathbf{v}_{\mathrm{ES}}$ paralleled to the galactic rotaion, $v_{\mathrm{ES}\parallel}$ is generally expressed as

$$v_{\mathrm{ES}\parallel} = v_{\mathrm{orb}} \cos \zeta \cos(\omega t). \tag{2.2}$$

Here $v_{\mathrm{orb}} \sim 30$ km/s denotes the Earth orbital speed velocity with respect to the Sun. The angle $\zeta \simeq 60°$ is the inclination of the Earth orbital plane with respect to the Galactic plane and $\omega = 2\pi/\mathrm{year}$. t is the elasped time from June 2nd in years when $v_{\mathrm{ES}\parallel}$ has the maximum.

2.2 Event rate

The differential event rate per unit target mass (kg) is

$$dR = \frac{N_{\mathrm{A}}}{A} \sigma_{\chi-\mathrm{N}} v dn, \tag{2.3}$$

where N_{A} is the Avogadro number per unit mass ($6.02 \times 10^{26} \mathrm{kg}^{-1}$), A is the mass number of a target nucleus, $v = |\mathbf{v} - \mathbf{v}_{\mathrm{E}}|$, which is the dark matter velocity relative to the target n is the dark matter particle number density, and $\sigma_{\chi-\mathrm{N}}$ is the neutralino-nucleus ($\chi - \mathrm{N}$) cross section for zero momentum transfer. The cross section for non-zero momentum transfer, $\sigma_{\chi-\mathrm{N(non-zero)}}$ is expressed as

$$\sigma_{\chi-\mathrm{N(nonzero)}} = \sigma_{\chi-\mathrm{N}} F^2(E_{\mathrm{R}}), \tag{2.4}$$

which is discussed later in this Section. The total event rate, R, is then expected as

$$R = \frac{N_0}{A} \sigma_{\chi-\mathrm{N}} \int v dn = \frac{N_0}{A} \sigma_{\chi-\mathrm{N}} n_0 \langle v \rangle, \tag{2.5}$$

where $n_0 = \frac{\rho_{\mathrm{D}}}{M_{\chi}}$ is the mean dark matter particle density given by the ratio of the dark matter density, ρ_{D}, to the neutralino mass, M_{χ}, and $\langle v \rangle$ is the mean dark matter velocity.

A Maxwell-Boltzmann distribution,

$$f(\mathbf{v}, \mathbf{v}_E) = \frac{1}{(\pi v_0^2)^{\frac{3}{2}}} e^{-|\mathbf{v}+\mathbf{v}_E|^2/v_0^2}, \tag{2.6}$$

is practically assumed as the dark matter velocity distribution. Here v_0 is the velocity dispersion of the dark matter. For $\mathbf{v}_E = 0$ and the local Galactic escape velocity $v_{esc} = \infty$, $\langle v \rangle$ is expressed as

$$\langle v \rangle = \frac{2}{\sqrt{\pi}} v_0. \tag{2.7}$$

From Eq. (2.5) and Eq. (2.7), the total event rate for $v_E = 0$ and $v_{esc} = \infty$, R_0 is expressed as

$$R_0 = \frac{N_0}{A} \sigma_{\chi-N} \frac{\rho_D}{M_\chi} \frac{2}{\sqrt{\pi}} v_0. \tag{2.8}$$

R_0 is conventionally expressed in units of $\text{kg}^{-1} \text{ day}^{-1}$. Normalized to $\rho_D = 0.3 \text{GeVc}^{-2}\text{cm}^{-3}$ and $v_0 = 220 \text{ km s}^{-1}$, Eq. 2.8 becomes

$$R_0 = \frac{361}{M_\chi M_N} \left(\frac{\sigma_{\chi-N}}{1\text{pb}}\right) \left(\frac{\rho_D}{0.3 \text{ GeVc}^{-2}\text{cm}^{-3}}\right) \left(\frac{v_0}{220 \text{ km s}^{-1}}\right) \tag{2.9}$$

with M_χ, M_N in units of GeV c^{-2}. M_N is the mass of the target nucleus ($M_N = 0.932$ A).

The total event rate for $v_E \neq 0$ and $v_{esc} \neq \infty$ is expressed using Eq. (2.5) and Eq. (2.8) as

$$R = R_0 \frac{\pi}{2} \frac{\langle v \rangle}{v_0} = R_0 \frac{k_0}{k} \frac{1}{2\pi v_0^4} \int v f(\mathbf{v}, \mathbf{v}_E) d^3 v, \tag{2.10}$$

where k is the normalization constant

$$k = \int_0^{2\pi} d\phi \int_{-1}^1 d(\cos\theta) \int_0^{v_{esc}} f(\mathbf{v}, \mathbf{v}_E) v^2 dv. \tag{2.11}$$

$k_0 = (\pi v_0^2)^{\frac{3}{2}}$ is the value of k for $v_{esc} = \infty$. Eq. (2.10) is then,

$$\frac{R(0, v_{esc})}{R_0} = \frac{k_0}{k_1} \left[1 - \left(1 + \frac{v_{esc}^2}{v_0^2}\right) e^{-v_{esc}^2/v_0^2}\right], \tag{2.12}$$

$$\frac{R(v_E, v_\infty)}{R_0} = \frac{1}{2} \left[\pi^{\frac{1}{2}} \left(\frac{v_E}{v_0} + \frac{1}{2}\frac{v_0}{v_E}\right) Erf(\frac{v_E}{v_0}) + e^{-v_E^2/v_0^2}\right], \tag{2.13}$$

$$\frac{R(v_E, v_{esc})}{R_0} = \frac{k_0}{k_1} \left[\frac{R(v_E, \infty)}{R_0} - \left(\frac{v_{esc}^2}{v_0^2} + \frac{1}{3}\frac{v_E^2}{v_0^2} + 1\right) e^{-v_{esc}^2/v_0^2}\right], \tag{2.14}$$

where $Erf(x) = 2/\sqrt{\pi} \int_0^x \exp(-t^2)dt$. k_1 is the value of k for $v_{esc} \neq \infty$ written as

$$k_1 = k_0 \left[Erf\left(\frac{v_{esc}}{v_0}\right) - \frac{2}{\sqrt{\pi}} \frac{v_{esc}}{v_0} e^{-v_{esc}^2/v_0^2}\right]. \tag{2.15}$$

The recoil energy of the nucleus with a mass M_N caused by an elastic scattering of the

dark matter particle of the mass M_χ with the kinematic energy E is

$$E_R = Er(1 - \cos\theta)/2, \tag{2.16}$$

where θ is the scattering angle (in the center of mass) and

$$r = \frac{4 M_\chi M_N}{(M_\chi + M_N)^2} . \tag{2.17}$$

With an assumption that the scattering is isotropic, and where E_R is uniformly distributed over the range of $0 \le E_R \le Er$, then the differential event rate is

$$\frac{dR}{dE_R} = \int_{E_{min}}^{E_{max}} \frac{1}{E_R} dR(E) = \frac{1}{E_0 r} \int_{v_{min}}^{v_{max}} \frac{v_0^2}{v^2} dR(v), \tag{2.18}$$

where $E_0 = 1/2 M_\chi v_0^2 = \left(\frac{v_0^2}{v^2}\right) E$, $E_{min} = E_R/r$ is the lowest energy of the incident particle which can produce a nuclear recoil of the energy E_R and $v_{min} = (2E_{min}/M_\chi)^{\frac{1}{2}}$ is the dark matter particle velocity corresponding to E_{min}. From Eq. (2.10),

$$dR = \frac{R_0}{E_0 r} \frac{k_0}{k} \frac{1}{2\pi v_0^2} \int_{v_{min}}^{v_{max}} \frac{1}{v} f(\mathbf{v}, \mathbf{v_E}) d^3 v, \tag{2.19}$$

then the differential spectral function is expressed using Eq. (2.18)

$$\frac{dR}{dE_R} = \frac{R_0}{E_0 r} \frac{k_0}{k} \frac{1}{2\pi v_0^2} \int_{v_{min}}^{v_{max}} \frac{1}{v} f(\mathbf{v}, \mathbf{v_E}) d^3 v. \tag{2.20}$$

For the simplest case of $v_E = 0$ and $v_{esc} = \infty$, Eq. (2.20) gives

$$\frac{dR(0, \infty)}{dR_R} = \frac{R_0}{E_0 r} e^{-E_R/E_0 r}. \tag{2.21}$$

Eq. (2.21) shows that the distribution of the recoil energy is determined by the mass of the dark matter particle and target nuclei. For non-zero v_E and finite v_{esc}, Eq. (2.20) gives

$$\begin{aligned}
\frac{dR(0, v_{esc})}{dE_R} &= \frac{k_0}{k_1} \frac{R_0}{E_0 r} \left(e^{-E_R/E_0 r} - e^{-v_{esc}^2/v_0^2} \right) \\
&= \frac{k_0}{k_1} \frac{R_0}{E_0 r} \left[\frac{dR(0, \infty)}{dE_R} - \frac{R_0}{E_0 r} e^{v_{esc}^2/v_0^2} \right], \tag{2.22} \\
\frac{dR(v_E, \infty)}{dE_R} &= \frac{R_0}{E_0 r} \frac{\pi}{4} \frac{v_0}{v_E} \left[Erf\left(\frac{v_{min} + v_E}{v_0}\right) - Erf\left(\frac{v_{min} - v_E}{v_0}\right) \right] \\
&\sim c_1 \frac{R_0}{E_0 r} e^{c_2 E_R/E_0 r}, \tag{2.23} \\
\frac{dR(v_E, v_{esc})}{dE_R} &= \frac{k_0}{k_1} \left[\frac{dR(v_E, \infty)}{dE_R} - \frac{R_0}{E_0 r} e^{-v_{esc}^2/v_0^2} \right], \tag{2.24}
\end{aligned}$$

where $c_1 = 0.751$ and $c_2 = 0.561$ are parameters in Eq. (2.23) for $v_E = 244.0$ km$\cdot$s^{-1}.

The Earth velocity v_E varies during the year as the Earth moves around the Sun.

$$v_E \sim 244 + 15\sin(2\pi y) \text{km} \cdot \text{s}^{-1}, \tag{2.25}$$

where y is the elapsed time from March 2nd in year. The Maxwellian velocity parameter, v_0, and the escape velocity, v_{esc}, are discussed by several authors [39, 40], and

$$v_0 = (220 \pm 40)\text{km} \cdot \text{s}^{-1}, \qquad (2.26)$$

$$v_{esc} = (450 - 650)\text{km} \cdot \text{s}^{-1}, \qquad (2.27)$$

are commonly used values.

2.3   Cross section

Neutralinos interact with quarks spin-independently(SI) and spin-dependently (SD). The cross section of each interaction can be calculated by assuming certain sets of parameters in the MSSM model [15, 41]

Theoretical Framework

The theoretical framework we use in the context of the MSSM is reviewed in this section. The MSSM Lagrangian leads to the following low-energy effective Lagrangian, $\mathcal{L}_{eff}$, which is suitable for describing elastic neutralino-quark interactions[41].

$$\mathcal{L}_{eff} = \quad \bar{\chi}\gamma^\mu\gamma^5\chi\bar{q}_i\gamma_\mu(\alpha_{1i} + \alpha_{2i}\gamma^5)q_i + \alpha_{3i}\bar{\chi}\chi\bar{q}_iq_i$$
$$+\alpha_{4i}\bar{\chi}\gamma^5\chi\bar{q}_i\gamma^5q_i + \alpha_{5i}\bar{\chi}\chi\bar{q}_i\gamma^5q_i + \alpha_{6i}\bar{\chi}\gamma^5\chi\bar{q}_iq_i \quad , \qquad (2.28)$$

where q_i denotes the quark and the subscript i labels up-type quarks $(i = 1)$ and down type quarks $(i = 2)$. This Lagrangian is to be summed over the quark generations. Terms in Eq. (2.28) with coefficients α_{1i}, α_{4i}, α_{5i} and α_{6i} make contributions to the elastic scattering cross section that have a velocity dependence, and may be neglected for dark matters with non-relativistic velocities. Coefficients α_{2i} and α_{3i} contribute to the SD and SI interactions, respectively. α_{2i} and α_{3i} are written as follows.

$$\alpha_{2i} = \frac{1}{4(M_{1i}^2 - M_\chi^2)}\left[|Y_i^2| + |X_i^2|\right] + \frac{1}{4(M_{2i}^2 - M_\chi^2)}\left[|V_i^2| + |W_i^2|\right]$$
$$-\frac{g^2}{4M_Z^2\cos^2\theta_W}\left[|a_3|^2 - |a_4|^2\right]\frac{T_i^3}{2}, \qquad (2.29)$$

$$\alpha_{3i} = \frac{1}{2(M_{1i}^2 - M_\chi^2)}Re\left[(X_i)(Y_i)^*\right] - \frac{1}{2(M_{2i}^2 - M_\chi^2)}Re\left[(W_i)(V_i)^*\right]$$
$$-\frac{gM_{qi}}{4M_WB_i}\left[Re(\delta_{1i}[ga_2 - g'a_1])D_iC_i\left(-\frac{1}{M_{H_1}^2} + \frac{1}{M_{H_2}^2}\right)\right.$$
$$\left.+Re(\delta_{2i}[ga_2 - g'a_1])\left(\frac{D_i^2}{M_{H_2}^2} + \frac{C_i^2}{M_{H_1}^2}\right)\right], \qquad (2.30)$$

where M_{qi}, is the quark mass. Eq. (2.29) and (2.30) are to be summed over q and i. M_{1i} and M_{2i} are the squark mass eigenvalues, M_χ is the neutralino mass, M_Z is the Z bozon mass, M_W is the W boson mass, T_i^3, is the third component of the weak isospin, $a_{1,2,3,4}$ are the neutralino composition parameters in Eq. (1.11), $M_{H_2} < M_{H_1}$ denotes two scaler Higgs mass, and θ_W is the weak mixing angle, which is given by the ratio of the two weak coupling

constants, $\tan \theta_W = g'/g$.

$$X_i \equiv \eta_{11}^* \frac{g M_{q_i} a_{5-i}^*}{2 M_W B_i} - \eta_{12}^* e_i g' a_1,$$

$$Y_i \equiv \eta_{11}^* \left(\frac{y_i}{2} g' a_i + g T_i^3 a_2 \right) + \eta_{12}^* \frac{g M_{q_i} a_{5-i}^*}{2 M_W B_i},$$

$$W_i \equiv \eta_{21}^* \frac{g M_{q_i} a_{5-i}^*}{2 M_W B i} - \eta_{22}^* e_i g' a_1,$$

$$V_i \equiv \eta_{22}^* \frac{g M_{q_i} a_{5-i}^*}{2 M_W B_i} + \eta_{21}^* \left(\frac{y_i}{2} g' a_i + g T_i^3 a_2 \right). \tag{2.31}$$

Here y_i denotes the hyper charge of the sfermion defined by $e_i = T_i^3 + y_i/2$, η is the sfermion mass matrix and defined for each flavor q_i, by an angle θ_{q_i} as

$$\begin{pmatrix} \eta_{11} & \eta_{12} \\ \eta_{21} & \eta_{22} \end{pmatrix} = \begin{pmatrix} \cos \theta_{q_i} & \sin \theta_{q_i} \\ -\sin \theta_{q_i} & \cos \theta_{q_i} \end{pmatrix}. \tag{2.32}$$

Other parameters in Eq. (2.29) and (2.30) are

$$\delta_{11} = a_3, \ \delta_{12} = a_4, \ \delta_{21} = a_4, \ \delta_{22} = -a_3, \tag{2.33}$$

$$A_1 = \cos \beta, \ A_2 = -\sin \beta, \ B_1 = \sin \beta, \ B_2 = \cos \beta, \tag{2.34}$$

$$C_1 = \sin \beta, \ C_2 = \cos \alpha, \ D_1 = \cos \alpha, \ D_2 = -\sin \alpha. \tag{2.35}$$

$$\tag{2.36}$$

Here α denotes the Higgs mixing angle, and $\tan \beta = v_2/v_1$, where v_1 and v_2 are the vacuum expectation values of the two Higgses. α, β and Higgs mass, M_H are related by the following equations.

$$\sin \alpha = - \left(\frac{1-k}{2} \right)^{\frac{1}{2}}, \ \cos \alpha = - \left(\frac{1+k}{2} \right)^{\frac{1}{2}}. \tag{2.37}$$

Here

$$k = c \left(\frac{c^2 + r^2 - 2r}{c_r^2 - 2rc} \right), \ c = \cos 2\beta, \ r = \frac{M_H^2}{M_Z^2}. \tag{2.38}$$

The cross section of the elastic neutralino-nucleon scattering is given by

$$\sigma_{\chi-N} \sim \sum_q |\langle N| \mathcal{L}_{\text{eff}} |N \rangle, \tag{2.39}$$

where $|n\rangle$ is a wave function of the nucleus.

Cross Section

The neutralino-nucleus cross section at zero momentum transfer is expressed as

$$\sigma_{\chi-N} = 4 G_F^2 \mu_{\chi-N}^2 C_N, \tag{2.40}$$

where $G_{\mathrm{F}} = 1.166 \times 10^{-5} \mathrm{GeV}^{-2} (\hbar c)^3$ is the Fermi coupling constant, $\mu_{\chi-\mathrm{N}}$ is the reduced mass of the neutralino ($M_\chi \mathrm{GeV\ c}^{-2}$) and the target nucleus ($M_\mathrm{N} \mathrm{GeV\ c}^{-2}$),

$$\mu_{\chi-\mathrm{N}} = \frac{M_\chi M_\mathrm{N}}{M_\chi + M_\mathrm{N}}. \tag{2.41}$$

C_N is a dimensionless number referred to as the enhancement factor that carries all the particle physics model information, C_N is expressed by the sum of SI and SD terms,

$$C_\mathrm{N} = (C_\mathrm{N}^{\mathrm{SI}} + C_\mathrm{N}^{\mathrm{SD}}). \tag{2.42}$$

In the following section, $C_\mathrm{N}^{\mathrm{SI}}$ and $C_\mathrm{N}^{\mathrm{SD}}$ values are discussed for various nuclei. Since $\sigma_{\chi-\mathrm{N}}$ can be expressed as

$$\sigma_{\chi-\mathrm{N}} = \sigma_{\chi-\mathrm{p}} \frac{\mu_{\chi-\mathrm{N}}^2}{\mu_{\chi-\mathrm{p}}^2} \frac{C_\mathrm{N}}{C_\mathrm{p}} = \sigma_{\chi-\mathrm{n}} \frac{\mu_{\chi-\mathrm{N}}^2}{\mu_{\chi-\mathrm{n}}^2} \frac{C_\mathrm{N}}{C_\mathrm{n}} \tag{2.43}$$

with the enhancement factor of proton C_p and neutron C_n. Here $\sigma_{\chi-\mathrm{p}}$ and $\sigma_{\chi-\mathrm{n}}$ are neutralino(χ)-proton and neutralino-neutron cross sections, respectively.

Spin-Independent (SI) interaction

The enhancement factor of the SI cross section is written as

$$C_\mathrm{N}^{\mathrm{SI}} = \frac{1}{\pi G_\mathrm{F}^2} \left[Z f^{(\mathrm{p})} + (A - Z) f^{(\mathrm{n})} \right]^2, \tag{2.44}$$

where A is the mass number and Z is the atomic number [41]. $f^{(\mathrm{p})}$ and $f^{(\mathrm{n})}$ are proton-neutralino and neutron-neutralino SI couplings, respectively, while they are written as the neutralino-quarks SI couplings, $f_{T_q}^{(\mathrm{p})}$ and $f_{T_q}^{(\mathrm{n})}$, summed over the quarks that comprise nucleon as described below.

$$\frac{f^{(\mathrm{p})}}{M_p} = \sum_{q=u,d,s} f_{T_p}^{(\mathrm{p})} \frac{\alpha_{3q}}{M_q} + \frac{2}{27} f^{(\mathrm{p})} \sum_{q=c,b,t} \frac{\alpha_{3q}}{M_q}, \tag{2.45}$$

$$\frac{f^{(\mathrm{n})}}{M_n} = \sum_{q=u,d,s} f_{T_p}^{(\mathrm{n})} \frac{\alpha_{3q}}{M_q} + \frac{2}{27} f^{(\mathrm{n})} \sum_{q=c,b,t} \frac{\alpha_{3q}}{M_q}, \tag{2.46}$$

$$\tag{2.47}$$

where M_q is the quark mass, M_p and M_n are the proton and neutron masses, respectively. Parameters $f_{T_q}^{(\mathrm{p})}$ and $f_{T_q}^{(\mathrm{n})}$ are determined by the information of quark mass ratio and chiral symmetry applied to baryons. The value of $f_{T_q}^{(\mathrm{p})}$ and $f_{T_q}^{(\mathrm{n})}$ are as follows,

$$f_{T_u}^{(\mathrm{p})} = 0.020 \pm 0.004, \ f_{T_d}^{(\mathrm{p})} = 0.026 \pm 0.005, \ f_{T_s}^{(\mathrm{p})} = 0.118 \pm 0.062$$

$$f_{T_u}^{(\mathrm{n})} = 0.014 \pm 0.003, f_{T_d}^{(\mathrm{n})} = 0.036 \pm 0.008, f_{T_s}^{(\mathrm{n})} = 0.118 \pm 0.062, \tag{2.48}$$

while

$$f_{TG}^{(\mathrm{p})} = 1 - \sum_{q=u,d,s} f_q^{(\mathrm{p})},$$

$$f_{TG}^{(\mathrm{n})} = 1 - \sum_{q=u,d,s} f_q^{(\mathrm{n})}. \tag{2.49}$$

$$\tag{2.50}$$

In most case, $f_{T_q}^{(\mathrm{p})} \simeq f_{T_q}^{(\mathrm{n})}$, therefore $C_\mathrm{N}^\mathrm{SI} \propto A^2$ from Eq. (2.44),

$$\frac{C_\mathrm{N}^\mathrm{SI}}{C_\mathrm{p}^\mathrm{SI}} = \frac{C_\mathrm{N}^\mathrm{SI}}{C_\mathrm{n}^\mathrm{SI}} = A^2 \tag{2.51}$$

is a practical estimation. Eq. (2.43) and Eq. (2.51) give

$$\sigma_{\chi-\mathrm{p}}^\mathrm{SI} = \sigma_{\chi-\mathrm{N}}^\mathrm{SI} \frac{\mu_{\chi-\mathrm{p}}^2}{\mu_{\chi-\mathrm{N}}^2} \frac{1}{A^2}. \tag{2.52}$$

Eq. (2.52) can be used for the conversion of the obtained $\sigma_{\chi-\mathrm{N}}^\mathrm{SI}$ into $\sigma_{\chi-\mathrm{p}}^\mathrm{SI}$. Eq. (2.52) indicates that materials with large A values are effective for SI-interacting neutralinos. Conversion values of $\sigma_{\chi-\mathrm{N}}^\mathrm{SI}/\sigma_{\chi-\mathrm{p}}^\mathrm{SI}$ of materials are shown in Figure 2.3.
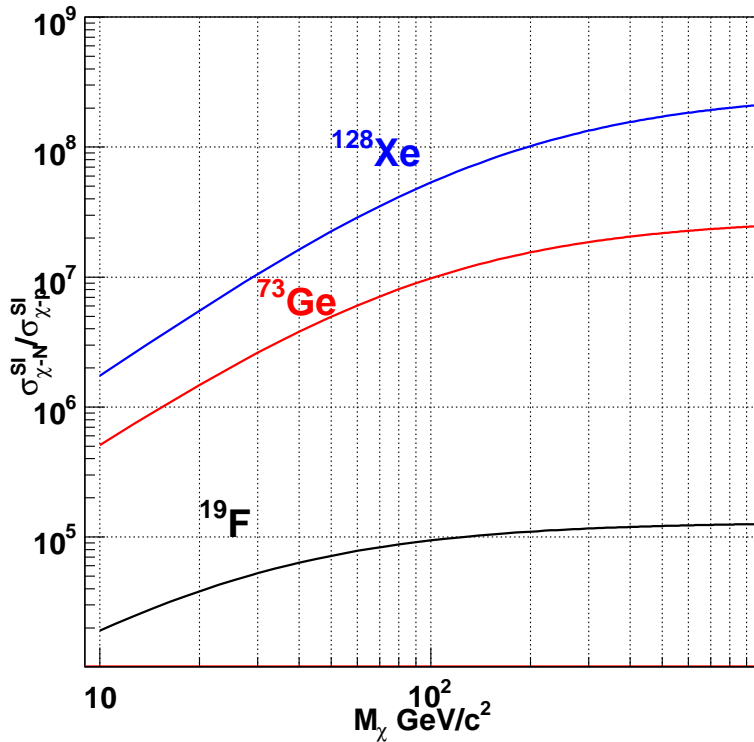
Figure 2.3: Function of conversion values from $\sigma_{\chi-\mathrm{p}}^\mathrm{SI}$ to $\sigma_{\chi-\mathrm{N}}^\mathrm{SI}$ for each nucleus as a function of neutralino mass.

Spin-Dependent(SD) interaction

The enhancement factor of the SD cross section is written as

$$C_N^{SD} = \frac{8}{\pi} \left(a_p \langle S_{p(N)} \rangle + a_n \langle S_{n(N)} \rangle \right)^2 \frac{J+1}{J}, \tag{2.53}$$

where $\langle S_{p(N)} \rangle$ and $\langle S_{n(N)} \rangle$ are the expectation values of the proton and neutron spin in the nucleus N [41]. a_p and a_n are the neutralino-nucleon SD couplings, and J is the total spin of the nucleus. a_p and a_n are expressed as

$$a_p = \sum_{q=u,d,s} \frac{\alpha_{2q}}{\sqrt{2}G_F} \Delta_q^{(p)}, \tag{2.54}$$

$$a_n = \sum_{q=u,d,s} \frac{\alpha_{2q}}{\sqrt{2}G_F} \Delta_q^{(n)}, \tag{2.55}$$

$$\tag{2.56}$$

where $\Delta_q^{(p)}$ and $\Delta_q^{(n)}$ are the quark spin contents of the nucleon, and are calculated as

$$\Delta_u^{(p)} = 0.78 \pm 0.02, \ \Delta_d^{(p)} = -0.48 \pm 0.02, \ \Delta_s^{(p)} = -0.15 \pm 0.02. \tag{2.57}$$

In the case of the neutron,

$$\Delta_u^{(n)} = \Delta_d^{(p)}, \ \Delta_d^{(n)} = \Delta_u^{(p)}, \ \Delta_s^{(n)} = \Delta_s^{(p)}, \tag{2.58}$$

Eq. (2.53) is written as

$$C_N^{SD} = \frac{8}{\pi} \lambda^2 J(J+1), \tag{2.59}$$

where

$$\lambda \equiv \frac{1}{J} \left(a_p \langle S_{p(N)} \rangle + a_n \langle S_{n(N)} \rangle \right). \tag{2.60}$$

λ is referred to as the Landé factor. $\lambda^2 J(J+1)$ values calculated on the basis of the odd group model for various nuclei are listed in Table 2.1. Eq. (2.43), Eq. (2.59) and Table 2.1 give

$$\sigma_{\chi-p}^{SD} = \sigma_{\chi-N}^{SD} \frac{\mu_{\chi-p}^2}{\mu_{\chi-N}^2} \frac{0.75}{\lambda^2 J(J+1)}. \tag{2.61}$$

Eq. (2.61) can be used for the conversion of the obtained $\sigma_{\chi-N}^{SD}$ into $\sigma_{\chi-p}^{SD}$. Values of $\frac{\sigma_{\chi-N}^{SD}}{\sigma_{\chi-p}^{SD}}$ and $\frac{\sigma_{\chi-N}^{SD}}{\sigma_{\chi-n}^{SD}}$ are shown in Figure 2.4 and Figure 2.5, respectivily.

As a "model independent" analysis, the case for the pure proton coupling ($a_n = 0$) and the pure neutron coupling ($a_p = 0$) are also checked to interpret the experimental results in terms of the SD interaction $\lambda^2 J(J+1)$ values calculated in the case of the pure proton coupling and the pure neutron coupling for various nuclei are listed in Table 2.2 and Table 2.3.
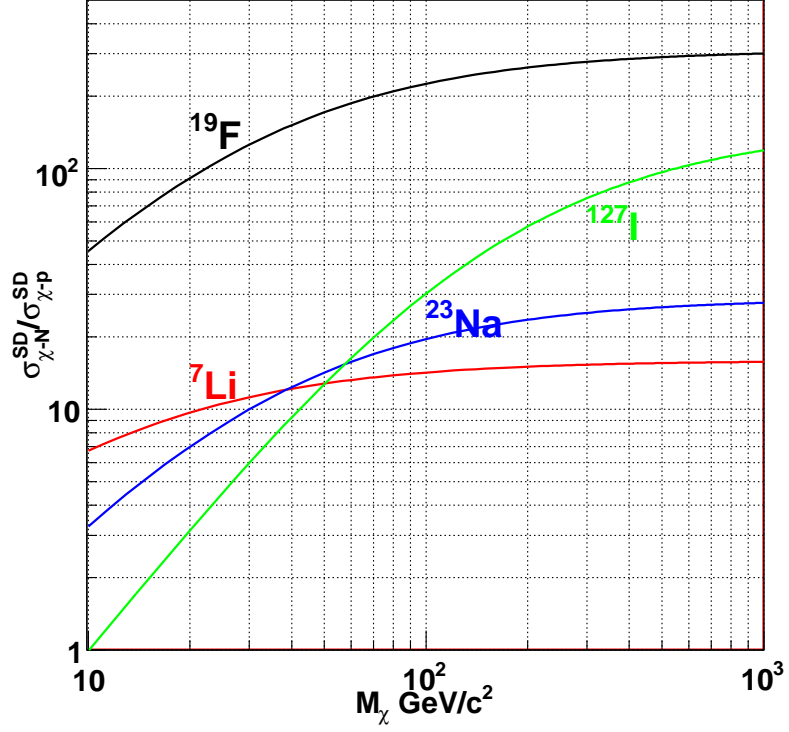
Figure 2.4: Function of conversion values from $\sigma^{\mathrm{SD}}_{\chi-\mathrm{P}}$ to $\sigma^{\mathrm{SD}}_{\chi-\mathrm{N}}$ as a function of the neutralino mass for each nucleus. Natural abundunce for each nucleus is considered.

unpaired proton			
Isotope	J	Abundance(%)	$\lambda^2 J(J+1))$
^{1}H	1/2	100	0.750
^{7}Li	3/2	92.5	0.244
^{19}F	1/2	100	0.647
^{23}Na	3/2	100	0.041
^{127}I	5/2	100	0.007
^{133}Cs	7/2	100	0.052
unpaired neutron			
Isotope	J	Abundance(%)	$\lambda^2 J(J+1))$
^{3}He	1/2	1.3×10^{-4}	0.928
^{29}Si	1/2	4.7	0.063
^{73}Ge	9/2	7.8	0.065
^{129}Xe	1/2	26.4	0.124
^{131}Xe	3/2	21.2	0.055
^{183}W	1/2	14.3	0.003

Table 2.1: Values of $\lambda^2 J(J+1)$ calculated in the basis of the odd group model for various nuclei.[38]
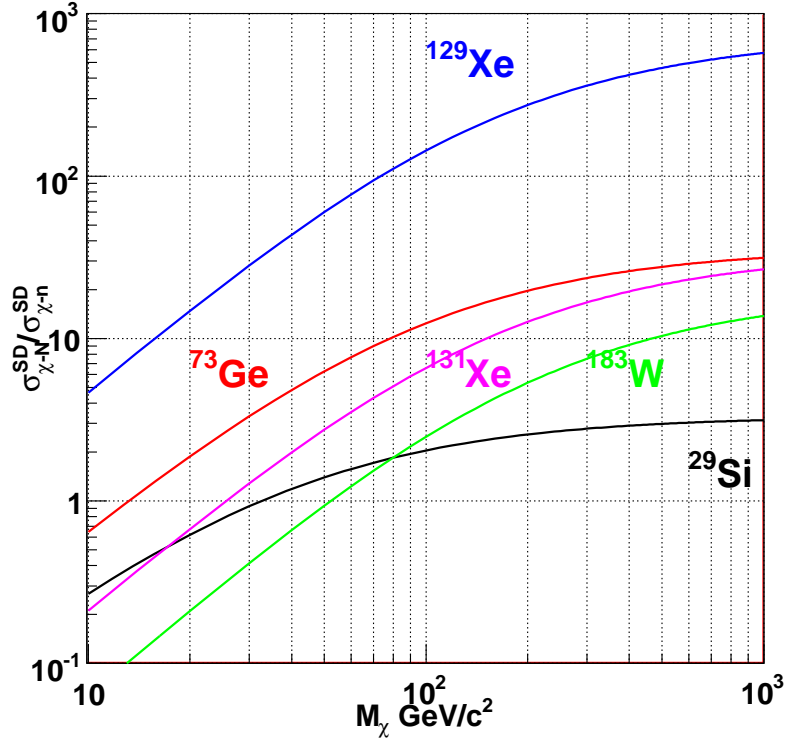
Figure 2.5: Function of conversion values from $\sigma_{\chi-n}^{SD}$ to $\sigma_{\chi-N}^{SD}$ as a function of the neutralino mass for each nucleus. Natural abundunce for each nucleus is considered.

unpaired proton			
Isotope	J	Abundance(%)	$\lambda^2 J(J+1))$
^{19}F	1/2	100	0.583
^{23}Na	3/2	100	0.103
^{127}I	5/2	100	0.133
unpaired neutron			
Isotope	J	Abundance(%)	$\lambda^2 J(J+1))$
^{29}Si	1/2	4.7	0.000012
^{73}Ge	9/2	7.8	0.0011
^{129}Xe	1/2	26.4	0.0024
^{131}Xe	3/2	21.2	0.000014

Table 2.2: Values of $\lambda^2 J(J+1)$ in the case of pure proton coupling.

unpaired proton			
Isotope	J	Abundance(%)	$\lambda^2 J(J+1))$
^{19}F	1/2	100	0.036
^{23}Na	3/2	100	0.00067
^{127}I	5/2	100	7.87
unpaired neutron			
Isotope	J	Abundance(%)	$\lambda^2 J(J+1))$
^{29}Si	1/2	4.7	0.051
^{73}Ge	9/2	7.8	0.175
^{129}Xe	1/2	26.4	0.385
^{131}Xe	3/2	21.2	0.086

Table 2.3: Values of $\lambda^2 J(J+1)$ in the case of pure neutron coupling.

2.4   Nuclear form factor correction

When the wavelength, h/q, with the momentum transfer $q = (2M_{\mathrm{N}}E_{\mathrm{R}})^{1/2}$ is no longer large compared to the nuclear radius, the effective cross section begins to fall with an increasing q. Here h is the Plank Constant. This effect is represented by a form factor, F, which is a function of the dimensionless quantity, qr_{n}, where r_{n} is an effective nuclear radius. The neutralino-nucleus cross-section at a zero momentum transfer, $\sigma_{\chi-\mathrm{N}}$, is corrected with this form factor as

$$\sigma(qr_{\mathrm{n}}) = \sigma_{\chi-\mathrm{N}}F^2(qr_{\mathrm{n}}). \tag{2.62}$$

In the first Born (plane wave) approximation, the nuclear form factor can be defined as a Fourier transformation of $\rho(r)$, the density distribution of 'scattering centers'

$$F(qr_{\mathrm{n}}) = \int \rho(r)\exp(i\mathbf{q}\cdot\mathbf{r})d\mathbf{r}. \tag{2.63}$$

For small momentum transfers ($qr_{\mathrm{n}} < 2$), a commonly used approximation is

$$F^2(qr_{\mathrm{n}}) = \left[3\frac{j_1(qr_{\mathrm{n}})}{qr_{\mathrm{n}}}\right]^2 \exp\left[-(qs)^2\right], \tag{2.64}$$

where $j_1(x) = [\sin(x) - x\cos(x)]/x^2$, $r_{\mathrm{n}} \simeq 1.14A^{1/3}$ fm and $s \simeq 0.9$fm represents the nuclear skin thickness. The form factors as a function of the recoil energy for the SI interactions are shown in Fig. 2.6. Energy spectra expected with fluorine targets for the SI-interacting neutralinos are shown in Fig. 2.7, where the nuclear form factor correction, F^2, is taken into account.

For SD interactions, with the odd group model assumption, the form factor is approximated by the Bessel function partially filled with a constant value,

$$F^2(qr_{\mathrm{n}}) = j_0^2(qr_{\mathrm{n}}), \tag{2.65}$$

where $j_0(x) = \sin(x)/x$ and $r_{\mathrm{n}} \simeq 1.0A^{1/3}$ fm. The form factors as a function of the recoil energy for SD interactions are shown in Figure 2.8. Energy spectra expected with fluorine targets for the SD-interacting neutralinos are shown in Fig. 2.9, where the nuclear form factor correction, F^2, is taken into account.
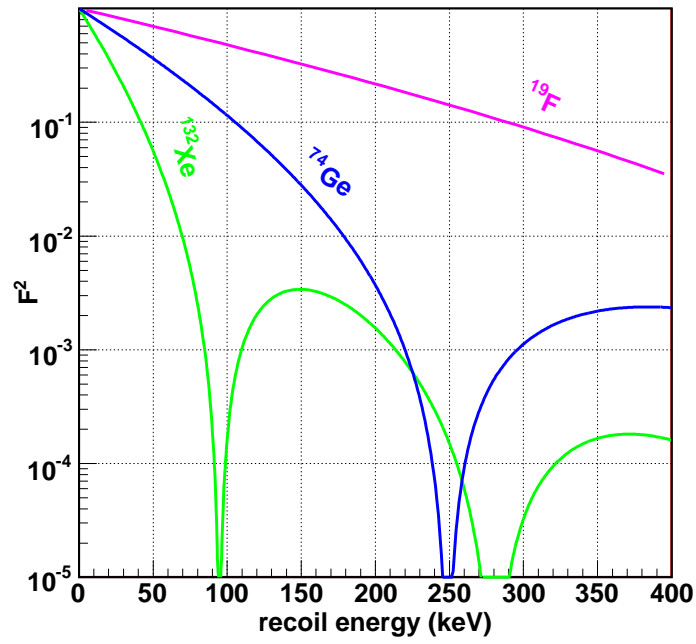
Figure 2.6: Form factors as a function of the recoil energy for the SI interactions for each nucleus.
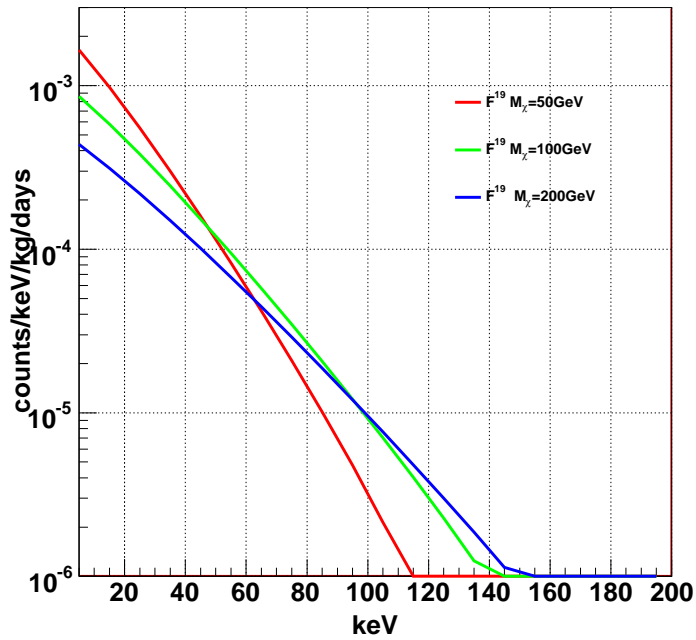
Figure 2.7: Energy spectra expected with fluorine targets for the SI-interacting neutralino for each mass of the neutralino.
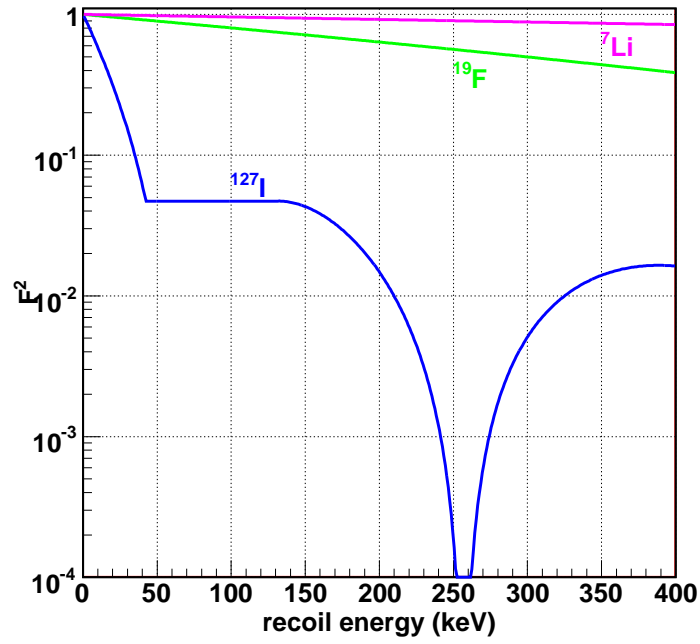
Figure 2.8: Form factors as a function of the recoil energy for SD interactions for each nucleus.
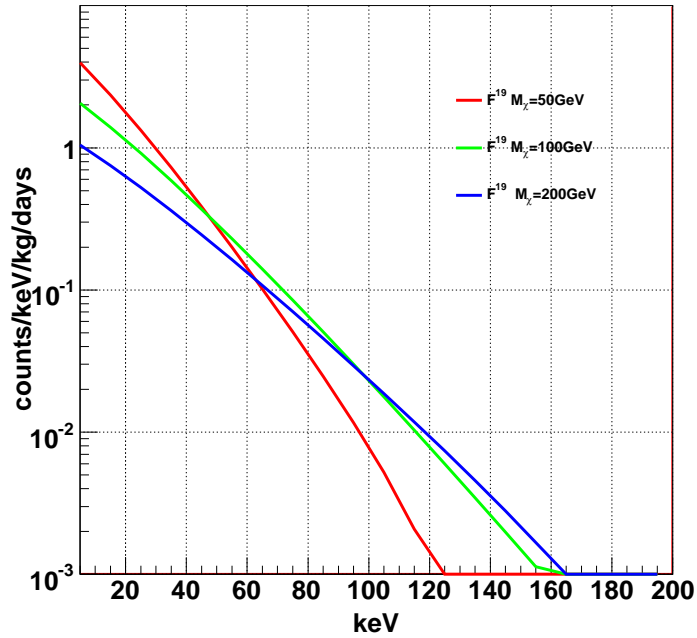
Figure 2.9: Energy spectra expected with fluorine targets for the SD-interacting neutralino for each mass of the neutralino.

2.5 Distinct signal of the dark matter

We need to observe a distinct signature in order to claim a clear detection of the dark matter because the expected spectrum itself has featureless exponentioal shape as described in Figure 2.7 and Figure 2.9. Distinct signatures can be caused by the nuclear-dependence of the neutralino-necleus reactions, relative motions of Solar system to the galactic halo, and that of the Earth. They can be observed as the signatures listed below.

- Nuclear target dependence of the event rate

- Annual modulation of the event rate and the shape of spectrum

- Directional dependence of the event rate

2.5.1 Nuclear target dependence

This signature arises from the difference of the cross sections $\sigma_0 F^2(E_{\mathrm{R}})$ and the target mass M_{N}. The expected recoil spectra dR/dE_{R} of various nuclei in existing detectors for the SI-interacting and the SD-interacting neutralino of $M_\chi = 100 \mathrm{GeV}/c^2$ and $\sigma^{\mathrm{SI}}_{\chi-\mathrm{p}} = 1 \times 10^{-6}\mathrm{pb}$ are shown in Figure 2.10 and Figure 2.11, respectively.

Although these figures indicate that the target-dependences seem to be easily observable, intrinsic backgrounds of target nuclei are also different, and thus reliable signatures are not easily obtained from the target-dependences.
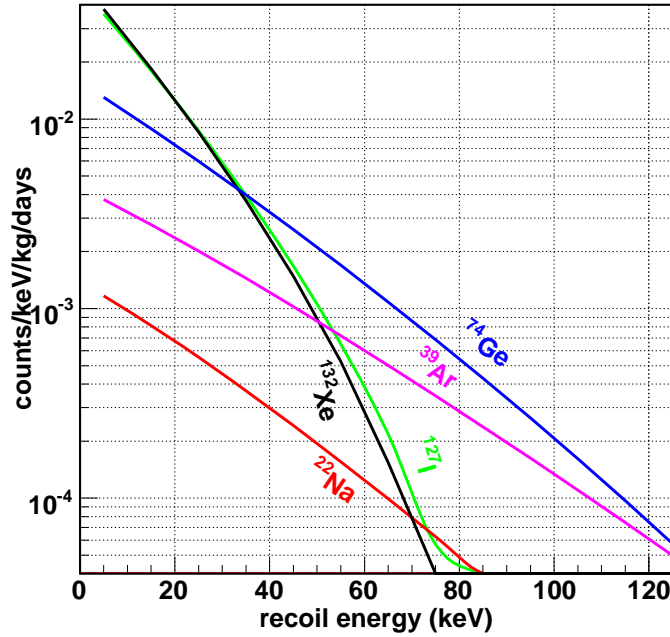
Figure 2.10: Recoil specra of various nuclei for the SI-interacting nuetralino with a mass of 100 GeV/c^2 and $\sigma^{\mathrm{SI}}_{\chi-\mathrm{p}}$=1×10^{-6}pb.
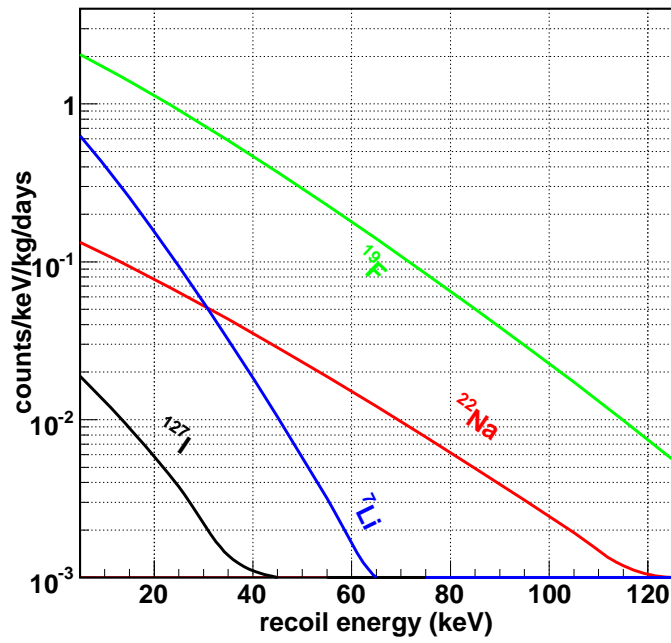
Figure 2.11: Recoil specra for of various nuclei for the SD-interacting nuetralino with a mass of 100 GeV/c^2 and $\sigma^{\mathrm{SD}}_{\chi-\mathrm{p}}$=1 pb.

2.5.2   Annual modulation

The annual modulation of the event rate is caused by the Earth's motion around the Sun as describe in Eq. (2.2). The order of modulation is less than $o(v_{\mathrm{orb}}/v_{\mathrm{SUN}}) \sim 10\%$ considering the inclined orbit of the Earth[42]. The component of v_{ES} parallel to the v_{SUN} reaches its maximum in June 2nd and its minimum in December 4th every year. Consequently, not only the total event rate, but also the shape of the recoil energy spectrum should vary. Figure 2.12 illustrates the eventual modulation of the recoil energy spectra of the florine target for the SD interaction with neutralino of M_χ=100 GeV and $\sigma^{\mathrm{SD}}_{\chi-\mathrm{p}} = 1$pb. The observation of this
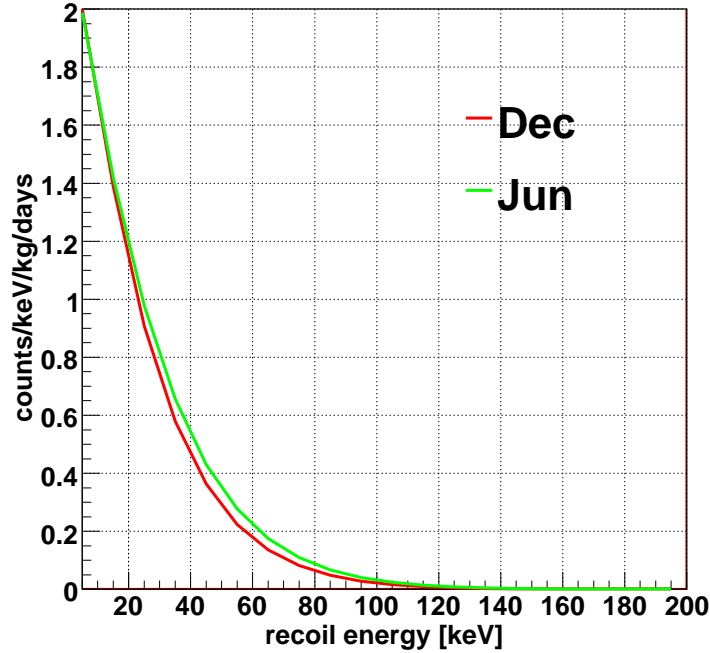
Figure 2.12: Difference of the fluorine spectra between summer and winter for the SD-interacting neutralino with a mass of 100 GeV/c^2 and $\sigma^{\mathrm{SD}}_{\chi-\mathrm{p}} = 1$pb. Green line is expected recoil specra in June, where v_{ES} has its maximum in the year. Red line is expected recoil specra in December, where v_{ES} has its minimum in the year.

small modulation of a very rare signal requires a large target mass, a long time measurement time, superb stability, extreme control of systematics. The results and discussions on the actual observations of this annual modulation signature are described in Section 3.1.

2.5.3   Directional asymmetry

The most convincing signature of WIMPs would be seen in the directional asymmetry of the recoil nucleus. The motion of the solar system relative to our galaxy makes an asymmetry in the directions of the incoming dark matters observed on the Earth, which can be expressed as "WIMP-wind". Figure 2.13 shows the directions in the sky of the Cygnus calculated for a day as they are observed Kamioka Observatory. The "WIMP-wind" is browing us from those directions.
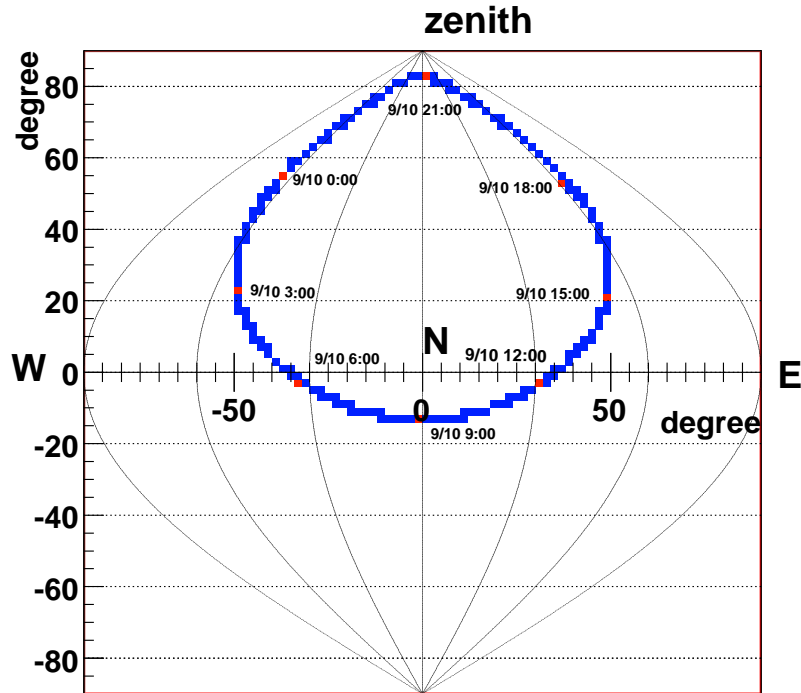
Figure 2.13: Daily motion of the direction of Cygnus, which is the same direction of the "WIMP-wind", expected in Kamioka Observatory(36°25'N, 137°18'E).

Spergel [43] has derived the differential angular spectrum with respect to laboratory recoil angle θ as

$$\frac{d^2R}{dE_R d\cos\theta} \sim \frac{1}{2}\frac{R_0}{E_0 r}\exp\left[-\frac{(v_E\cos\theta - v_{\min})^2}{v_0^2}\right], \qquad (2.66)$$

where a distribution of the isotheramal model Eq.(2.6) was assumed. Expected recoil angle-energy distribution of ^{19}F for the SD interacting WIMP cross section of $\sigma_{\chi-p}^{SD} = 1$pb with a mass of $M_\chi = 100$ GeV is shown in Figure 2.14.

The order of magnitude of the effect should be $O(v_E/v_0) \sim 1$ and the effect of the "WIMP-wind" is clearer in the recoil angle distribution $dR/d\cos\theta$. The expected anglular distribution of ^{19}F for the SD interacting WIMP cross section of $\sigma_{\chi-p}^{SD} = 1$pb with a mass of $M_\chi = 100$ GeV and a given recoil energy range of 100-120 keV is shown in Figure 2.15. It shows a large asymmetry which is not easily mimicked by any isotropic background. If the device has a direction sensitivity and is able to measure $\cos\theta$ distribution, we can discriminate dark matter signals from isotropic background events by fitting measured data with the model. A small signale-to-background ratio should be enough to discriminate signal from background event [44].

In this thesis we develop and study the direction sensitive dark matter search detector with this detection methode.
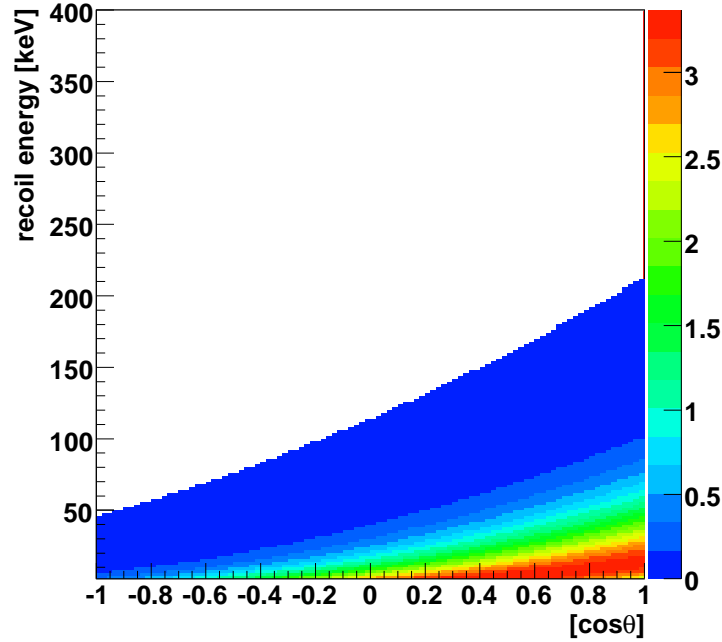
Figure 2.14: Expected recoil angle-energy distribution for the SD interacting neutralino with a mass of $M_\chi = 100$ GeV, and a cross section of $\sigma_{\chi-p}^{SD} = 1$pb, where θ is the recoil angle of the nuclear recoil with respect to the WIMP wind direction. X-axis shows $\cos\theta$, where θ is nuclear recoil angle. Y-axis shows nuclear recoil energy. Color contor shows event rate in unit of [counts/keV/kg/days/$\cos\theta$].
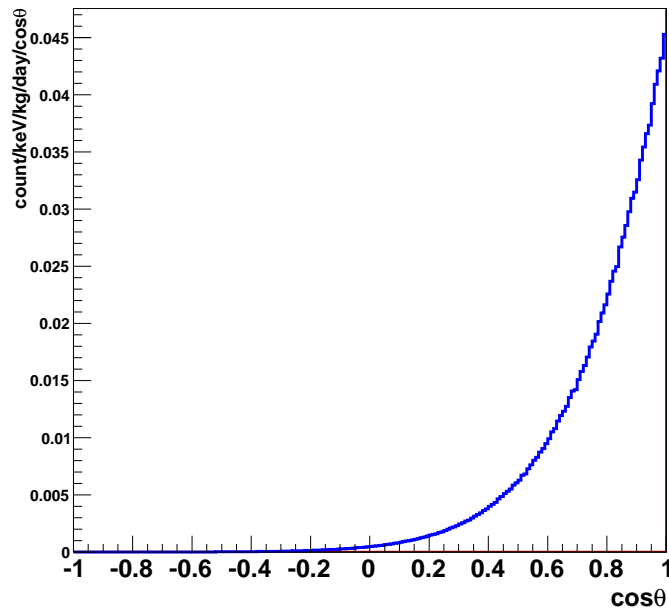
Figure 2.15: Expected $\cos\theta$ distribution for the SD interacting neutralino with a mass of $M_\chi = 100$ GeV, a recoil energy range of 100-120 keV, and a cross section of $\sigma^{\mathrm{SD}}_{\chi-\mathrm{p}} = 1\mathrm{pb}$, where θ is the recoil angle of the nuclear recoil with respect to the WIMP wind direction.

Chapter 3

Review of direct dark matter search experiments

A number of experiments have been trying to detect WIMPs by observing neutralino-quark elastic scatterings. Their detectors are designed to detect recoil nuclei via photons, phonons or charges in these experiments. Detector systems and results of some of the experiments are described in this section. Those results are summarized in Figure 3.1 and Figure 3.2.

In general, direct dark matter detectors should have following three characteristics.

- **Low energy threshold**
  As shown in Section 2.2, a featureless, quasi exponentially decreasing energy spectrum is expected by elastic scatterings. Therefore, the lower the energy threshold, the more of the signal is expected. The relevant energy region will be typically below 100 keV.

- **Large target mass**
  Since WIMP direct detection is a rare event search, one would need large target masses generally in order to gain sufficient statistics in a reasonable observation time of the experiment. A typical required mass scale is from kilogram to ton.

- **Low background**
  Typical precautions of rare event searches such as a material selection and shielding are essential to WIMP detectors in an underground laboratory. For nuclear recoil events, a generic background contribution originates from neutrons. On the other hand, the majority of background consists of electron recoils from photons (X-ray or γ-ray radiation) or electrons (β-ray radiation). Techniques to discriminate between these two types of energy deposition reduce the background obviously.

3.1 Solid scintillator experiments

Scintillators have advantages to constructing large mass detectors and well-studied their properties. Many types of scintillators, such as NaI(Tl), CsI(Tl) and so on, have been used for dark matter searches.

DAMA group operated a dark matter search with a highly radio-pure 100kg NaI(Tl) setup for seven years and claimed to have detected an annual modulation signature due to the dark matter[45]. Allowed parameter regions of WIMPs are shown as enclosed regions by black lines in Figure 3.1 and Figure 3.2. They also reported new results with a highly
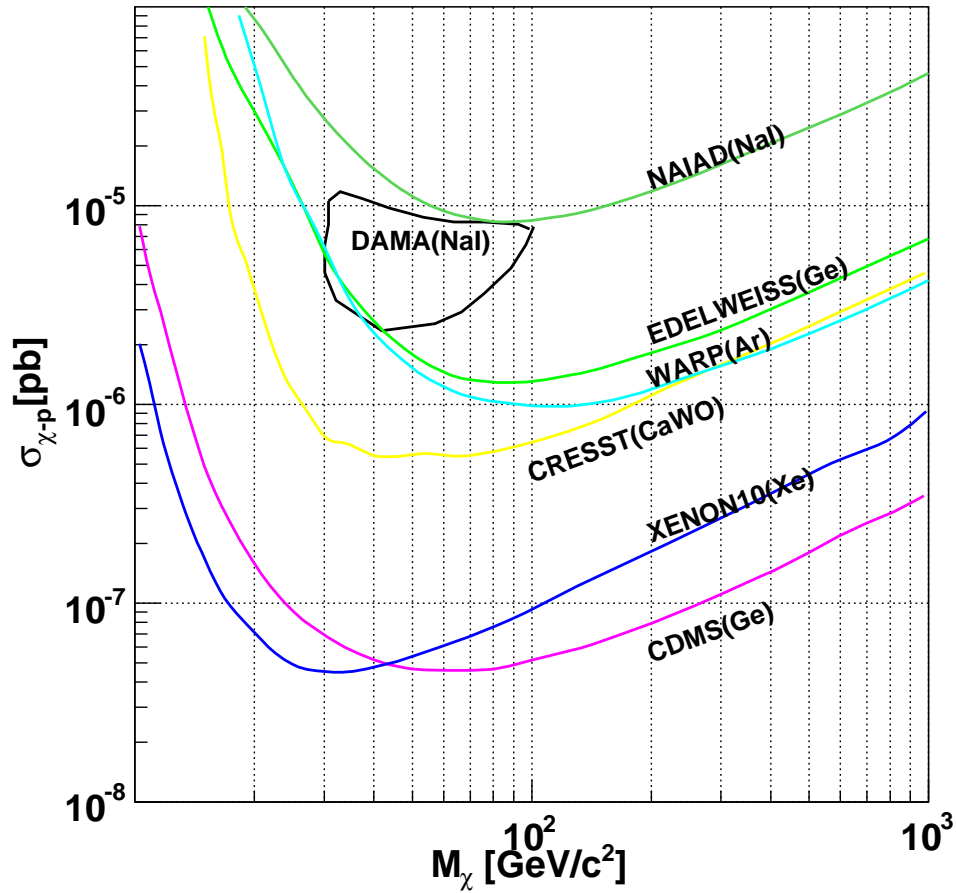
Figure 3.1: Results of SI(spin-independent) WIMP searches. Regions enclosed by black line is a region allowed by DAMA experiment[45]. Other experiments (NAIAD[47], EDELWEISS[55],CDMS[56], WARP[65], CRESST[59], and, XENON10[64]) exclude upper region of each line.
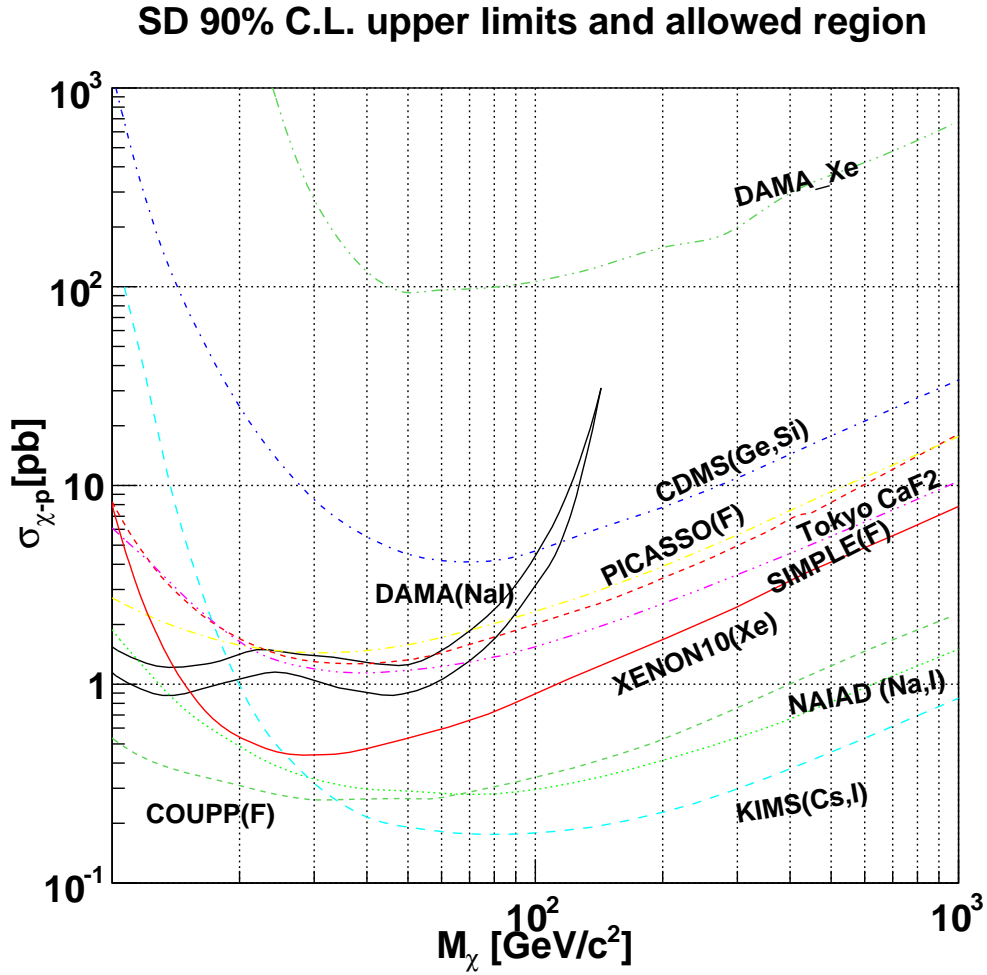
Figure 3.2: Results of SD(spin-dependent) WIMP searches. Regions enclosed by black line is a region allowed by DAMA experiment[45]. Other experiments (DAMA(Xe)[60], CDMS[56], Tokyo[49], PICASSO[71], SIMPLE[70], NAIAD[47], KIMS[48], XENON10[64], and COUPP[69]) exclude upper region of each line.

radio-pure 250kg NaI(Tl) setup (DAMA/LIBRA), which reproduced the peculiarities of the DAMA annual modulation signature as shown in Figure 3.3[46]. The DAMA/LIBRA experiment accumulated the largest exposure (0.82 ton·year) and claimed the only positive signature of the dark matter, while other experiments have not shown any results that have supported the DAMA/LIBRA results.

NAIAD detector was a 55 kg NaI(Tl) scintillator developed by UKDMC group in the year of 2000. They analyzed all data using a pulse shaping cut to reject background gamma-ray events. The pulse shaping cut applies a property, which a scintillation decay time for nuclear recoils is shorter than that for electron recoil. They derived an exclusion limits from an exposure of 44.9 kg·year (Green lines in Figure 3.1 and Figure 3.2).

KIMS collaboration constructed a 34.8 kg CsI(Tl) scintillator detector. They analyzed their 3409 kg·days data using the pulse shaping technique. They set the best limit of 1.7 pb to the SD WIMP-proton interaction for WIMPs with a mass of 100 GeVc^{-2} (Cyan line in Figure 3.2)[48].

CaF$_2$ scintillators do not show a good rejection power by the pulse shaping cut, while they have a potential advantage to the SD sensitivity because fluorine has a large $\lambda^2 J(J+1)$ as shown in Table 2.1. Shimizu et al.[49] reported a WIMP-search result with highly radio-pure CaF$_2$ crystals (Yellow line in Figure 3.2).

3.2 Bolometers (cryogenic detectors)

The heat capacity of a dielectric crystal is proportional to T^3 at low temperatures. Thus at mK temperatures the small energy deposition from a nuclear recoil can yield a measurable increase of a target crystal [50]. Some of the earliest WIMP search experiments were based on the technique, where energy released by particle interactions can be observed as phonons or a quanta of lattice vibrations. Works started on this idea in the 1980's [51], of which the original motivation were to obtain very low recoil energy thresholds and high energy resolutions. However, it was soon demonstrated, first in Si [52] and then in Ge [53], that the phonon detection could be combined with a simultaneous detection of the ionization to provide also a powerful means of the discriminatio n against electron recoils, on an event by event basis. This comes from the feature that the ratio of energy observed in the two channels depends on the energy deposition per unit length. A high dE/dx event, such as a recoil nucleus, produces proportionally more heat than the ionization (i.e. ionization is quenched). For instance, the ratio of the ionization to recoil energy (the ionization yield) for Ge recoils is 0.3 times of the value for electron recoils above 20 keV [54].

While bolometers without ionisation collections already showed a good potential for a dark matter search, the hybrid technique has obtained one of the best sensitivities in the dark matter experiments. Most notable experiments are EDELWEISS (at Frejus)[55] and the CDMS collabolation (at Soudan mine)[56]. The EDELWEISS experiments used 320g Ge crystals operated at 17 mK with NTD-Ge thermometric sensors attached for the heat signal and aluminium electrodes used to collect the charge. A variety of detectors were tried in EDELWEISS-I with several runs from 2000 to March 2004. These measurements yielded a total exposure of 62 kg·days, and the main result coming from three crystal with a recoil energy threshold of 13 keV or better over 4 months of a stable operation. Some nuclear recoil candidates were recorded, but they seem to be due to the remaining background or surface electrons.

The CDMS experiment operates towers of Ge and Si crystals with thickness of 1 cm. The mass of the Ge and Si crystals were 250 g and 100 g, respectively. Technique for the ionisation collection was same as the EDELWEISS but here thermal phonons were detected using superconducting transition edge sensors, formed by photolithography on the
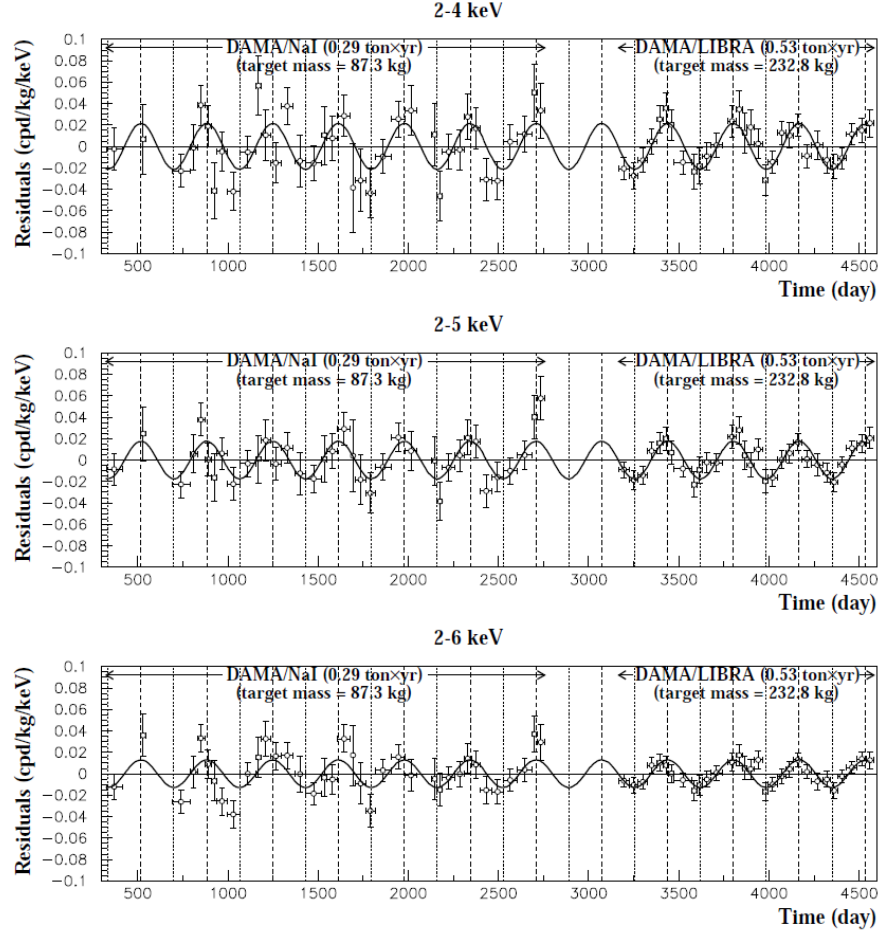
Figure 3.3: Residual rates maeasured by DAMA/LIBRA experiment in the (2-4), (2-5) and (2-6) keV energy intervals as afunction of the time. X-axises show days (t) from January 1st of the first year of data taking of the former DAMA/NaI experiment. The experimental points present the errors as vertical bars and the associated time bin width as horizontal bars. The superimposed curves represent the cosinusoidal functions behaviours $A \cos \omega(t-t_0)$ with a period $\frac{2\pi}{\omega} = 1$ yr, with a phase $t_0 = 152.5$ day (June 2nd) and with modulation amplitudes, A, equal to the central values obtained by best fit over the whole data, that is: (0.0215 ± 0.0026) cpd/kg/keV, (0.0176 ± 0.0020) cpd/kg/keV and (0.0129 ± 0.0016) cpd/kg/keV for the 2-4 keV, for the 25 keV and for the 26 keV energy intervals, respectively. The dashed vertical lines correspond to the maximum of the signal (June 2nd), while the dotted vertical lines correspond to the minimum. The total exposure is 0.82 ton·yr[46].

crystal surface. This design has a potential advantage to providing a sensitivity of the depth position, via a measurement of the phonon pulse rise time, and hence a possibility of rejecting surface electron events. The 15 Ge crystals were operated from Octobar 2006 to July 2007 yielding an exposure of 121.3kg·days in the recoil energy region of 10-100 keV. No events were observed and thus a 90% C.L. SI WIMP-proton limit of 4.6×10^{-8}pb for WIMPs with a mass of 60 GeVc^{-2} were obtained (purple line in Figure 3.1) [57].

ROSEBUD[58] and CRESST[59] groups have developed "scintillating bolometers" which detect scintillation photons together with heat as an alternative method for the electron-event rejection. In the CRESST experiment, a silicon wafer of $30 \times 30 \times 0.4$mm^3 with tungsten thermometer was used to detect the photon, while a 8 mm$\times$8 mm$\times$200 nm superconducting evaporated tungsten film was used as the heat sensor. Results so far have been obtained with two 300 g CaWO$_4$ crystals at Gran Sasso with a total exposure of 20.5 kg·days. 16 events observed in the recoil energy range of 12-40keV could be explained by the ambient neutron background becasue they measured without a neutron shield. Due to a relatively high sensitivity to the SI interactions of W nuclei, they derived a limits comparable to other experiments [59](yellow line in Figure 3.1).

All these cryogenic experiments are being upgraded to increase the target masses to the order of 100 kg, while feasibility studies on the next scaling-up to 1 ton scale are also being performed.

3.3 Liquid noble element detectors

While great efforts in the world have been devoted to cryogenic bolometers over many years, a rapid growth in liquid noble gas technology for WIMP searches was achieved. The liquid noble elements are excellent scintillators, while simultaneous ionization signals can be collected with an existence of a certain electric field. Most notable has been liquid xenon (LXe), started by DAMA/Xe [60], but also recently liquid neon and, in particular, liquid argon.

LXe has particularly good intrinsic properties for the WIMP detection, that are a large atomic number (Z=54, A=131.3), high density, high radio purity, and, high light output. ZEPLIN I experiment, which used a 3.2 kg of active LXe viewed by three photo multipliers (PMTs), accumulated a 293 kg·days exposure during an operation at Boulby mine until 2002, and published a result based on the pulse shaping analysis for the nuclear recoil discrimination [61]. XMASS project [62] designed a spherical LXe detector based on a self-shielding with a large scale LXe (800 kg). γ-rays coming from outside of the detector within the dark matter search energies are expected to be sufficiently shielded by the outer region of the detector. These experiments with only the liquid state of xenon are commonly referred to as "single phase" detectors in contrast to the "two phase" detectors which have a gaseous phase simultaneously.

Two phase detectors detect not only a scintillation signal but also an ionization signal. The ioninzation signal is detected as a gas amplification scintillation signal in the gas phase region caused by the primary electron drifted out of the liquid phase. Because the ionization signals for nuclear recoils are quenched significantly much more than the primary scintillation signals, while the ionization signals for electron recoils are not quenched so much, a ratio of the ionization signal and the primary signal provides a powerful electron discrimination power. This technology is used by ZEPLIN II/III[63] and XENON 10/100 experiments[64]. These experiments aim to achieve higher sensitivities with small fiducial masses than those expected with single phase detectors. XENON10 with a 15 kg detector accumulated 165 kg·days of data until 2007. They applied a background subtraction and derived a very stringent SI WIMP interacting limit of 5.5×10^{-8}pb for WIMPs with a mass

of $100\text{GeV}/\text{c}^2$ (blue line in Figure 3.1) [64].

Despite the current interest in LXe, the intrinsic discrimination power may not be as good as that of bolometers. In this respect liquid argon (LAr) detectors may provide better prospects. Some properties of LAr are inferior to LXe for the WIMP search, notably smaller atomic mass (A=40) and the need to use a wavelength shifter for the vacuum ultra violet scintillation light (128 nm). However, both the pulse shaping discrimination and the two phase signals discrimination are now known to be more powerful, which is expected to be capable in principle combined the discrimination factor up to 10^8. LAr is also a factor 400 times lower in cost than LXe. Based on these properties, WARP collabolation has build and deployed a 3.2kg LAr detector at LNGS and recently reported a sensitivity near 10^{-6} pb for WIMPs with a mass of 100 GeVc^{-2} and an exposure of 96.5 kg·days (Cyan line in Figure 3.1) [65]. Other LAr experiments such as ArDM[66], CLEAN[67] and DEAP[68] are also under construction.

3.4   Superheated droplet detectors

Superheated liquids, in the form of bubble chambers, were used in accelerator experiments. In a bubble chamber kept in a delicate metastable superheated state, an ionizing radiation particle makes a local vapor phase with the energy deposited along its path. Rapidly growing bubbles are photographed and the chamber is then reset by a fast recompression to the metastable liquid phase. COUPP[69], SIMPLE[70], PICASO[71] experiments applied a superheated droplet detector to the direct dark matter search using piezoelectric sensors as the trigger.

These devices have advantages to the nuclear recoil discrimination, a large mass, and a target selection for the SD WIMP searches, but have disadvantage to detecting the nuclear recoil energy. The superheated liquid can be tuned to respond exclusively to particles with a large stopping power, while muon and electron events all fall well below the bubble nucleation threshold.

The COUPP project reported the lowest limit on the SD WIMP-proton cross section for WIMPs with a mass of 10 GeV/c^2, assuming the amount of the background event due to ^{222}Rn gas. This result excluded the result of DAMA observation completely in the SD WIMP search. (Dark green line in Figure 3.2)[69].

3.5   Gas detectors

Low-pressured gas detectors have an advantage to a direction-sensitive dark matter search, while several challenges to overcome exist. The requirement for use of low pressure gas implies large volume detectors of more than 1 m^3 will eventually be needed. Another issue is to discriminate the head and tail of a track, or the track sense. Orientation of a recoil track alone provides significant directional information, which nearly an order of magnitude greater sensitivity can be achieved in principle if the track sense are known.

3.5.1   Gas selection for the direction-sensitive WIMP search

There are some candidates for target gases of a directional WIMP search. A target gas should have a large cross-section of WIMP-nucleus scatterings and a small cross-section of the neutron interaction because it is impossible to discriminate the WIMP-nucleon interaction from neutron-nucleon one event by event. Since hydrogen has a large cross-section to neutron, a gas which contains one or more hydrogens (e.g. CH_4, C_2H_6) should be avoid.

Noble gases (Xe, Ar, and so on) are well-used gas for common particle detectors, and Xe is the most proper nucleus of noble gases for the SI interaction search because it has a large atomic mass ($A = 131.29$) and few radio isotopes in natural Xe as described in section 3.3. However, the electron transfer diffusion in noble gas are so large that an appropriate position resolution can not be obtained with a large detector. Drift velocities and drift diffusions calculated by the MAGBOLTZ simulator [82] are shown in Figure 3.4 and Figure 3.5, respectively. For example, in case of the Xe gas with an electric field of 2 kV/cm/atm, the electron transfer diffusion calculated by MAGBOLTS is larger than $\sigma_{\rm diff}{=}400\mu m/\sqrt{\rm cm}$.

On the other hand, a negative ion time projection chamber (NITPC), where the primary electron is rapidly captured by electron negative gases and transferred as negative ions along a strong electric field, has potential to realize a very small diffusion because, unlike electrons, drifting ions remain in or near thermal equilibrium with the gas up to extremely high drift fields. Transverse and longitudial diffusions are therefore suppressed to the thermal levels, which is less than $100(\mu m/\sqrt{\rm cm})$ in case of CS_2.

CF_4 gas, although it is not electron negative gas, has small electron diffusions less than $200\mu m/\sqrt{\rm cm}$ becasue the electron drift velocity in CF_4 gas is fast. CF_4 gas is easy to handle because it is inert and harmless, while CS_2 gas is ignitable and harmful. We note that CS_2 gas has advantages to the SI interaction search (Atomic mass of sulfur is 32) and CF_4 gas has advantages to the SD interaction search.
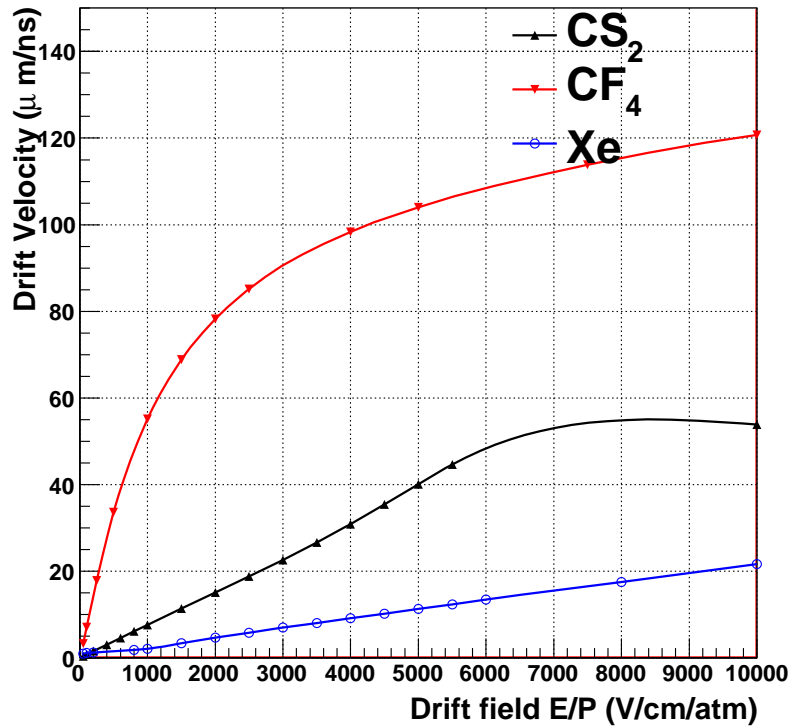
Figure 3.4: Drift velocity of electrons of negative ions calculated by MAGBOLTZ for CF_4(red), Xe(blue), CS_2(black) at a temperature of 300K.

The position resolution is also an important property of a direction-sensitive detector.
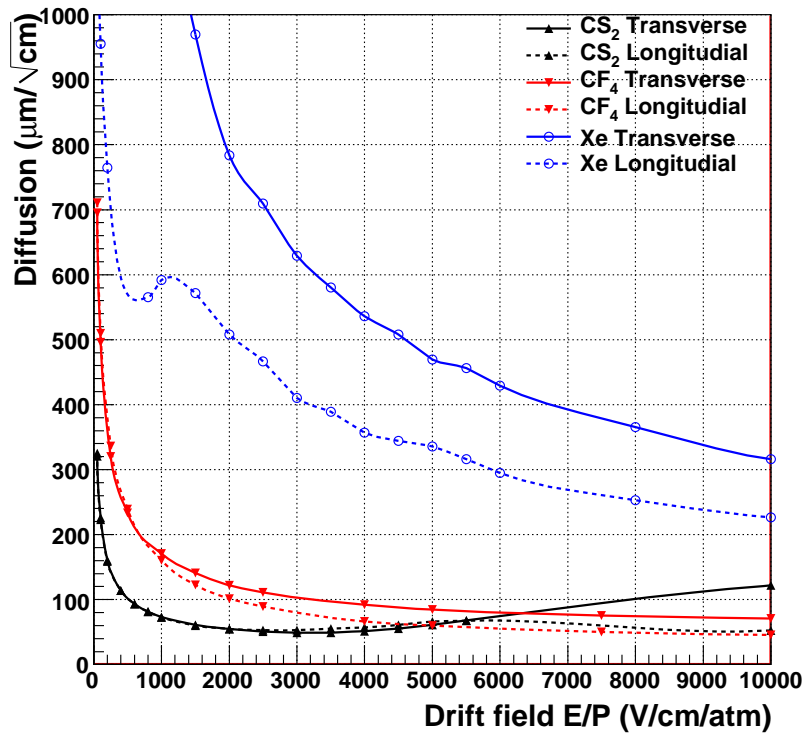
Figure 3.5: Longitudial (dotted line)and Transverse (solid line) diffusion of electrons or negative ions calculated by MAGBOLZ for CF_4(red), Xe(blue), CS_2(black) at a temperature of 300K.

Roughly saying a direction-sensitive detector should have a position resolution better than a typical nuclear track length of interest. The lengths of nuclear tracks in several types of chamber gas calculated by SRIM[77] as a function of the initial energy are shown in Figure 3.6. Although Longer tracks are expected in lower pressured gas, a low pressured gas detector needs a large volume and also often causes the unstability of the operation. We need to overcome these difficulties in order to detect the very distinct signals of the dark matter.

An overall discussion leads that the use of Xe gas requires much more technological development issues than those of CF_4 and CS_2 gas because a finer position resoltuion and lower pressure operation are required.
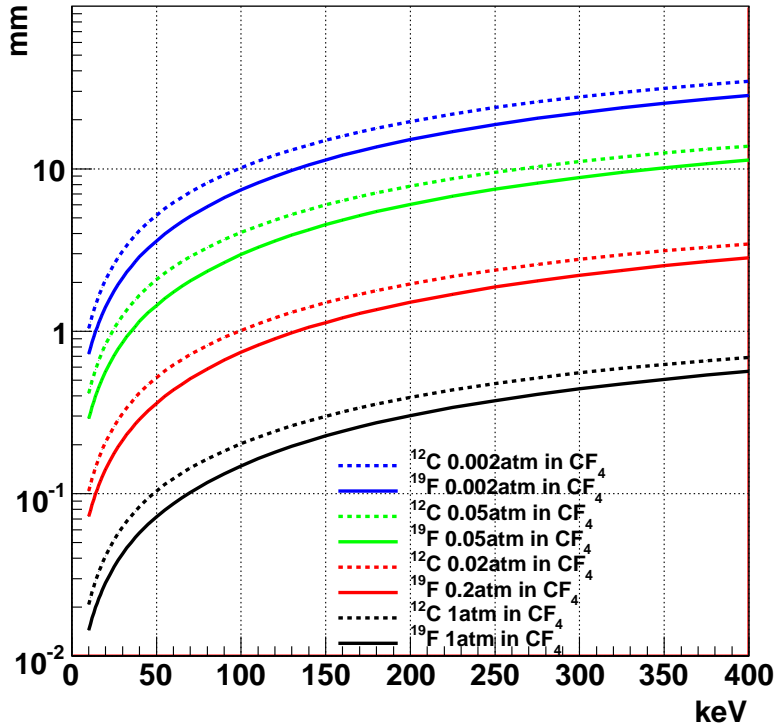
Figure 3.6: Length of recoil Carbon (dotted line) and Fluorine (solid line) nuclei in CF_4 gas calculated by SRIM with each pressure (blue:0.002atm, green:0.05atm, red:0.2atm, black:1.0atm).

3.5.2 Gaseous detector experiments

Since there are some issues to technologically overcome, any gaseous detector project has never reached the sensitivity for the DAMA signal regions. We describe some gasous detectors and development status in the following paragraph.

US-UK DRIFT experiment [72] pioneered the study of the directional detection of the dark matter with 1 m^3 of CS_2 at 40 torr (170g fiducial mass) detectors. They demonstrated the ability to reconstruct the direction of the incoming particles by detecting the direction
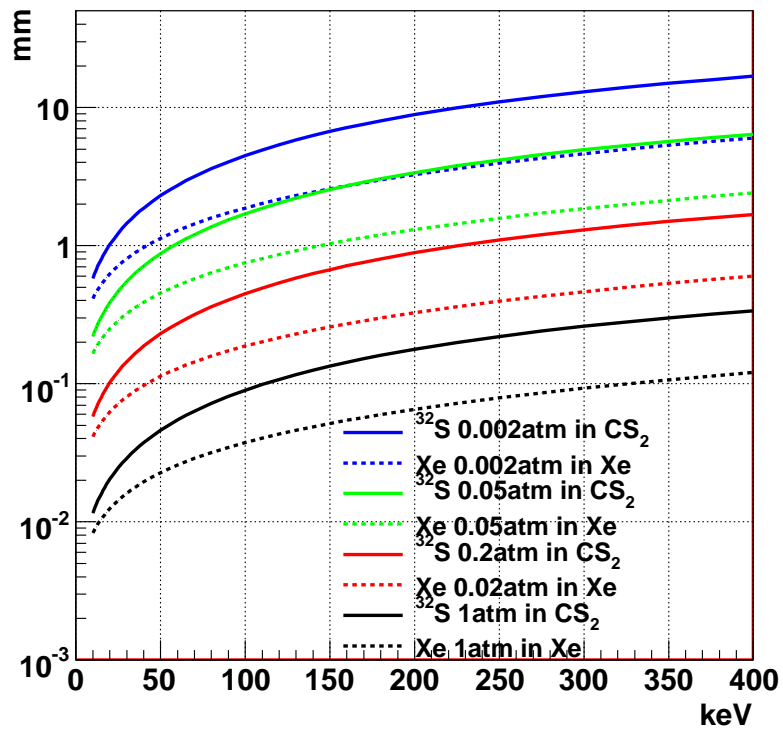
Figure 3.7: Length of recoil Xe and S nuclei in Xe gas and in CS_2 gas. They were calculated by SRIM with each pressure (blue:0.002atm, green:0.05atm, red:0.2atm, black:1.0atm)

of recoil nuclei in a gaseous detector. However, there existed an intrinsic limit of ability due to their readout pitch of 2 mm.

DMTPC collaboration[74] proposed a new method to detect the track sense using a CCD-readout TPC. They demonstrated that the projected images of nuclear recoil tracks could be precisely taken via scintillation photons produced during the avalanche process in CF_4 gas. Though their detector is now small and there are many issues to develop in oreder a dark matter search detector, their technique is very notable for the detection of the track sense.

NEWAGE detector with CF_4 gas and a fine pitch gasous detectors, which will be described in Chapter. 4 has potentials to scaled up to $1m^3$ with a low-cost mass-production. Here we compare the NEWAGE detectors with the gaseous detectors of other projects, DRIFT and DMTPC. Properties of the current and and developing detector of each project are shown in Table 3.1. NEWAGE has advantages to the readout pitch and the effective volume against DRIFT and DMTPC, respectively.

	NEWAGE-0.3a NEWAGE-0.3b	DRIFT-I DRIFT-IIa	DMTPC DMTPC2
gas	CF_4	CS_2	CF_4
pressure(torr)	152 40	40	50
volume(m^3)	0.23×0.28×0.31 0.23×0.28×0.51	1×1×1	0.16 × 0.16×0.16 ϕ0.25 × 0.25
readout	GEM&uPIC(charge)	multi-wire(charge)	CCD-readout(light)
dimension	3D	2D 3D	2D
pitch	400μm	2mm	256μm
ref	[75]	[72]	[74]

Table 3.1: Comparison of gaseous directional sensitive dark matter detectors. Details of the the DRIFT and the DMTPC can be found in the references.

Chapter 4

NEWAGE-0.3a detector

4.1 NEWAGE-0.3a detector

NEWAGE (NEw generation WIMP search with advanced Gaseous TPC Experiment) is a direction-sensitive dark matter search project. As described in Section 2.5, a direction-sensitive method has a potential to provide strong evidence for the dark matter. However, there was no directional-sensitive detector with a sensitivity covering the DAMA region, let alone the MSSM region. Purposes of NEWAGE are to develop direction-sensitive detectors, to search for the WIMP-wind, to detect a strong evidence, and finally, to study the properties of the dark matter. NEWAGE goals of the sensitivity for the spin-dependent WIMP-proton cross sections are shown in Figure 4.1 [75].

As a first step, we developed a prototype detector (NEWAGE-0.3a) and investigated its performance precisely focusing on the requirements for a direction-sensitive dark matter search experiment. We describe the properties of CF_4 gas and the properties and performance of the NEWAGE-0.3a detector in this chapter.

4.1.1 Property of CF_4 gas

The TPC (Time Projection Chamber) gas is the most important material in the detector because it determines the performance of the detector and also the sensitivity to WIMPs, as described in Section 3.5. We use CF_4 gas for the NEWAGE-0.3a detector.

Basic properties of CF_4 gas are listed in Table 4.1. CF_4 gas has an advantage to the SD WIMP search, because a CF_4 molecular has four fluorine nuclei which have a large $\lambda^2 J(J+1)$ (See Section 2.3). Since CF_4 gas has a faster drift velocity, smaller drift diffusion than noble gases (e.g. Ar, Xe. See Figure 3.5) is expected. This is an important property to develop a large-sized detectors.

On the other hand, CF_4 gas has two disadvantages: a large W-value and small Townsent coefficient. The W-value, which is an average energy required to make an electron-ion pair in the detector gas, of CF_4 is about twice larger than that of Ar and Xe. This property means the number of electrons is only a half of that expected in Ar gas. The townsend coefficient, a factor that governs the gas multiplication process, of CF_4 is smaller than that of Ar and Xe. This property indicates that we need to supply a higher voltage to anode electrodes than the voltages with Ar or Xe gas. Therefore, the use of CF_4 gas as TPC gas generally requires a more intensive study than those of the other standard gases. This requirement was slightly relaxed in our case because the muons and electrons are not our primary target, but the recoil nuclei, with larger energy deposition per unit length, are.

SD 3σ detection sensitivities
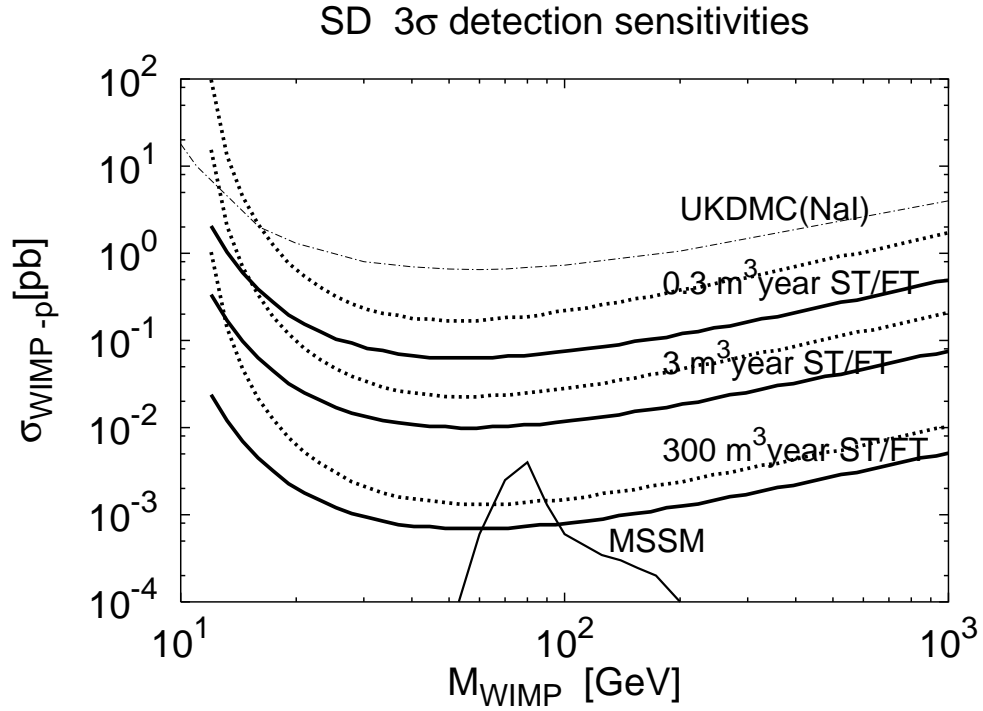
Figure 4.1: Sensitivity goals of the NEWAGE project. Thick and dotted lines show expected 3σ asymmetry detection sensitivities by the ST(semi-tracking) and FT(full-tracking) modes, respectively. Details are described in [75]. An experimental result of NAIAD (thin dashd-dotted line labeled UKDMC) and MSSM predictions(thin line labeled MSSM) are also shown [47],[76].

molecular forum	CF_4
name	Tetrafluoromethane, Carbon tetrafluoride
appearance	colorless odorless gas
molecular mass	88.01 g/mol
density	3.76g/l (15°C 1atm)
melting point	-183.6°C
boiling point	-127.8°C
W-value	54

Table 4.1: The properties of CF_4 gas.

4.1.2 NEWAGE-0.3a detector

The NEWAGE-0.3a detector is a μ-TPC (micro Time Projection Chamber) read by a 30.7×30.7 cm^2-sized μ-PIC (micro PIxel Chamber, TOSHIBA/DNP, SN060222-3) which is a two-dimensional fine-pitch imaging device [78]. The properties of the NEWAGE-0.3a are shown in Table 4.2 and its photograph is shown in Figure 4.2. The schematic view of
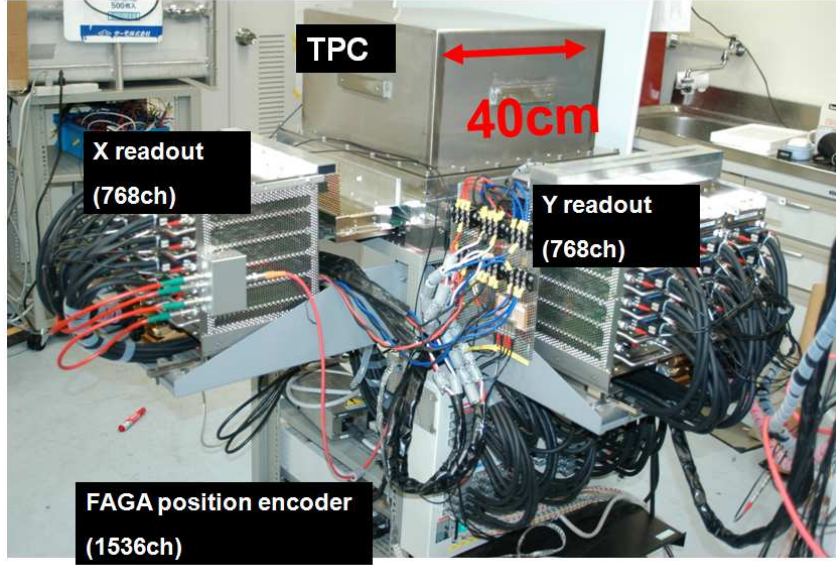
Figure 4.2: Photograph of the NEWAGE-0.3a detector, which consists of a TPC vessel and read-out circuits.

the μ-TPC is also shown in Figure 4.3. A μ-PIC is manufactured by printed circuit board (PCB) technology. PCB technology realizes an economical mass production, which is one of the most important requirements for the fabrication of a dark matter detector. The μ-PIC has 768×768 pixels with a pitch of 400 μm read by 768 anode strips and 768 cathode strips. The anode and cathode strips are orthogonally formed and thus we can detect the two-dimensional position of each event by taking the coincidence of the anode and the cathode strips. The schematic structure of μ-PIC is shown in Figure 4.4. Details of μ-PICs are shown in Appendix B.

The μ-PIC is used as a main gas-amplifier and as readout electrodes. A GEM [79] with an effective area of 23×28 cm^2 (Scienergy Co. Ltd.), is set 5 mm above the μ-PIC and used as a sub-amplifier. We make an electric field with a length of 31 cm above the GEM with field-shaping patterns on circuit boards to form a detection volume of $23 \times 28 \times 31$ cm^3. A volume of $20 \times 25 \times 31$ cm^3 is set as the fiducial volume for the dark matter search in the analysis. The μ-TPC is set in a 3 mm-thick stainless-steel vacuum vessel filled with CF$_4$ gas at 152 torr. A SORB-AC Cartridge pump (saes getter MK5) is attached to the vessel to absorb contaminants in the chamber gas.

The μ-TPC signals from 768 anode strips and 768 cathodes strips are read by a dedicated electronic system [80]. The schematic structure of the data acquisition system for NEWAGE-0.3a is shown in Figure 4.5. The signals are digitized in the amplifier shaper discriminator (ASD) chips (CXA3183Q), synchronized in a position encoding system with 100MHz clocks, and recorded by a VME-bus memory board. Each digital signal or hit is a set of (Xmin, Xmax, Ymin, Ymax, T), where Xmin and Xmax are the minimum and maximum positions

$V_{DRIFT} = -8.2kV$

drift plane (z=31cm)

8.25MΩ ×31

Field shaping pattern ×30

Z

$V_{GEMT} = -915V$

Y

X

$V_{GEMB} = -650V$

GEM (Z=0cm)

30MΩ

$V_{\mu-PIC} = 515V$

μ−PIC(z=−0.5cm)

cathode strip ×768

anode strip ×768
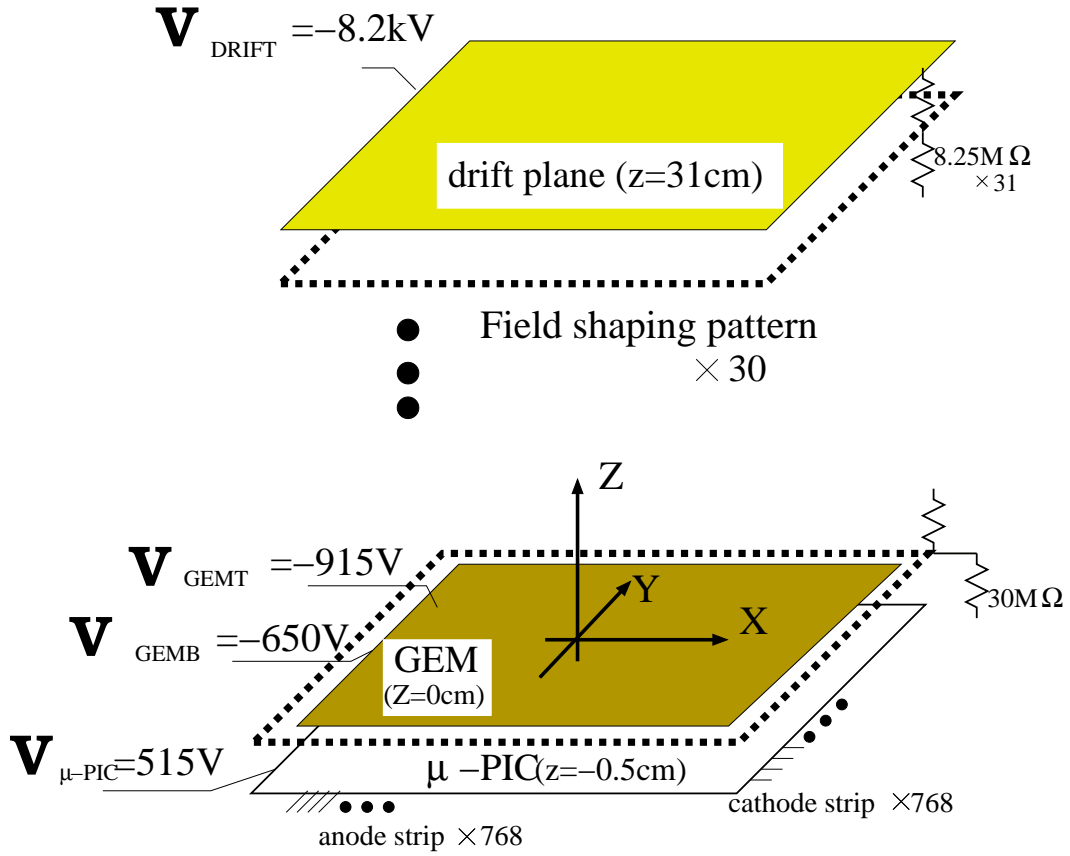
Figure 4.3: The schematic structure of the NEWAGE-0.3a. V_{DRIFT} is a voltage supplied at the drift plane, V_{GEMT} is at the top of the GEM, V_{GEMB} is at the bottom of the GEM, $V_{\mu-PIC}$ is at the anode of the μ-PIC.
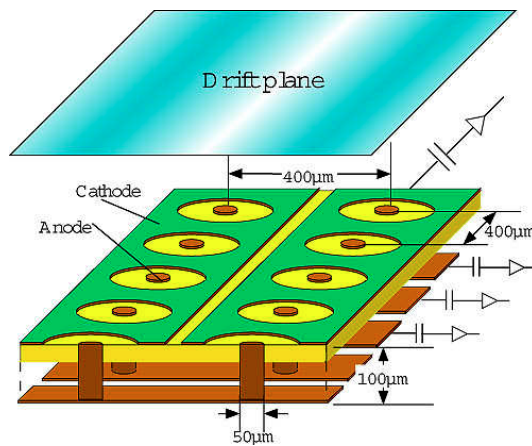
Figure 4.4: The schematic structure of a μ-PIC.

Outer vessel	
size	$42.6 \times 42.6 \times 34.65$ cm^3
thickness	3mm(top&side),16.5 mm(bottom)
material	stainless steel
Gas volume	
Gas	CF$_4$
pressure	152 torr
Drift volume	
size	$35.0 \times 35.0 \times 31.0$ cm^3
material	Fluoroplastic*1(wall), Cooper(top)
electric field	$\sim$240 V/cm at 152torr
Detection volume	
effective volume	$23 \times 28 \times 31$ cm^3
fiducial volume	$20 \times 25 \times 31$ cm^3
fiducial mass	11.48g
readout module(μ-PIC)	
S/N	SN060222-3
size	30×30 cm^2
operation gas gain	$\sim \times 700$
readout pitch	400 μm
Gas preamplifier (GEM)	
material	polyimide
size	23×28 cm^2
hole pitch	140μm
hole size	70μm
thickness	50μm
operation gas gain	$\sim \times 3$

Table 4.2: Properties of the NEWAGE-0.3a detector

*1:GP-500 [81]

of the anode strips which detected the TPC signals, the Ymin and Ymax are those of the cathode strips and the T is the clock counter. We introduced a new tracking procedure which took account of the spread of the electron cloud by using a data set of (Xmin , Xmax, Ymin, Ymax) for one clock, instead of ((Xmin+Xmax)/2,(Ymin+Ymax)/2) used in our previous work [75]. In the previous tracking procedure we were not able to decide directions of tracks that run parallel to X-Y plane because X-Y spreads in one clock were ignored. In this new method, we analyzed a data set of (Xmin , Xmax, Ymin, Ymax, T) as independent 4 points (Xmin, Ymin, T), (Xmax, Ymin, T), (Xmin, Ymax, T), and (Xmax, Ymax, T). We thus obtained 4 points for a clock and determined the direction by fitting all of these measured points with a straight line. The track-length is defined as the distance of end-points of the fitted segment. Analog TPC signals of 768 cathodes are amplified and grouped down to 4 channels and their waveforms are recorded by a 100 MHz flash ADC. The energy deposition of a charged particle is thus known from the detected waveforms. Typical operation parameters are shown in Figure 4.3, which are optimized to realize a stable operation with a combined (μ-PIC×GEM) gas gain of 2000 and the drift field of 0.24 kV/cm.

The gas gains of the μ-PIC and the GEM for CF_4 are measured by a previous work and are shown in Figure 4.6 and Figure 4.7. This measurement was performed by irradiating a small-sized TPC which consisted of a 10×10 cm^2 μ-PIC and a 10×10 cm^2-GEM with 5.6 keV X-rays from a ^{55}Fe source. The operation gas gain for the dark matter search is about 2000, which is out of the range of these measurements, so we used these results as a rough guide to determine the operating voltages. Absolute gas gain is measured by using the α-ray calibration (See Section 4.2.2).
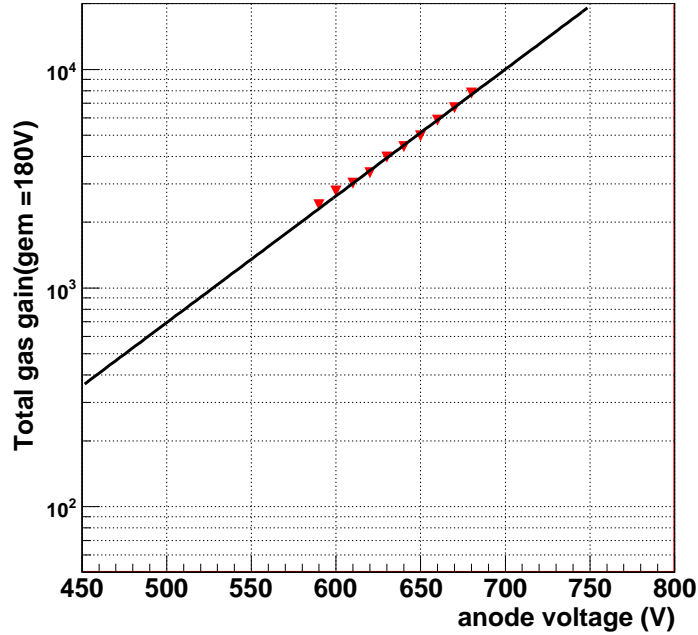
Figure 4.6: Gas gain as a function of μ-PIC anode voltage. The voltage between the top and bottom electrodes of GEM is fixed at 180 V.

We defined the detector coordinate as follows. We set the origin at the center of the
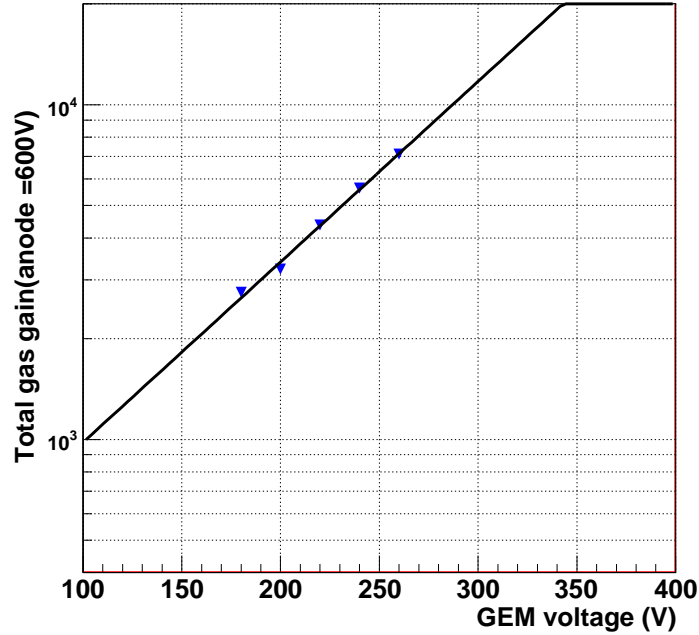
Figure 4.7: Gas gain as a function of a voltage between the top and bottom electrodes of GEM. The μ-PIC anode voltage was fixed at 600V.

GEM, X-axis along the cathode strips, Y-axis along the anode strips and Z-axis along the drift field as shown in Figure 4.3. The detector is set so that the μ-PIC plane is placed horizontally. We also describe a position in the laboratory with the detector coordinate as (X(cm),Y(cm),Z(cm)).

The NEWAGE-0.3a has two type of the operation modes which differ in the trigger signal. One is "external-trigger mode". We use this mode only for a measurement with a ^{252}Cf source and we use a signal of a prompt gamma ray or a neutron detected by a plastic scintillator set nearby the ^{252}Cf source as a trigger. We can measure the absolute Z position of the recoil nuclear tracks in this operation mode. We measured the drift velocity and the angular resolutions in this mode. The other is "self-trigger mode". In this trigger mode, the TPC analog signals from 768 anode strips are grouped down to 16 channels and are used as the triggers. The absolute Z position is not measured, but only the relative position is measured. In this thesis we used the self trigger mode unless we mention otherwise.

The data taken by μ-TPC is analyzed with some event selections as follows.

- Nhit selection: We select the events which have at least three hit points. We implicitly used this selection to all data in this thesis.

- Fiducial selection: We select the events whose hit points were all in the fiducial volume. We implicitly used this selection to all data in this thesis.

- Energy selection: We select the events which satisfy the energy condition.

- Length selection: We select the events which satisfy the length condition.

- Nuclear selection: This selection consists of an energy selection of E>100 keV and a length selection of L<1 cm. The length limit is to reject gamma rays, and the energy threshold is determined to keep a performance of nuclear tracking. These details are described in Section 4.3. This selection was used at the nuclear recoil measurements in Section 4.4.1 and the dark matter search run.

4.2 Energy calibration and stability

4.2.1 Drift velocity

The electron drift velocity in the μ-TPC needs to be measyred to reconstruct a three-dimensional track from the μ-TPC data set (Xmin , Xmax, Ymin, Ymax, T). Although a drift velocity of an electron in CF_4 is calculated in Figure 3.4, it is very sensitive to the impurity of gas. We measured the drift velocity with the external-trigger mode. We used a plastic scintillator and a ^{252}Cf source with an intensity of 2.2 MBq. (We mean this source when we refer to as "the ^{252}Cf source" throughout this thesis.) The ^{252}Cf source was set at (0,0,33) and the plastic scintillator for a trigger was set by the source. Nuclear recoils due to neutrons from the source were detected and a drift-time (T) distribution of the hit points were obtained as shown in Figure 4.8. Because the detection volume was limited by the drift plane, we can see a edge due to the drift plane. The drift velocity was calculated to be 6.5cm/μs since the edge is at 4750 ns and a maximum drift length is 31cm which was a length from the drift plane to the GEM.
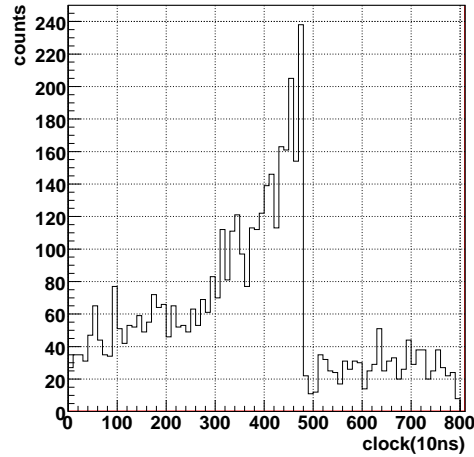
Figure 4.8: Drift-time distribution of nuclear recoils in a drift velocity measurement

4.2.2 Energy cariblation

We calibrated the μ-TPC with α-particles. First, we used the ^{10}B(n,α)^{7}Li reaction (Q = 2.7 MeV). The maximum energy of the α particle in this reaction is 1.5 MeV , and it runs approximately 1.6 cm in CF_4 gas at 152 torr. A glass plate with a size of 7.5×2.3 cm^2 and coated with a 0.6 μm-thick layer of ^{10}B was installed at the position (12.3, 8.0, 15.0) in the vessel as a part of the detector. We set the ^{252}Cf source, and then placed polyethylene blocks with a thickness of 5 cm surrounding the source, and thus the ^{10}B-plate was irradiated with thermal neutrons. In an analysis of this measurement, the events which were fully contained in an area of 5 cm≤X≤14 cm and 3 cm≤Y≤12 cm were selected. Typical tracks of α particles detected in this measurement are shown in Figure 4.9. Each mark indicates one digital hit, and different marks (colors) display different events. The gray region indicates the ^{10}B-plate in the figure. It was clearly seen that these tracks came from the ^{10}B-plate. We determined the energy scale using the spectrum edge around 1.5MeV. The measured length-to-energy correlation was compared with the one calculated by SRIM [77]. We fitted each track with
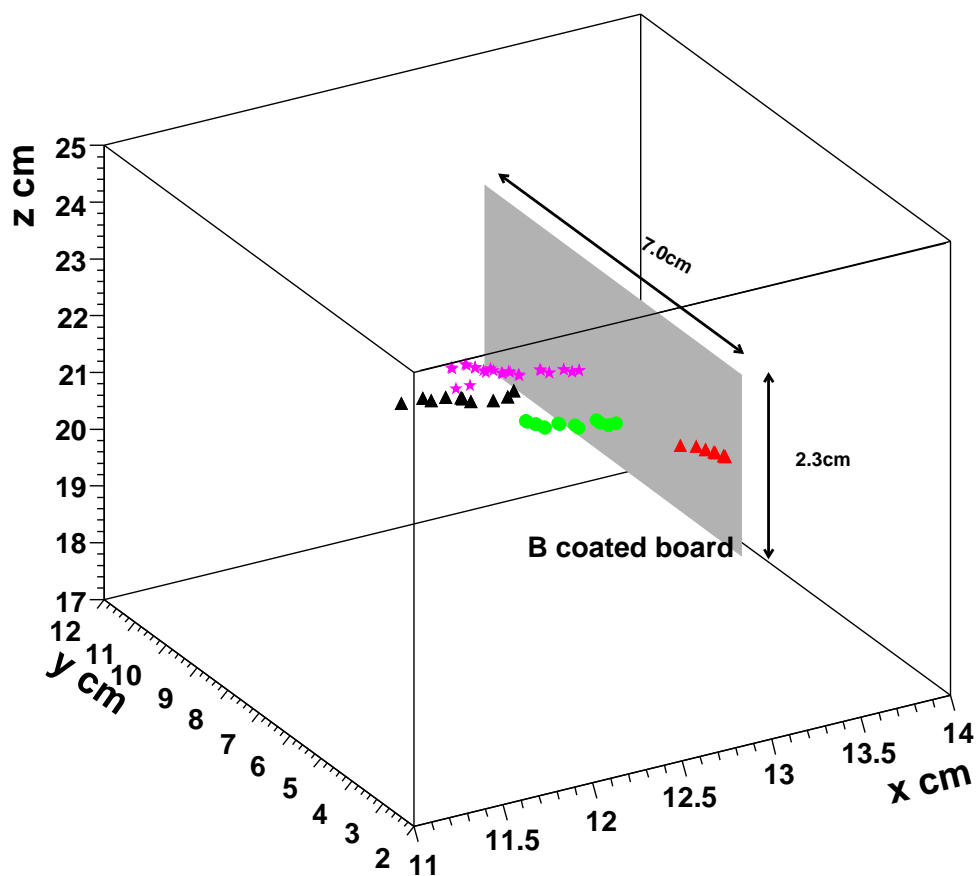
Figure 4.9: Typical tracks of α particles from the ^{10}B-plate. The ^{10}B-plate is set at the shaded area. Each mark indicates one digital hit and different marks (color) display different events.
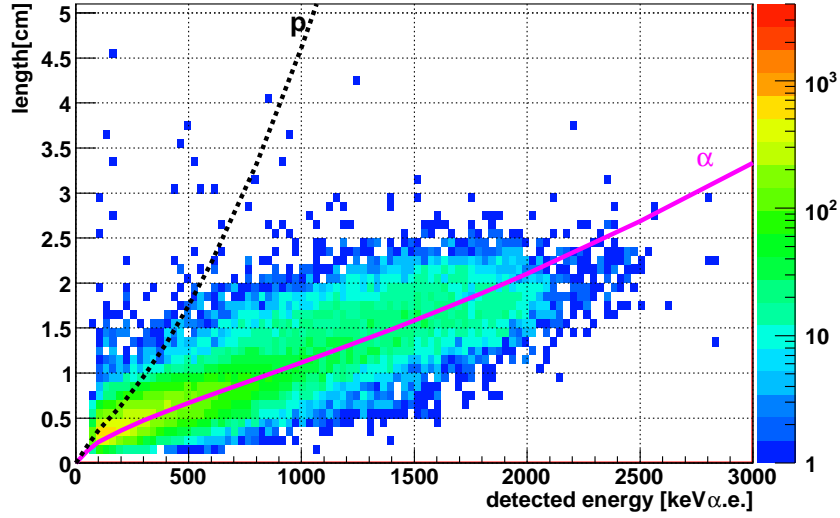
Figure 4.10: Correlation of the energy-length of the ^{10}B-run (color contour) and the calculated lines by SRIM. The dotted line (black) shows an energy-length correlation of the protons and the solid line (purple) shows one of the α particles.

a straight line and calculated the position on the nearest to each hit point, and then defined the track length as the distance between the both ends of the points on the fitted line. In Figure 4.10, the measured data are shown by the color contour, while the correlations of the protons and the α particles calculated by SRIM and were shown by dotted (black) and solid (purple) lines, respectively. The measured plots are consistent with those of the α-particle tracks down to 100 keV. The energy scale determined by these alpha-particles are used as keV α-particle equivalent (keVα.e.) because it is important to consider a nuclear quenching factor for low energy nuclear recoil detector, F_q, which is determined as

$$F_q = \frac{\text{energy used for ionization of target molecules}}{\text{total energy deposited in target}}. \tag{4.1}$$

Using this F_q, a number of ion-electron pairs produced by a recoil particle with an energy of E in a gas detector is calculated as $F_q \times \frac{E}{W}$, where W is W-value of the gas. Nuclear quenching factors for several gas detectors were summarized in [83]. The nuclear quenching factors of helium, carbon and fluorine ions in CF_4 gas were calculated by SRIM as shown in Figure 4.11. These values are used when the energy deposition of ions in a detector are calibrated by α-particle energy.

4.2.3 Position-dependence of the gas gains

We measured the position-dependence of the gas gains in order to apply the calibration by the ^{10}B-plate to the whole area. Then we used background α particles from ^{222}Rn progeny (See Appendix A) for these two measurements, where the higher energy data, above 1 MeV, of a dark matter run performed with the self-trigger mode were used. We divided the fiducial area into 4×5 regions, and made an energy spectrum of each region by applying a length-selection of L > 3 cm. The background spectrum of the reference region
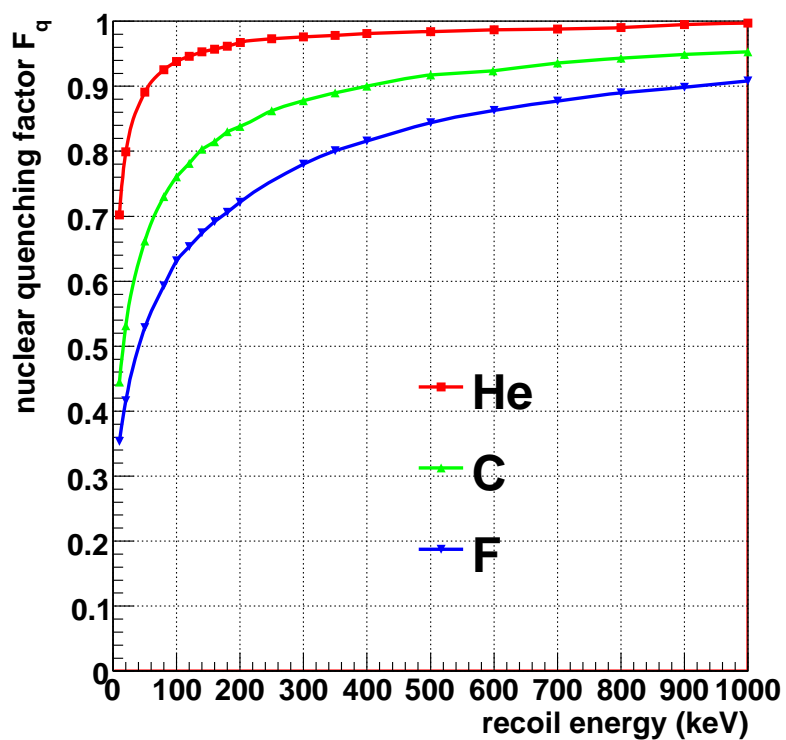
Figure 4.11: Nuclear quenching factor for helium (red line), carbon(green line) and fluorine (red line) in CF$_4$ gas. The number of ion-electron pairs produced by a particle with energy of E in gas is calculated as $F_{\mathrm{q}} \times \frac{E}{W}$, where W is the W-value of the gas.
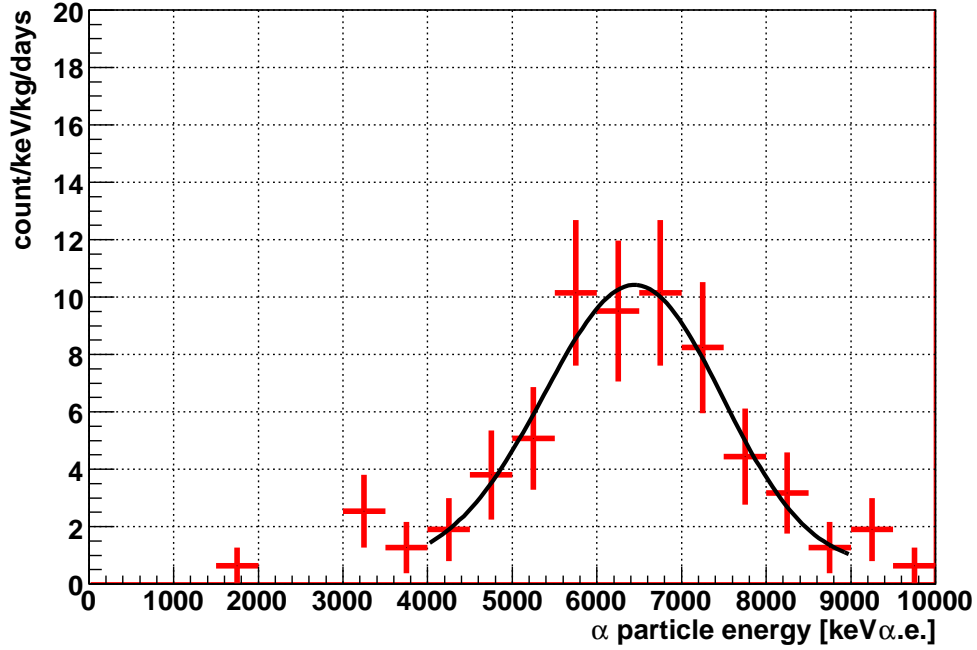
Figure 4.12: Spectrum of α particles due to the ^{222}Rn progeny in the reference region. The solid line is a best-fit function.

(7.5 cm$\leq$X$\leq$12.5 cm, 5 cm$\leq$Y$\leq$10 cm), which is the nearest region to the ^{10}B-plate is shown in Figure 4.12. We fitted the spectrum with a sum of three Gaussians that had peaks at 5.49 MeV, 6.00 MeV and 7.69 MeV, which are energies of α-particles emitted from ^{222}Rn progeny (See Figure A.2). We fixed the relative energy scales, relative energy resolutions and relative intensities of three peaks, while the absolute energy scale, the absolute energy resolution and the absolute intensity were treated as free parameters. The best-fit energy scale agreed with the one obtained with the ^{10}B-plate calibration with an accuracy of $\pm 3\%$ (RMS). We then fitted 19 spectra of other regions by the same method. We calculated the gas gains of these 19 regions relative to the ^{10}B-region using the best-fit energy scales. We show the relative gas gains of the whole area, or the gain map, in Figure 4.13. The gas gains were normalized by the averaged one. The maximum gas gain and the minimum one were 1.4 and 0.35, respectively. This in-uniformity of the gas gain was due to the plating process of the μ-PIC, and is expected to be improved in the next fabrication. We used this gain map to correct the gas gains in all analysis of the following measurements.

4.2.4 Energy resolution

We made an energy spectrum of the whole fiducial volume. We then fitted the corrected energy spectrum in the same way as we fitted the spectrum of each region. The measured spectrum and corrected spectrum are shown in Figure 4.14. The energy resolution was 45% (FWHM) around 6 MeV. This energy resolution was not a good value, which is probably due to the local position-dependence of the gas gains within the regions and the position-dependence along the Z-axis.
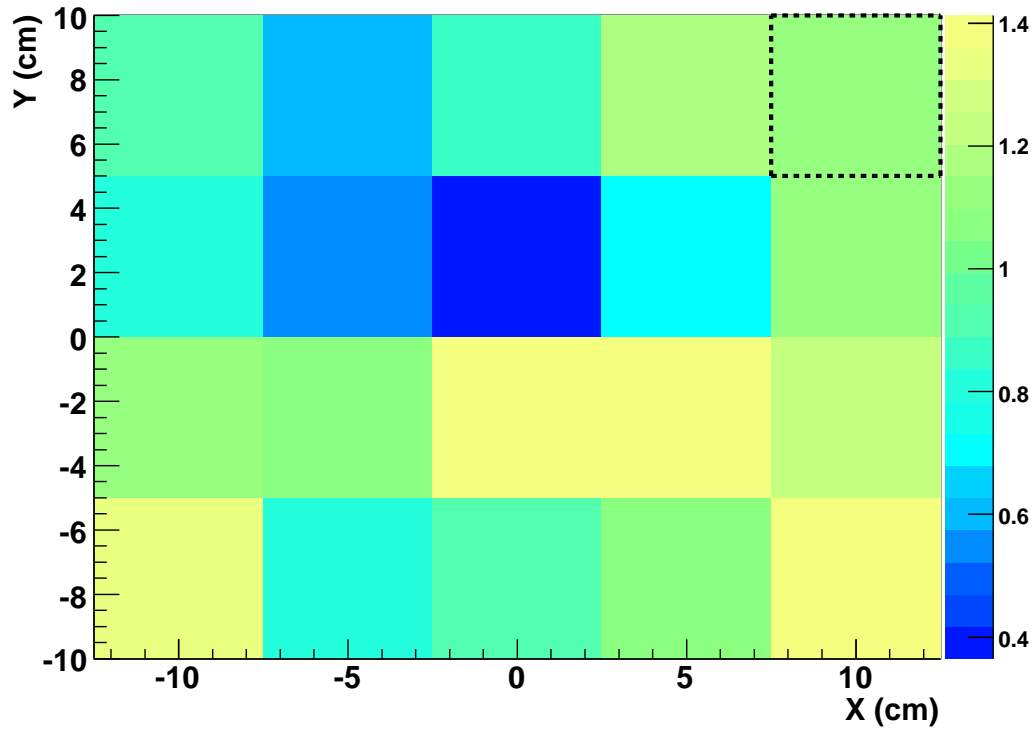
Figure 4.13: Measured relative gain map of the μ-TPC. The area enclosed with dotted lines is the reference region. The gas gains were normalized by averaged value.
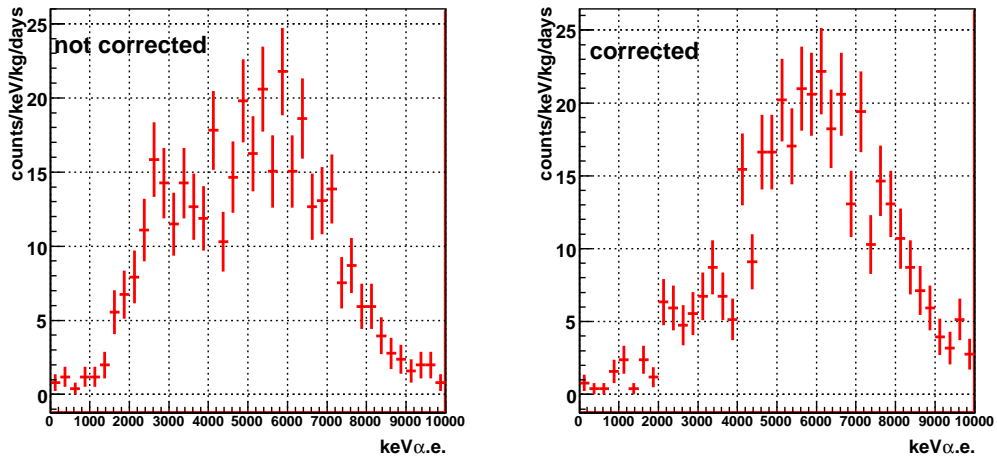
Figure 4.14: Measured spectrum of α particles due to the ^{222}Rn progeny from whole fiducial volume before (left) and after (right) the position dependent gain correction.
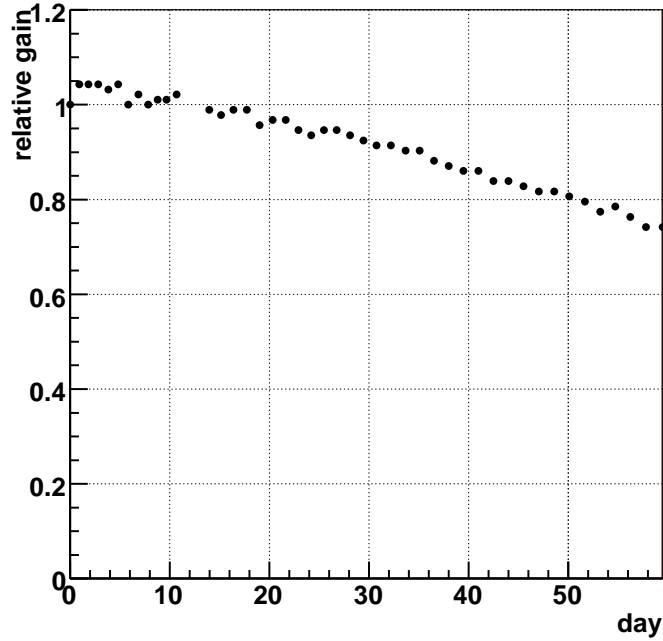
Figure 4.15: Time-dependence of the gas gain. The origin of the time axis is when we filled the vessel with a CF_4 gas and gas gains are normalized by the initial one.

The energy resolution around 100 keVα.e. was estimated as follows. There were fluctuations due to an electrical noise σ_{noise} equal to about 55 keVα.e.(FWHM) against a gas gain of 2000, while that of position dependence σ_{uni} was less than 45% (FWHM) as measured and that of statistical dependence σ_{sta} was 5.5% (FWHM) at 100keVα.e.. Thus the total energy resolution was estimated to be about 70% at 100 keVα.e. with a gas gain of 2000.

4.2.5   Time-dependence of the gas gains

Also we have to monitor the time-dependence of the gas gains in order to calibrate the energy properly during a long-term measurement. The time-dependence of the gas gain was monitores by the energy scale obtained by the procedure described in Section 4.2.2. The measured time-dependence of the gas gain is shown in Figure 4.15, where the origin of the time axis was when we filled the vessel with CF_4 gas. A gradual 15% decrease of the gas gain was observed in one month. The decrease was so slow that we could correct a calibration parameter with this gain monitor. However we needed a certain gas gain to maintain sufficient performances, so we refilled the vessel with new CF_4 gas at least every two months.
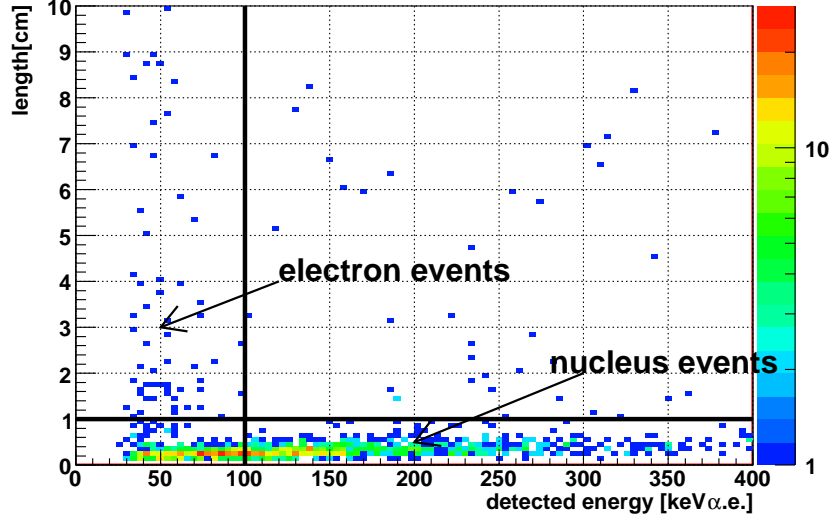
Figure 4.16: Correlation of the length-energy of the ^{252}Cf run. The nuclear-selection region is indicated by the vertical thick line (E>100 keVα.e.) and the horizontal thick line (L<1 cm).

4.3 Gamma-ray rejection power

Gamma rays are known to be one of the most dominant background sources for direct dark matter search experiments. Many technologies have been developed to subtract them statistically [47, 48, 69, 70, 71], or reject them by event-by-event methods [56, 55, 59, 61, 64, 65]. Obviously the latter method is more reliable for experiments with a poor statistics of real events. In the NEWAGE-0.3a detector the length-to-energy correlation is used to discriminate the electron tracks from the nuclear tracks by an event-by-event method. Recoil nuclei are known to deposit much more energy per unit length than electrons. We measured the responses of the μ-TPC to the gamma rays to measure the rejection power.

We set the ^{252}Cf source at a position of (0,0,40.5) so as to irradiate μ-TPC with fast neutrons and gamma rays. We then replaced the source with a ^{137}Cs gamma-ray source with an intensity of 0.9 MBq. Both measurements were performed in the self-trigger mode with the full-fiducial volume. We determined the nuclear recoil region of the "nuclear selection", where few gamma-ray events were expected. Figure 4.16 shows a length-to-energy plot of a ^{252}Cf run. In the ^{252}Cf run, most events are seen in the nuclear recoil region along the horizontal axis. We determined the nuclear selection as requiring both L<1 cm and E>100 keVα.e. The length limit was to reject gamma rays, and the energy threshold was to keep certain angular resolutions. (See Section 4.4.3.) The detection efficiencies for the nuclear tracks are discussed in Section 4.4.1. Figure 4.17 shows a length-to-energy plot of the ^{137}Cs run. Almost all events were outside of the nuclear region, which indicated a good gamma-ray rejection power.

We calculated the rejection factor of the electron tracks by a comparison between the ^{137}Cs run and a data simulated by Geant4. We defined the rejection factor of the electron tracks as the probability that we mis-identify an electron event as a nuclear event. Figure 4.18 shows the energy spectra of the nuclear track region of the ^{137}Cs run (square and red line histogram) and the background run (triangle and blue line histogram). We
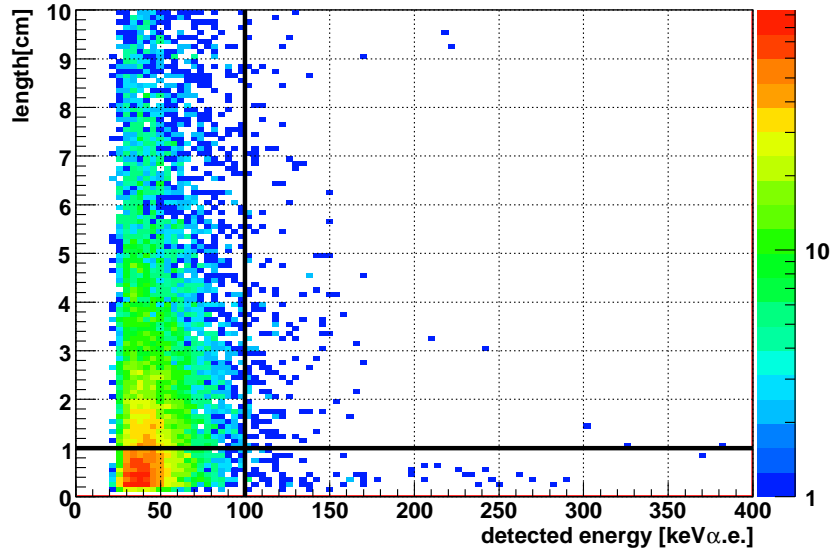
Figure 4.17: Correlation of the length-energy of the ^{137}Cs run. The thick lines shows the selection described in Figure 4.16. Almost all events are outside of the nuclear region.
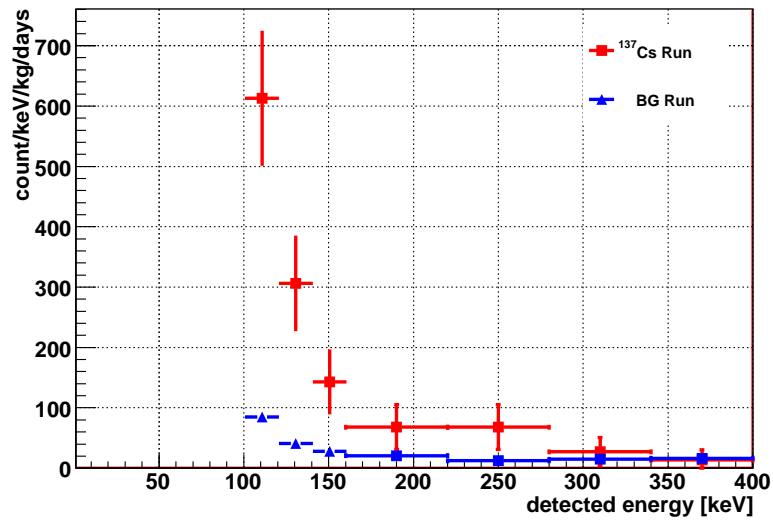
Figure 4.18: Spectra of the ^{137}Cs run (square red) and the background run (triangle blue) in the nuclear recoil region.
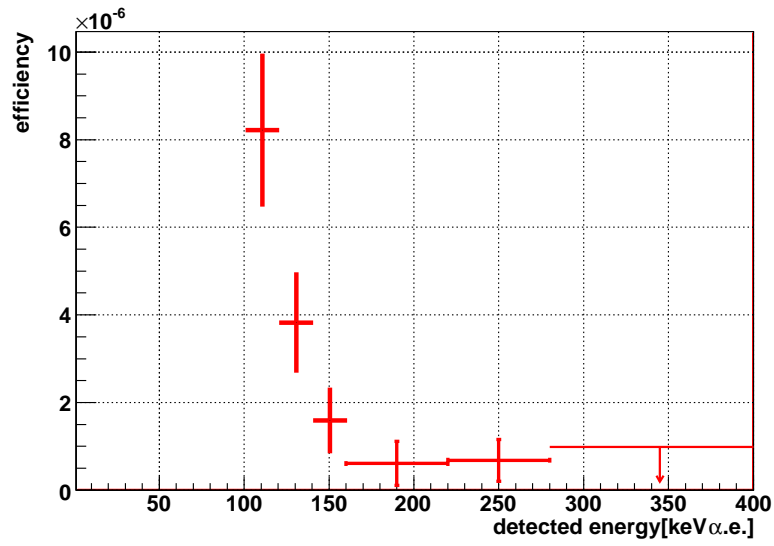
Figure 4.19: Efficiency of the electron track detection, or the gamma-ray rejection power, of μ-TPC in the nuclear recoil region.

subtracted the background spectrum from the ^{137}Cs run spectrum. We then derived the rejection factor of the electron track by dividing the measured subtracted spectrum by the simulated spectrum of the initial energy of the recoil electrons. The result is shown in Figure 4.19. The measured rejection factor of the electron tracks is $(8.1\pm1.9)\times10^{-6}$ at 100 keVα.e., and less than 1×10^{-6} at an energy region higher than 200 keVα.e.
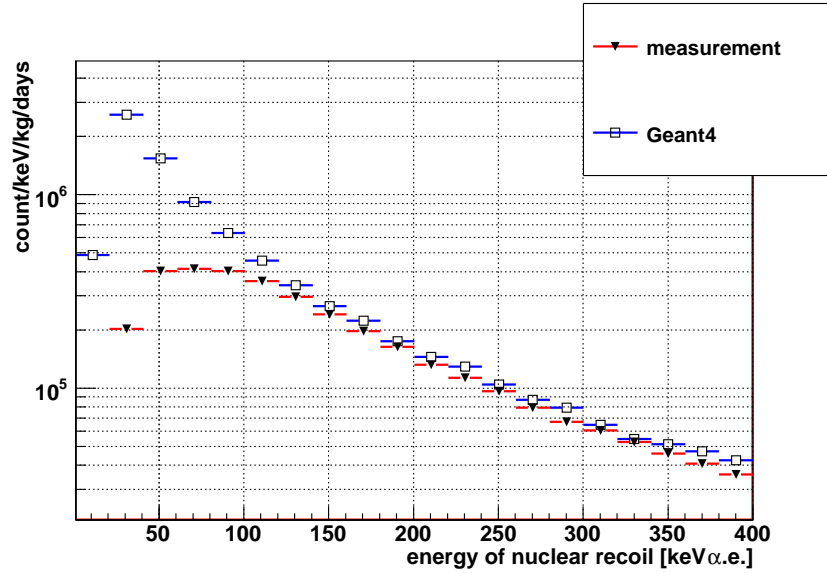
Figure 4.20: Measured (triangle red) and simulated (square blue) spectra of the nuclear recoil scattered by fast neutrons from the ^{252}Cf source.
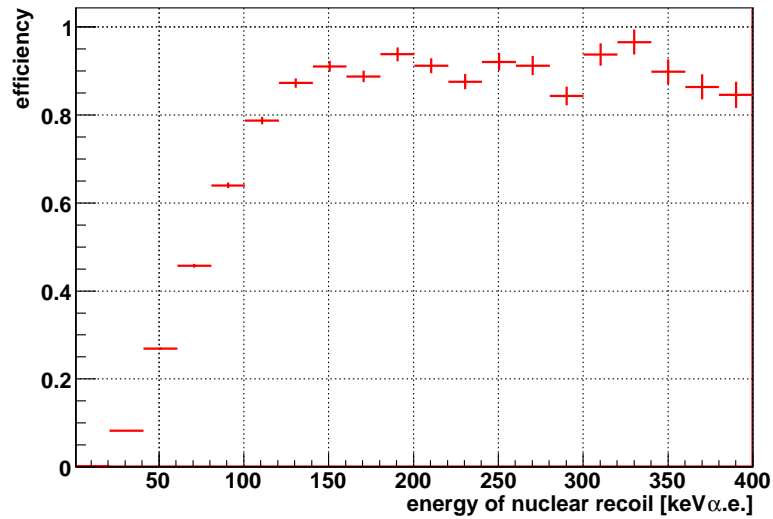
Figure 4.21: Absolute detection efficiency of the μ-TPC for nuclear recoil.

4.4   Response to nuclear recoils

4.4.1   Absolute detection efficiency

It is very important to precisely investigate the responses of the μ-TPC to nuclear recoils for a dark matter search. We measured the absolute detection efficiency by comparing the
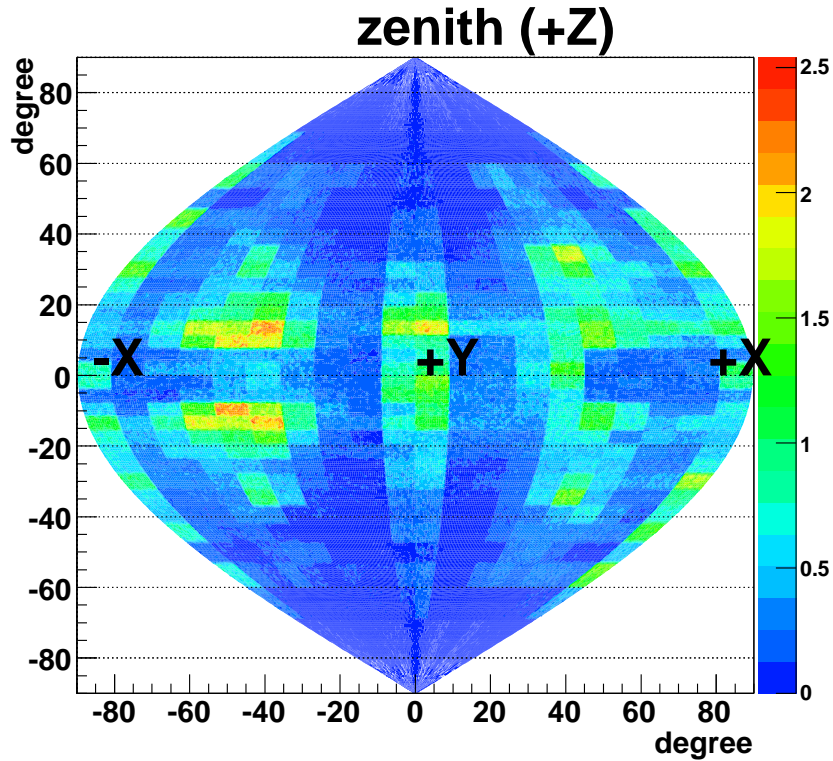
Figure 4.22: Relative directional-dependent efficiency (100-400 keVα.e.), which is the detection efficiency of nuclear recoils depending on the directions of nuclear recoils. The vertical axis is the elevation angle and the horizontal axis is the azimuth angle.

measured spectrum of nuclear recoils scattered by fast neutrons from the ^{252}Cf source with a simulated spectrum.

A Geant4 simulation indicated that the irradiations from positions of (25,0,15), (-25,0,15), (0,25,15), (0,-25,15), (0,0,40.5) and (0,0,-9.5) provide an isotropic distribution of the nuclear recoil directions. We irradiated the detector with fast neutrons from the ^{252}Cf source placed at one of the six positions described above, and took data in the self-trigger mode. We repeated this measurement for the six positions. We applied the fiducial- and nuclear-selections and combined six spectra. The combined spectrum and the simulated one are shown in Figure 4.20. The simulated spectrum was normalized taking account of the live time of the measurements, the intensity of the source and the quenching factor of carbon and fluorine in Figure 4.11. Then, the absolute detection efficiency was obtained by dividing the measured spectrum by the simulated one. As shown in Figure 4.21, the detection efficiency was 80% at 100 keVα.e. This decrease was reasonable because we apply the nhit selection (NHIT>2) and the two-dimensional sampling pitch of the μ-PIC (400 μm) and the sampling clock (100 MHz) was not fine enough compared to the track length (ex. 1.1 mm for an 100 keVα.e. for a fluorine nucleus in 152 torr CF$_4$).

4.4.2 Directional-dependent efficiency

For the same reason as the absolute efficiency decrease, there also exists an in-uniformity of the detection efficiency of the nuclear recoil depending on the direction of the nuclear recoil (*directional-dependent efficiency*). For a directional dark matter search, we need a *directional-dependent efficiency* map of the nuclear recoil. We made a map by comparing the measured distribution of directions of the nuclear recoil with the simulated one. We used the same isotropic scattering data described in Section 4.4.1. The direction of each nuclear recoil was determined by the best-fit vector, which was derived from a fitted line of measured nuclear track points. In the fitting process, we fixed the sign of the X component of the vector to be positive, because we did not measure the track sense (head-tail discrimination) in this measurement. We made a distribution of the direction of the nuclear track with the energy range of 100-400 keVα.e. (*measured direction distribution*). We also made a distribution of the direction of simulated nuclear recoils under the same condition, which was isotropic, as we had expected (*simulated direction distribution*). The relative *directional-dependent efficiency* was derived by dividing the *measured direction distribution* by the *simulated direction* one. We show the relative *directional-dependent efficiency* in Figure 4.22. The efficiency is shown in the celestial chart, where the vertical axis is the elevation angle, the horizontal axis is the azimuth angle, and the color contour shows the relative *directional-dependent efficiency* normalized by the mean value. Our detector had better efficiencies for tracks with moderate elevations (around 45° from the horizon) than for those close to the vertical (elevation=90°). This is mainly caused by the readout system and we are trying to decrease the direction-dependence by improving the position encoding algorithm.

4.4.3 Angular resolution

The angular resolution of the tracking is one of the most important parameters of a direction-sensitive dark matter detector. We defined the tracking angular resolution as the root mean square (RMS) of the angles between the real tracks and the measured ones. We measured the angular resolution by comparing the distribution of the measured recoil angles of the nuclear tracks with that of the simulated ones. Figure 4.23 shows simulated $\left|\cos\theta\right|$ distributions, where θ is the angle between the direction of an incident neutron and a nuclear track. Each $\left|\cos\theta\right|$ distribution was a combined one of the results of the simulations in which the ^{252}Cf source was set at (25,0,15), (0,-25,15) and (0,0,40.5), The tracking angular resolutions of 0°, 22.5°, 45.0°, 67.5° and 90.0° were taken into account using two-dimensional Gaussians. The relative *directional-dependent efficiency* shown in Figure 4.22 was also taken into account. The shape of the distribution of the $\left|\cos\theta\right|$ apparently depends on the angular resolution of the tracking. We thus can measure the angular resolution by comparing the measured distribution with the simulated distributions.

We set the ^{252}Cf source at the positions of (25,0,15), (0,-25,15) and (0,0,40.5), and measured with the external-trigger mode. We used this mode to detect the absolute position of a nuclear recoil and thus the incoming direction of an incident neutron was precisely measured. We set the sign of the X component of the direction of the nuclear recoil to be positive by the same reason as in the previous measurement. The incident neutron vector was calculated from the source position and the hit point nearest to the source position, while the nuclear recoil track vector was measured by the μ-TPC. We then calculated the absolute value of the cosine of a recoil angle between these two vectors.

One of the measured distributions is shown by a histogram with errors (red) in Figure 4.24, where the energy range was 100-400 keVα.e. We compared the measured histogram with simulated histograms with various angular resolutions in the range from 0° to 90°. The simulated one with an angular resolution of 46° fitted with the least value of
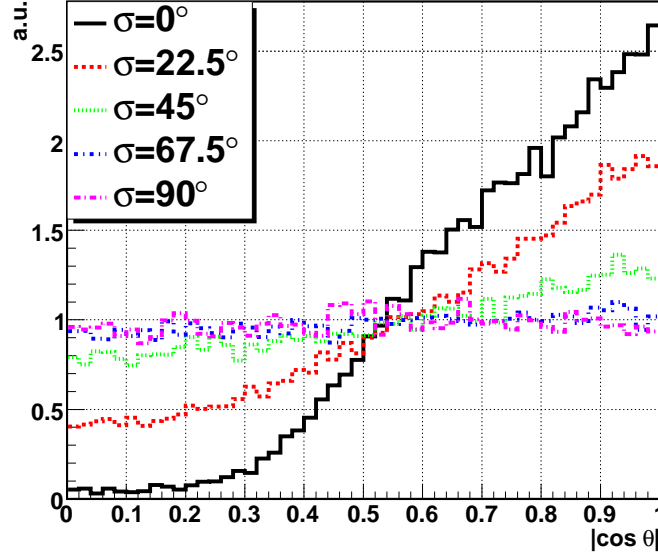
Figure 4.23: Simulated distributions of the absolute value of the cosine of the recoil angle of the nuclear tracks (100-400 keVα.e.) assuming some angular resolutions of the tracking.

χ^2, where χ^2/d.o.f was 1.829/9. This best-fit simulated histogram is shown by the solid histogram (black) in Figure 4.24. The probabilities derived for the χ^2 tests are shown in Figure 4.25 as a function of the angular resolution. Thus, the angular resolution of the tracking was known to be 46±3° in the energy range of 100- 400 keVα.e., where the error was the 68% confidence level. We also derived the angular resolutions in the energy ranges of 100-200 keVα.e., 200-300 keVα.e., 300-400 keVα.e. and 400- 800 keVα.e. by the same method. The result is shown in Figure 4.26. The angular resolution was better at higher energy due to a longer track This trend indicates that better resolution is expected in a lower pressure gas. We will operate the μ-TPC at a lower pressure in the near future for better angular resolutions.
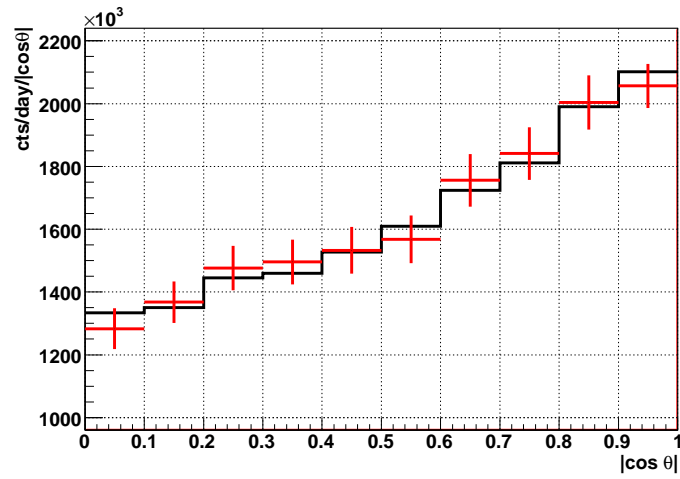
Figure 4.24: Measured (red histogram with error bars) and the best-fit simulated (black solid histogram) distributions of $\left|\cos\theta\right|$.
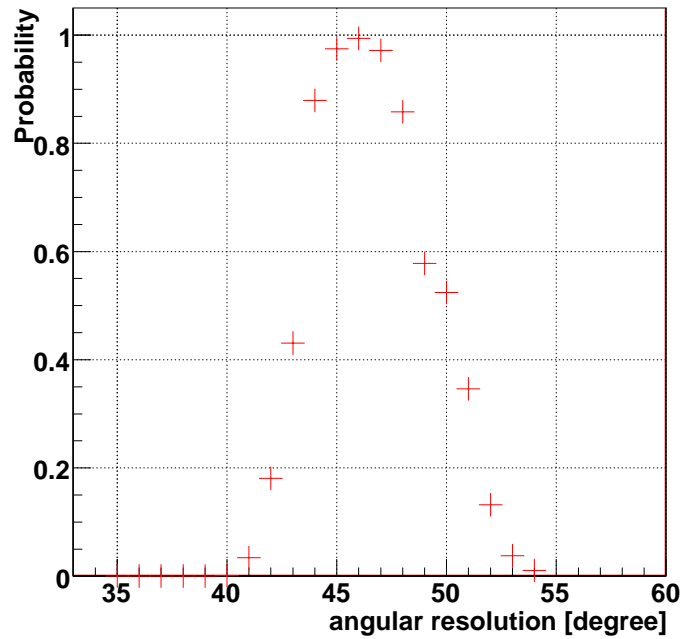
Figure 4.25: Probabilities derived by the χ^2 as a function of angular resolutions. We fitted measured $\left|\cos\theta\right|$ distributions with simulated ones.
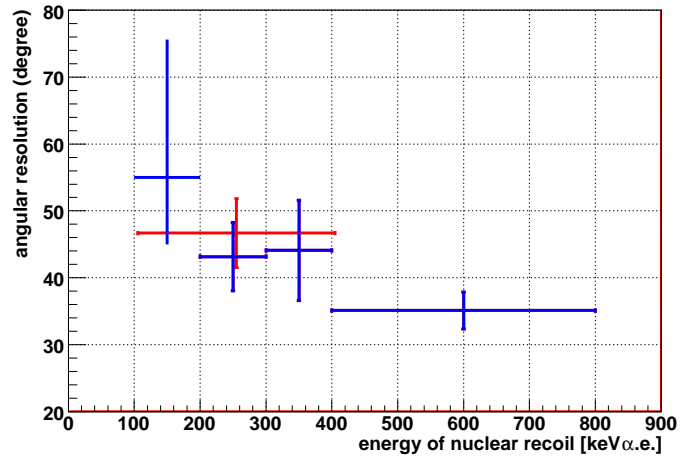
Figure 4.26: Angular resolutions of the nuclear tracking as a function of the recoil energy. The errors bars indicate the 68% errors. The blue points show those with each energy and the red one shows that with the energy in range of 100-400 keVα.e..

4.5   Summary of detector performance

We summarized the performances of the NEWAGE-0.3a detector in Table 4.3.

parameter	values	section
energy resolution	45% (FWHM) at 6 MeVα.e.	(4.2.4)
	70% (FWHM) at 100 keVα.e.	(4.2.4)
γ-ray detection efficiency	8.1×10^{-6} at 100keVα.e.	(4.3)
energy threshold for nuclear recoil	100 keVα.e.	(4.3)
Nuclear detection efficiency	80% at 100keVα.e.	(4.4.1)
Nuclear angular resolution	55°(RMS) at 100keVα.e.	(4.4.3)

Table 4.3: Performances of the NEWAGE-0.3a detector.

Chapter 5

Pilot runs and background studies in Kamioka mine

We performed pilot runs for the dark-matter search with the NEWAGE-0.3a detector in a surface laboratory and an underground laboratory in Kamioka mine. Purposes of these pilot runs are to demonstrate a long term stability of the detector and to understand background events due to neutrons, γ-rays and α-particles in an underground laboratory. In this chapter we will briefly introduce a surface run result, which was reported in [85], then report the pilot runs in the underground laboratory. We then discuss remaining background events measured in these pilot runs.

5.1   Dark matter search in a surface laboratory

A dark matter search measurement was performed in a surface laboratory at Kyoto University (Lat. $35°2'$N, Long. $135°47'$ E, third floor in a five-story building). The measurement was performed from November 1st, 2006 to November 27th, 2006. The total live time was 16.71 days and the exposure was 0.151 kg·days. Figure 5.1 shows the obtained spectrum in the energy range of 100-400 keV. The spectrum can be explained by a typical neutron flux in a surface laboratory of $O(1 \times 10^{-2} \mathrm{ncm}^{-2}\mathrm{s}^{-1})$. We derived the limits of the WIMP-proton SD cross section only from the spectrum(conventional method) and by a direction-sensitive method as shown in Figure 5.2. This limit was the first limit derived with a gasous direction-sensitive detector.
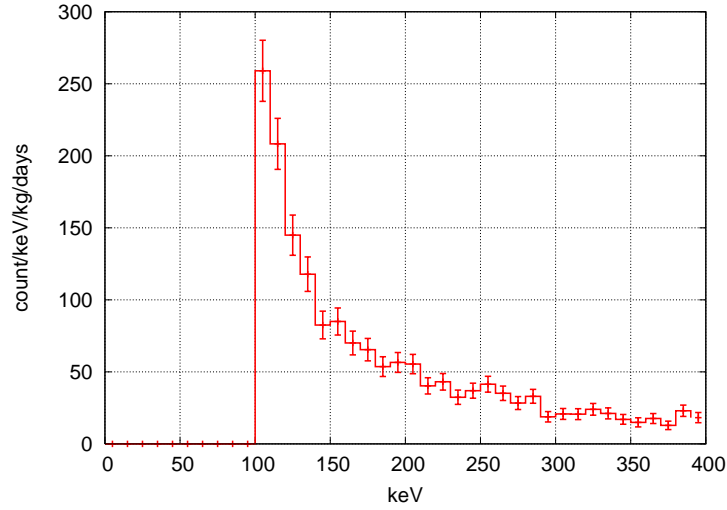
Figure 5.1: Measured energy spectrum in the surface run. The detection efficiency was taken into account.
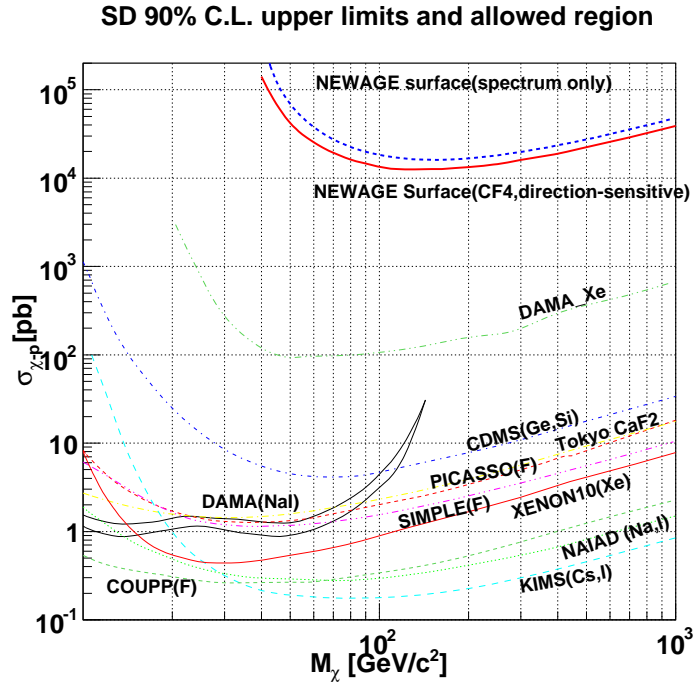
Figure 5.2: Limits of SD cross section as a function of M_χ. NEWAGE surface run experiment results (blue conventional method red direction-sensitive method). Allowed region(DAMA(NaI)[45]) and limits of other experiments (DAMA(Xe)[60], CDMS[56], Tokyo[49], PICASSO[71], SIMPLE[70], NAIAD[47], KIMS[48], XENON10[64],COUPP[69]) are shown for comparison.

5.2 Pilot runs in an underground laboratory
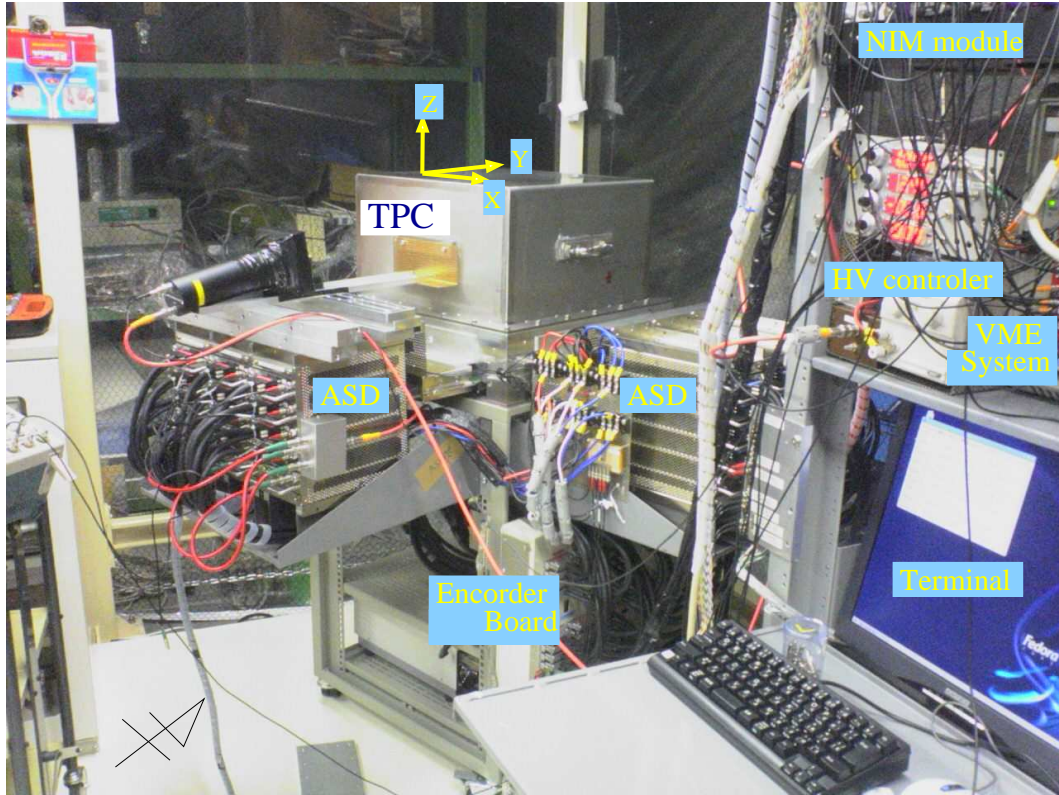
Figure 5.3: Photograph of the NEWAGE-0.3a detector placed in Kamioka Observatory.

Pilot runs with the NEWAGE-0.3a detector were performed in an underground laboratory in Kamioka mine. The NEWAGE-0.3a detector was placed in Laboratory B, Kamioka Observatory located at 2700m water equivalent (w.e.) underground (36°25'N, 137°18'E). Since the aims of the NEWAGE-0.3a detector were to demonstrate a long-term operation and to study the background, we did not set any radiation shield. The detector was set so that the μ-PIC plane was placed horizontally and the X-axis is aligned to the direction of S87°E as shown in Figure 5.3. (For detector coordinates, see Figure 4.3).

The run properties are summarized in Table 5.1. Run IDs were reassigned when we

run ID	date	live time [day]	effective mass [g]	exposure[kg days]
RUN-I-1	Dec.7th -Dec.18th,2007	10.05	11.48	0.115
RUN-I-2	Dec.18th, 2007 -Mar.4th, 2008	66.04	11.48	0.758
RUN-I-3	Mar.6th -Apr.6th, 2008	16.15	11.48	0.185
RUN-I-4	Apr.9th -Jun.10th, 2008	57.10	11.48	0.686
	Kamioka RUN-I total exposure			1.744
RUN-II-1	Jun.12th -Jul.24th, 2008	21.46	11.48	0.246
RUN-II-2	Jul.25th -Sep.9th, 2008	30.99	11.48	0.356
	Kamioka RUN-II total exposure			0.602

Table 5.1: Properties of the pilot runs in Kamioka mine.

refilled the chamber gas. The time dependencies of the drift velocity and the detection efficiency at 100 keVα.e. are measured as shown in Figure 5.4, and Figure 5.5, by the methods described in Section 4.2.1 and Section 4.2.5, respectively. The red points in figures show measured values and black error bars show interpolated value used in the analysis. There were decrease due to the gas impurity and recoveries due to the gas refills in the both figures. We also monitored the gas gain during the pilot run using the peak position around 6 MeV due to radons with the method described in Section 4.2.4, as shown in Figure 5.6. There were decreases of the gas gain due to the gas impurity and recoveries due to the gas refills. The peak count rate around 6 MeV, R_{peak} , which is a useful parameter to study the radon behaviors in the gas volume for background study later (Section 5.4.1), was also measured as shown in Figure 5.7. This variation seemed to be due to ^{222}Rn decay as described in Section 5.4.1.

All the data of these pilot runs were analyzed with the nuclear selection cut and the fiducial volume cut with the method as described in Section 4.1.2. Since the detection efficiency and gas gain decreased, we corrected the calibration factor and detection efficiency with monitored parameters. Details of each run are described in the following sections.
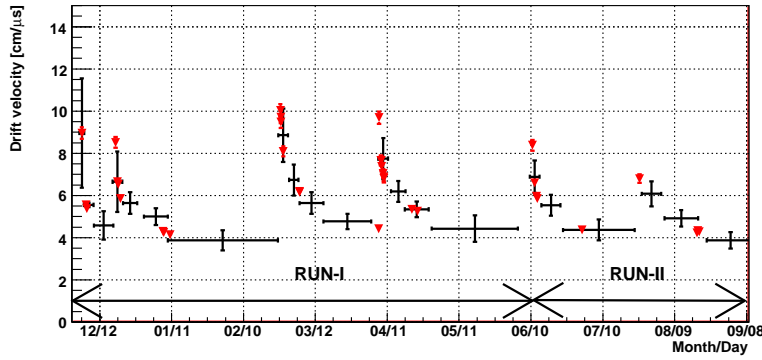
Figure 5.4: Drift velocities during the pilot runs in Kamioka mine (Kamioka RUN-I and RUN-II). Red points show measured values. Black error bars show interpolated values for the analysis.
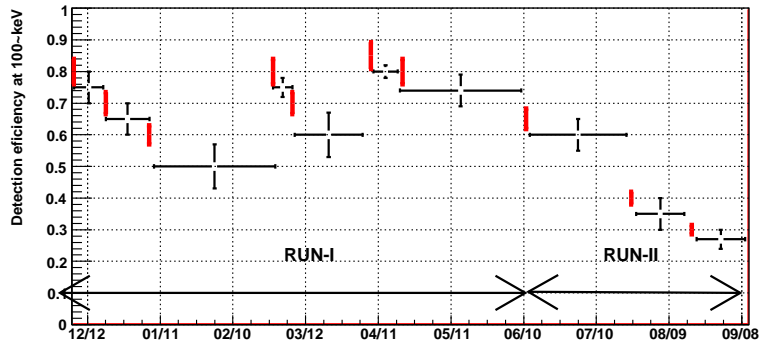
Figure 5.5: Nuclear detection efficiencies at 100 keVα.e. during the pilot runs in Kamioka mine (Kamioka RUN-I and RUN-II). Red points show measured values. Black error bars show interpolated values for the analysis.
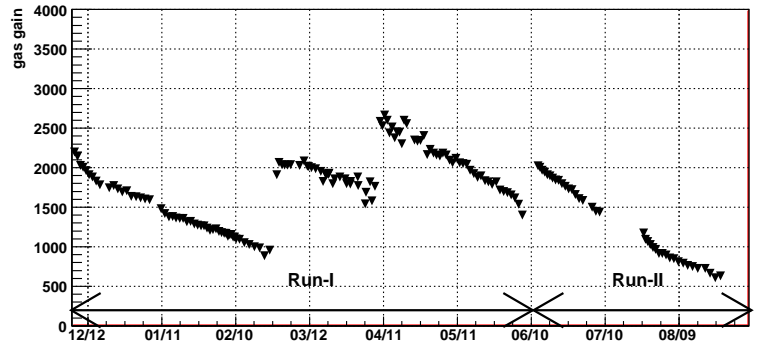
Figure 5.6: Monitored gas gain in the pilot runs (Kamioka RUN-I and RUN-II). Decrease of the gas gain was due to gas impurity. Recoveries of the gas gain were due to the gas refill.
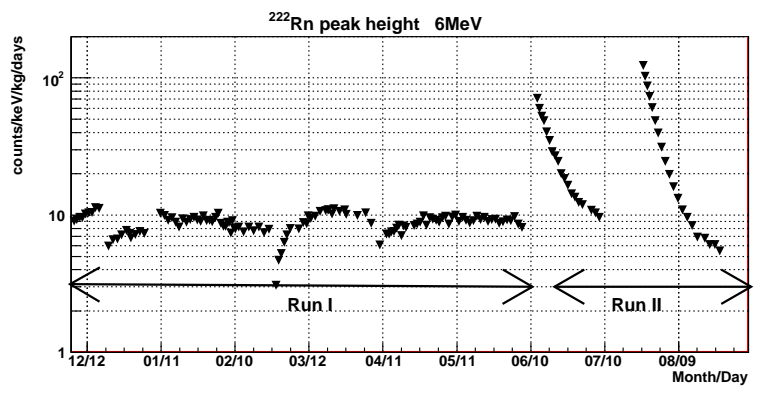
Figure 5.7: Monitored a peak count rate around 6 MeV due to ^{222}Rn progeny in pilot runs (Kamioka RUN-I and RUN-II). The variation of peak count rate due to ^{222}Rn is discussed in Section 5.4.1

5.2.1 Kamioka RUN-I ~ first underground run

We started the first underground measurement (Kamioka RUN-I) on December 7th, 2007. Until June, 2008, we eventually achieved a total exposure of 1.74 kg·days. Obtained spectrum is shown in Figure 5.10. Measured event rate between 100 keVα.e. and 400 keVα.e. region was about 40 % of that measured in the surface run. The background sources are discussed from Section 5.3. We then plotted the directions of nuclear recoil tracks with an energy range of between 100 keVα.e. and 400 keVα.e. with the black points in Figure 5.9(top). We also plotted the directions of the solar motion, or the Cygnus from which WIMP-wind is expected at each event time with purple circle marks. We calculated θ, the angle between the recoil direction and the WIMP-wind direction for each event, and drew the $|\cos\theta|$ distribution shown in Figure 5.9(bottom).
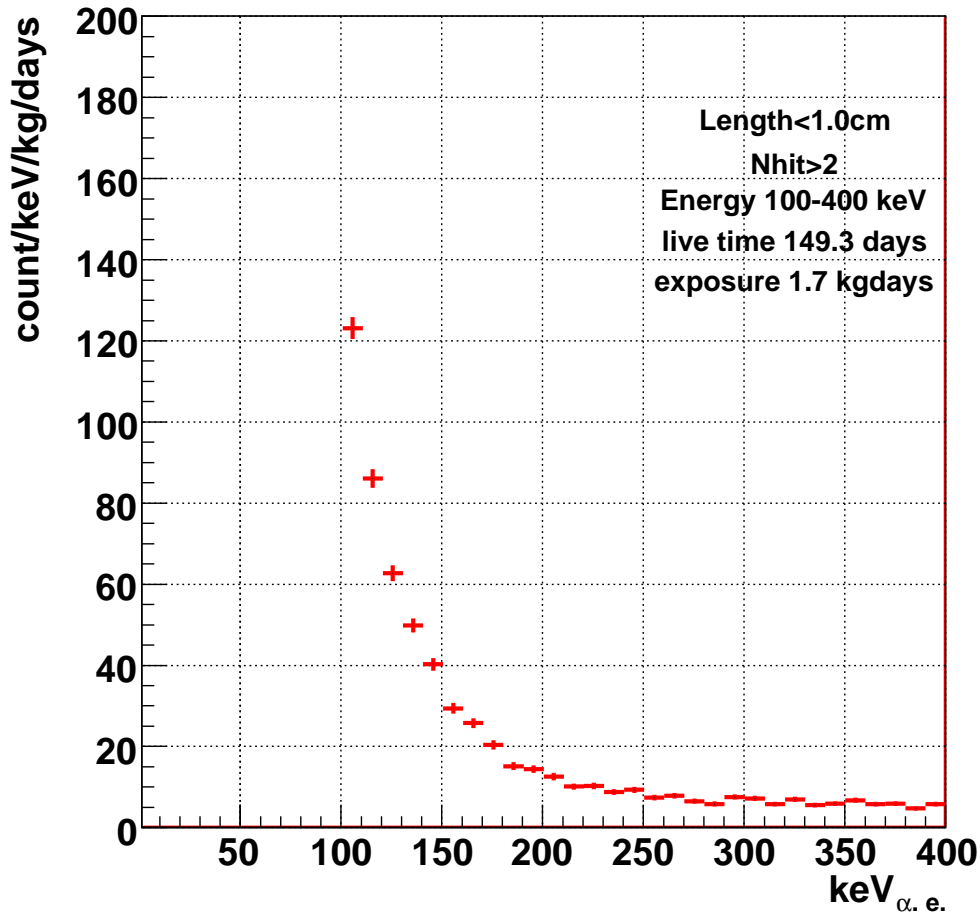
Figure 5.8: Obtained spectrum in Kamioka RUN-I.
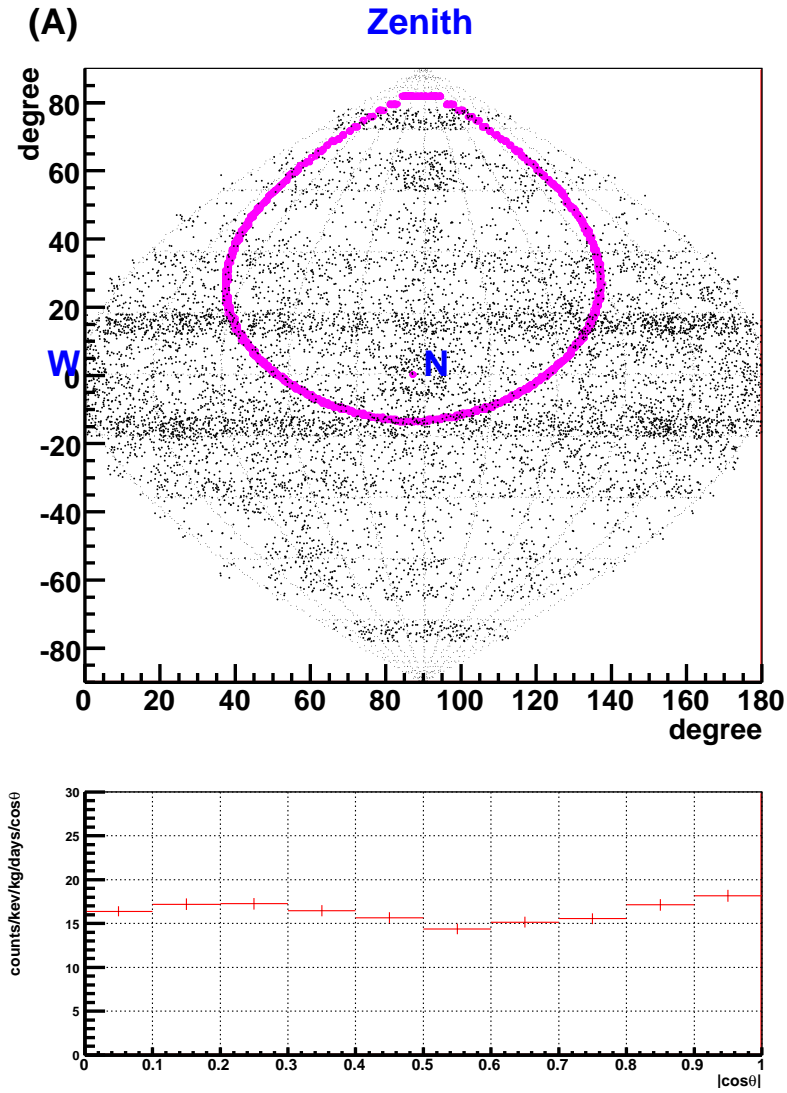
Figure 5.9: Obtained nuclear direction plots of events (top) and $|\cos\theta|$ distribution(bottom) in Kamioka RUN-I. An inuniformity in the event direction plots was due to the *directional-dependent efficiency*.

5.2.2   Kamioka RUN-II ~ radon-rich run

We then the performed a radon rich run (Kamioka RUN-II) in order to study contributions of radon to the dark matter search energy region from June 12th, 2008. Since α-particles from ^{222}Rn progeny are one of the most probable candidates of remaining background origins, it was important to study their behaviors(See Section 5.4.1 and Appendix A). We intentionally mixed radon gas in the chamber gas by using the vacuum tube exposed to the radon-rich atmosphere in the underground laboratory. Measured peak around 6 MeV due to α-particles from radon progeny at the beginning of Kamioka RUN-II was ten times larger than that of the Kamoika RUN-I as expected as shown in Figure 5.7. Time-variations of this peak and contribution to the dark matter regions is discussed in Section 5.4.

Obtained spectrum in the energy range of 100-400 keVα.e., the direction map and the $|\cos\theta|$ distribution drawn by the same manner in the previous section are shown in Figure 5.10, and Figure 5.11(top and bottom), respectively. The count rate at 100 keVα.e. was 1.5 times larger than that of Kamioka RUN-I.
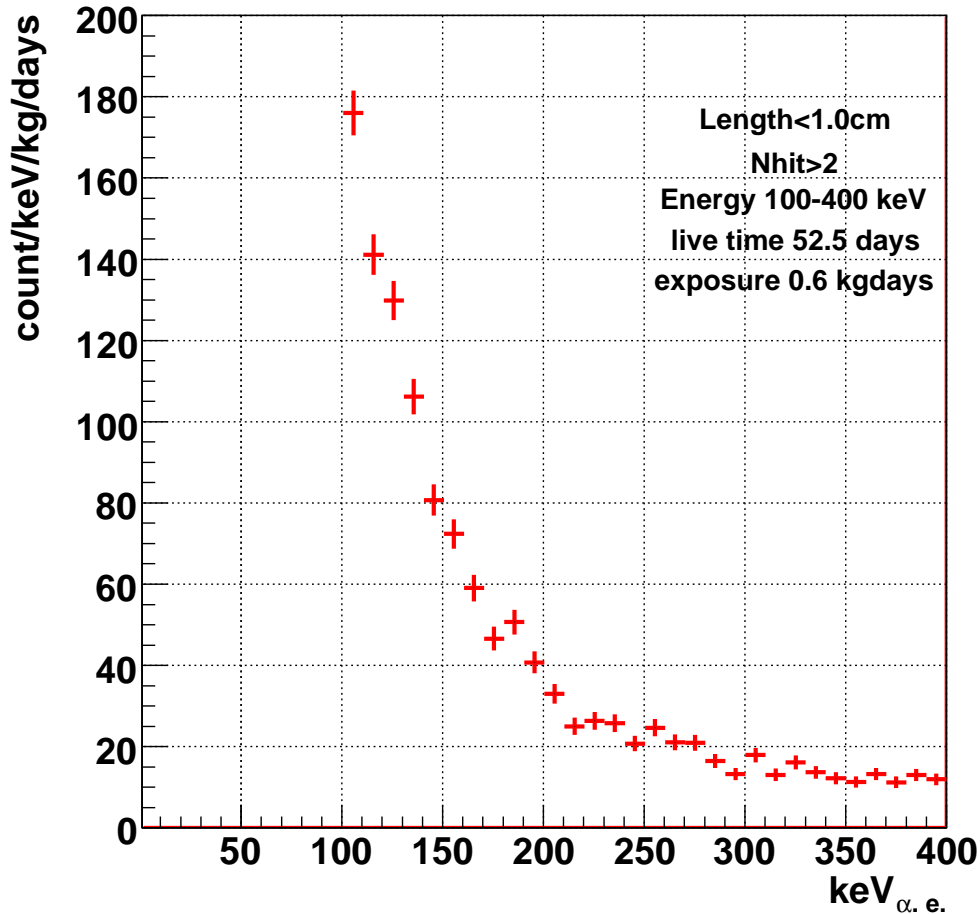
Figure 5.10: Obtained spectrum in Kamioka RUN-II

(A)

(B)
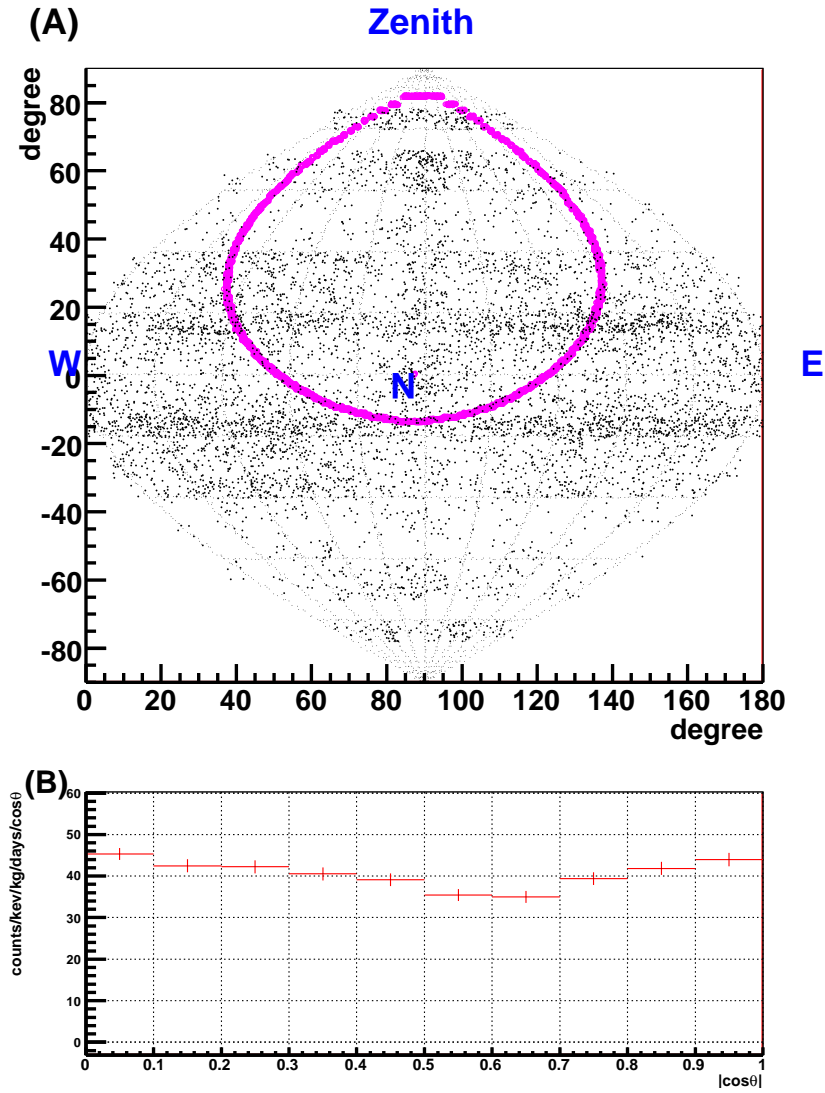
Figure 5.11: Obtained nuclear direction plot of events (top) and $|\cos\theta|$ distribution(bottom) in Kamioka RUN-II.An inuniformity in the event direction plots was due to the *directional-dependent efficiency.*

5.2.3 Summary of the pilot runs

The first underground run (Kamioka RUN-I in Figure 5.8) was performed at the same condition as the surface run in a low background environment where neutron flux is approximately three orders of magnitude less than that in the surface laboratory (see Section5.3). Measured count rate in Kamioka RUN-I was 40% of that of the surface run. This result explained that about half of the background sources in the surface run were ambient neutrons and the measured spectrum in Kamioka RUN-I was caused by other sources. A flat $|\cos\theta|$ distribution (Figure 5.9 (bottom)) showed that unknown remaining backgrounds, not the WIMP signals, should have dominated the measured events. The result of the radon-rich run (Kamioka RUN-II) implied the possibility of the contributions of the radon progeny. In the following sections we will precisely discuss the candidates of this unknown background.

5.3   Background from outside the vacuum chamber

We discuss the remaining background measured in Kamioka RUN-I and RUN-II. We discuss background originating outside the vacuum chamber and that originating inside the vacuum chamber in this section and the next section, respectively.

In this section, we start with the cosmic-ray muon which is the most common background sources in rare event searches. Then we discuss on the major two background sources in most of dark matter search experiments: γ-rays and neutrons. β-rays and α-particles from the outside can be neglected because they are stopped by the vacuum chamber. Therefore we estimated the contributions of muons, γ-rays and neutrons.

5.3.1   Cosmic-ray muons

The flux of the cosmic-ray muon at Kamioka observatory is $\sim 6 \times 10^{-8} \text{cm}^{-2}\text{s}^{-1}\text{sr}^{-1}$[86]. Muon flux as a function of depth in some underground laboratories in the world including our laboratory (labelled by "Super-Kamiokande") is shown in Figure 5.12 [86]. A very rough discussion explains that the muon contribution to the remaining background should be negligible because the muon flux in the underground laboratory was less than 10^{-3} times of that in the surface laboratory, while the background count rate in Kamioka RUN-I was about 40% of that in the surface laboratory. More quantitatively, the muon rate passing through the effective volume of the μ-TPC was calculated to be less than 2×10^{-4}cts/s. If we assume the muon rejection power was the same order of that of electron ($\sim 10^{-5}$ at 100 keVα.e.), the rate of a misidentified muon track as a nuclear track should be less than 2×10^{-1} counts/kg/days above 100 keVα.e. That count rate is much smaller than the one in Kamioka RUN-I shown in Figure 6.6. The secondary particles produced by cosmic-ray muons are studied as ambient gamma rays and neutrons in the following sections.

5.3.2   Gamma-rays

Ambient γ-rays are major background sources for direct dark matter searches. γ-rays are mainly produced in the decay of ^{40}K and the decay chains of ^{238}U and ^{232}Th shown in Figure A.1 and Figure A.3, respectively. Although the NEWAGE-0.3a detector had a strong rejection power against electron tracks as described in Section 4.3, mis-rejected γ-ray events might not be negligible.

We measured the γ-ray flux in our laboratory with a $5 \times 5 \times 1$cm^3 CsI(Tl) scintillator and a 5-inch photomultiplier(PMT R877, Hamamatsu) on October 23rd, 2008. The energy resolution was about 10% at 662keV. We set the scintillator on the μ-TPC, and the PMT signals were recorded by a PCI-3100 FADC with 20 MHz clock and the live time was recorded by a PCI-6200 50 MHz scaler. Measured spectrum with a live-time of 0.512 days is shown in Figure 5.13. Since the scintillator was on the NEWAGE-0.3a detector, the spectrum contained γ-rays emitted from the detector materials.

We then simulated the generation and propagation of γ-rays from ^{40}K, U-chain, and Th-chain in the rock. The incident γ-ray spectra from the U-chain and Th-chain are shown in Figure A.2 and Figure A.4, respectively. We considered the detector response and fitted these simulated spectra with the measured one treating the contaminations of the ^{40}K, ^{238}U, and ^{232}Th as free parameters. Estimated ambient γ-ray spectrum is shown in Figure 5.14, where fitting parameters have errors of +100% and -50%. The total flux of this result was consistent with that of a previous work [87] measured near the Super-Kaiokande with a germanium detector within the error. We then simulated the response of the NEWAGE-0.3a detector to this γ-ray flux. The result is shown by a red line in Figure 5.15. The
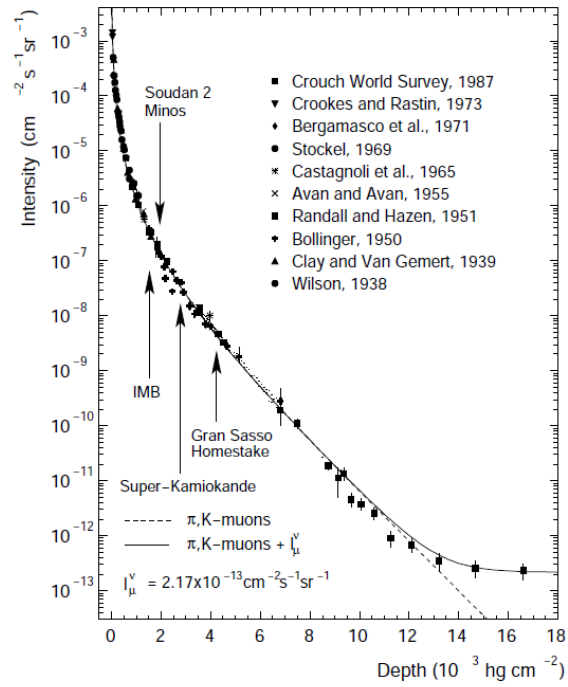
Figure 5.12: Cosmic ray muon flux as a function of depth in 10^3hg cm^{-2} equivalent to km w.e.[86].
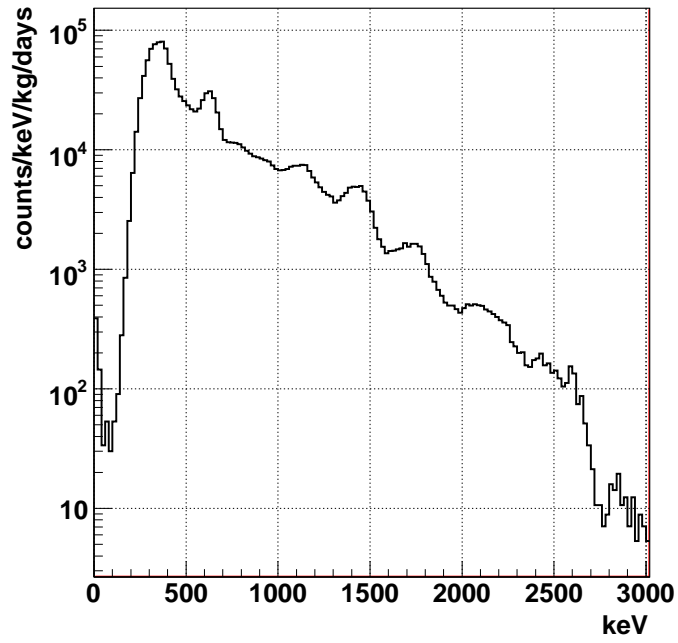
Figure 5.13: Ambient γ-ray spectrum measured in our laboratory with a CsI(Tl) scintillator.
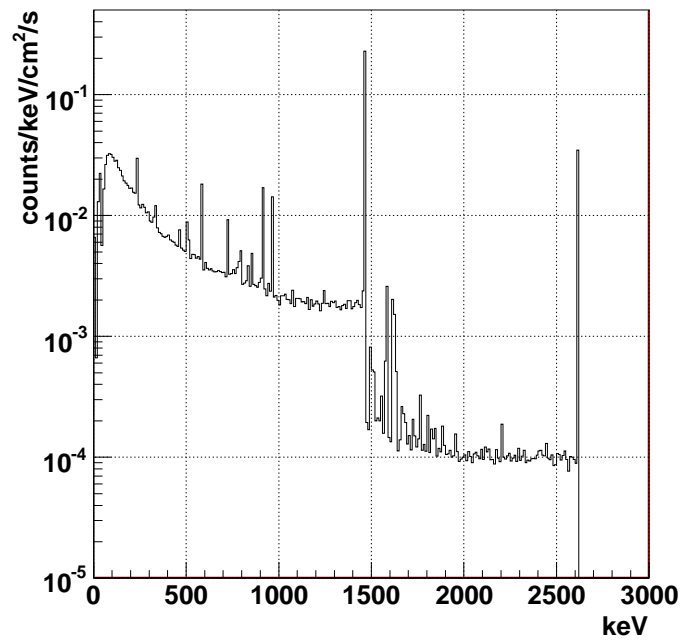
Figure 5.14: Estimated spectrum of the ambient γ-ray flux in our laboratory.

background rate by the γ-rays was about 7.1^{+7}_{-4} counts/keV/kg/days at 100 keVα.e., which was about $6^{+6}_{-3}\%$ of the remaining background.

5.3.3 Neutrons

The neutron flux inside the radiation shield in Kamioka Observatory was measured with a ^{3}He proportional counter by other group [88]. Results are shown in Table 5.2. Since the

location	thermal neutron	fast neutron
Kamioka Observatory	$< 4.8 \times 10^{-7}$	$\sim 1.9 \times 10^{-6}$

Table 5.2: Neutron flux (neutrons $cm^{-2}s^{-1}$) in Kamioka Observatory measured with a ^{3}He proportional counter[88].

.

cross sections of the neutron capture reaction are very small for both of carbon and fluorine nuclei, the contribution of thermal neutrons to the background spectrum was found to be negligible.

We then calculated an expected spectrum by ambient fast neutrons as follows. If the following conditions are satisfied, the energy spectrum of ambient fast neutrons is represented by the "1/E law".

- Neutron sources are distributed uniformly inside a boundless moderator.

- The moderator rarely absorbs neutrons.

The Kamioka Observatory satisfies the above conditions because the laboratory is surrounded by a base rock which contains a small amount of water. Thus the "1/E law" was assumed to calculate the non-thermal neutron flux in the laboratory. An expected background spectrum from fast neutrons is calculated with Geant4 as shown with a blue line in Figure 5.15. The expected spectrum was three orders of magnitude less than measured remaining background spectrum.

As a result of this session, we note that the ambient γ-ray is the major background source from outside the chamber and its contribution is 7.1^{+7}_{-4} counts/keV/kg/days, while that of neutron and muon are less than 1 counts/keV/kg/days. at 100 keVα.e.

5.4 Background from inside the chamber material (Contributions of α-particles)

Radioactive contaminations within the detector components often determine the background level in rare event measurements. The radioactive contaminations emit γ-rays, β-rays and α-rays. γ-rays and β-rays can be rejected with a rejection power of 1×10^{-5}, however α-rays can not be discriminated from nuclear recoils around 100 keVα.e. region.

Natural radioactive isotopes contaminated in most of the materials are ^{238}U, ^{232}Th and ^{40}K. As described in AppendixA, there are many α-decays and β-decays associating γ-ray emissions in the ^{238}U-chain and the ^{232}Th-chain. ^{40}K decays with a β-ray and a γ-ray. These isotopes could be contaminated in most of the material used in the detector components such as metal, plastic, glass-fiber, and so on. In addition, radons(Rn) in U-chain and Th-chain can emanate from the material as gas. Therefore, Rn and Rn progeny, which are the isotopes below Rn as shown in Figure A.1 and Figure A.3, might exist not only in the detector components but also in the gas volume.
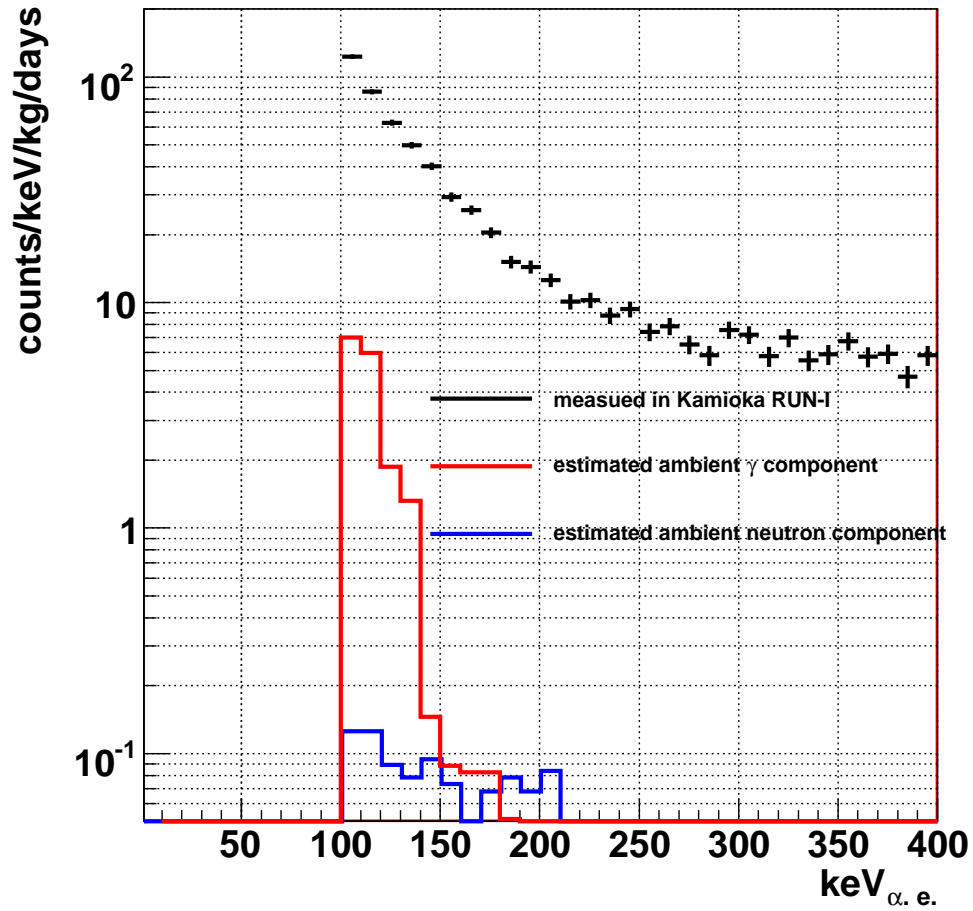
Figure 5.15: Estimated spectrum due to the ambient γ-rays (red line) and the ambient fast neutrons (blue line). Black histogram shows the measured spectrum in Kamioka RUN-I.

We studied the contributions of these contaminations to the observed spectra in the pilot runs. Although the number of β-rays emitted from one U-chain and Th-chain is as the same order as that of α-rays, the detection efficiency of an electron track of 100 keVα.e. is less than 1.0×10^{-5}. In addition, most of the γ-rays from U-chain, Th-chain and ^{40}K went out of the vacuum chamber and measured as parts of ambient γ-rays in Section 5.3.2. Thus we mainly studied the behavior of α-particles emitted from U-chain and Th-chain. Then we discuss β-rays from ^{40}K.

Although α-particles emitted from the U and Th chains have initial energy of more than 4 MeV, they sometimes deposit only their partial energy in the detection volume and make background events of about 100 keVα.e. The background due to α-particles from the U and Th chains detected with the NEWAGE-0.3a detector can be classified into five types according to the positions of their energy depositions. The categorization is listed below and is also shown in Figure 5.16.
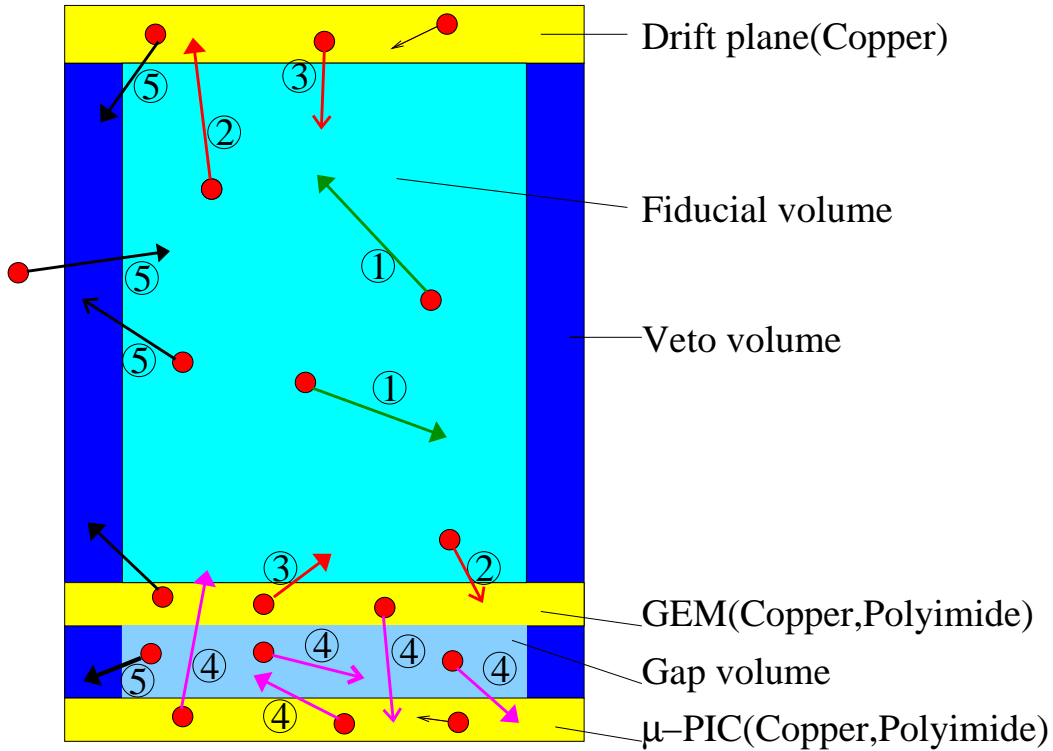
Figure 5.16: Five types of energy deposition of background α-particles. There are α-particles which run only in the fiducial volume (①), from the fiducial volume into the drift plane or the GEM(②), from the drift plane or the GEM into the fiducial volume (③), through the gap volume between the GEM and the μ-PIC (④), and through the veto volume (⑤). Particles with green arrows(①) deposit all of the initial energy in the fiducial volume, while those with red arrows(②, ③) deposit parts of the initial energy in fiducial volume. Energy depositions of purple arrows(④), are suppressed by the "suppression factor"(see text). α-particles categorized in ⑤ are rejected by a fiducial cut.

① α-particles which deposit all of their energy in the fiducial volume. In this case, α-particles are emitted from Rn progeny in the fiducial volume and stop in the fiducial volume.

② α-particles which deposit parts of their energy in the fiducial volume and then deposit rests of the energy in the drift plane or the GEM. In this case, α-particles are emitted from Rn progeny in the fiducial volume and run into the drift plane or the GEM.

③ α-particles which deposit parts of their energy in the drift plane or the GEM and then deposit the rests of the energy in the fiducial volume. In this case, α-particles are emitted from U or Th progeny in the drift plane or the GEM and come into the fiducial volume.

④ α-particles which run through the gap between the μ-PIC and the GEM. Their observed energies are "suppressed" compared to the events categorized in ① by the following three reasons. (i) They deposit only some parts of their energy in the gap volume, because their track length are generally longer than the gap length. (ii) These events are not multiplied by the GEM before being detected. Thus their energies are observed as if "suppressed" by the GEM gain compared to the events in ①. (iii) They run so close to the μ-PIC that the electrode-structure of the μ-PIC is seen. Thus the electron collection efficiency depend on their path. Measured energies of some events are suppressed by the collection inefficiencies.

Since we did not understand exact values of (ii) and (iii), we defined the combined effects as "suppression factor". The energy depositions in the gap region were detected with suppressed energies by the "suppression factor". In this case, some α-particles are emitted from U, or Th in the GEM and the μ-PIC, and come into the gap region between the GEM and the μ-PIC, while some α-particles are emitted from Rn progeny in the gap region and run into the the GEM or the μ-PIC.

⑤ α-particles which run through and deposit parts of the energy in the veto volume. We rejected them by the fiducial cut. In this case, α-particles are emitted from any place in the detector and run through the veto volume.

Some of the α-particles classified in ②,③, and ④, may make background events with an energy around 100 keV. Thus we calculated the partial energy depositions of α-particles with Geant4 assuming each radioactive contamination listed below.

Ⓐ ^{222}Rn abd ^{220}Rn progeny uniformly distributed in the gas volume

Ⓑ ^{238}U-chain and ^{232}Th-chain progeny uniformly distributed in the drift plane (the upside of the detection volume; 3mm-thickness cooper plate)

Ⓒ ^{238}U-chain and ^{232}Th-chain progeny uniformly distributed in the GEM (the downside of the detection volume; 5μm-thick cooper and 50μm-thick polyimide plate)

Ⓓ ^{238}U-chain and ^{232}Th-chain progeny uniformly distributed in the μPIC (100μm-thick cooper and 1mm-thick polyimide plate)

Calculated results are shown in the following sections and we also discuss the potentials of the contributions to the measured Kamioka RUN-I and RUN-II spectra.

5.4.1 Contributions of Rn progeny in gas chamber Ⓐ

Calculated spectra for case Ⓐ are shown in Figure 5.17. α-particles from Rn progeny classified in ① make a peak around 6 MeV, while those in ② make a flat continuous components from 100 keV to 3 MeV. The peak around 6 MeV was obviously observed and were used for the gain monitoring in Kamioka RUN-I and RUN-II, as shown in Figure 5.6. The flat continuous component would also make some contributions to the background spectrum of Kamioka RUN-I and RUN-II. Following discussions strongly indicate that this component dominated the measured spectrum above 200 keVα.e.
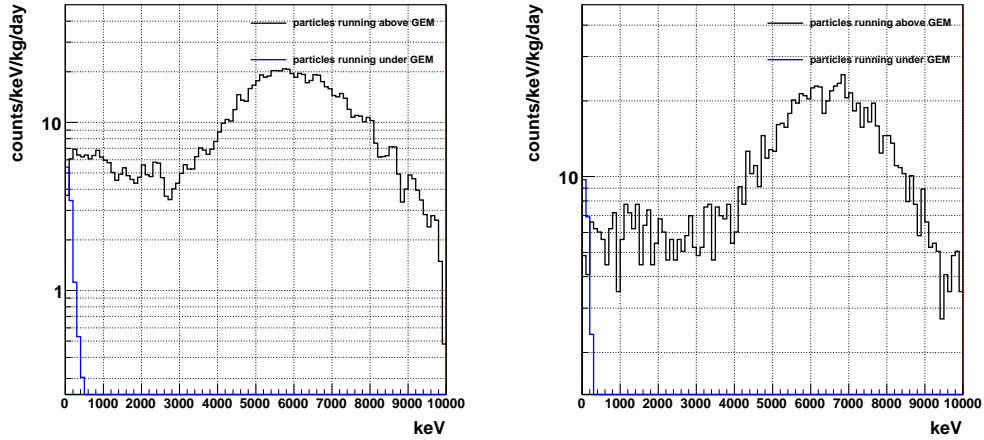
Figure 5.17: The results for Ⓐ: Expected spectra of α-particles emitted from ^{222}Rn- (left) and ^{220}Rn- (right) progeny in the gas volume. We assumed their density of 3.81×10^{-15}g/g and 3.27×10^{-20}g/g, respectively. These contamination were determined by the count rate around 6MeV of the measured spectrum in Kamioka RUN-I. Black and blue histograms show deposit energy above (the deposit position ① ②) and under the GEM (the deposit position ④.) , respectively.

Time variation of the peak around 6MeV in Kamioka RUN-I and RUN-II

We observed time variations of the peak around 6MeV in Kamioka RUN-I and RUN-II as shown in Figure 5.18 and Figure 5.19, respectively.

These variations were explained by the following scenarios. We assume that there is no Rn gas in the gas volume just after the gas refill unless we intentionally contaminate. Then the radons are produced in the U and Th chains within the detector components and emanate into in the gas volume. We assume the production rates of ^{222}Rn and ^{220}Rn in the material are constant, because U and Th chains in the materials are in the radiation equilibrium. Thus the Rn emanation rate from the material to the gas volume were assumed constant as $^{220}R_{\text{out}}$ and $^{222}R_{\text{out}}$ [cts/s]. Therefore the rates of Rn decay in the gas volume are described by Eq.(5.1).

$$R_{^{220}\text{Rn decay}}(t) = ^{220}R_{\text{out}} \times (1 - \exp(-\frac{t}{T_1}))$$

$$R_{^{222}\text{Rn decay}}(t) = ^{222}R_{\text{out}} \times (1 - \exp(-\frac{t}{T_2})), \qquad (5.1)$$

where t is time from a gas refill, $T_1 = 79.3$s and $T_2 = 5.516$days, are decay times of ^{220}Rn, ^{222}Rn, respectively. The initial condition gives $R_{^{220}\text{Rn decay}}(0) = R_{^{222}\text{Rn decay}}(0) = 0$. In the case of ^{222}Rn progeny, since the decay times of isotopes down to ^{210}Pb are much shorter than 5.516 days, these progeny become in the radiation equilibrium in a few seconds. Thus the decay rates of those ^{222}Rn progeny are same as that of ^{222}Rn, while the decay rate of progeny after ^{210}Pb can be negligible because a life-time of ^{210}Pb is much longer than that of ^{222}Rn.

Based on those assumption were applied the time variation in Kamioka RUN-I. We fitted
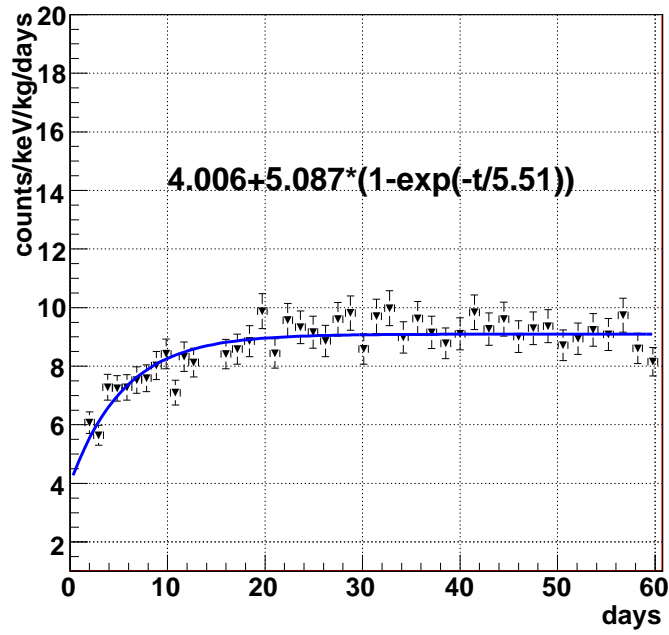
Figure 5.18: Time dependence of the count rate around 6 MeV in Kamioka RUN-I-2. X-axis is the days from a gas refill. A blue line is the fitted function of $C_1 + R_{out} \times (1 - \exp(-t/5.5))$, where $C_1 = 4.0 \pm 0.40$ and $R_{out} = 5.1 \pm 0.44$. This time-dependence indicates existence of ^{222}Rn.
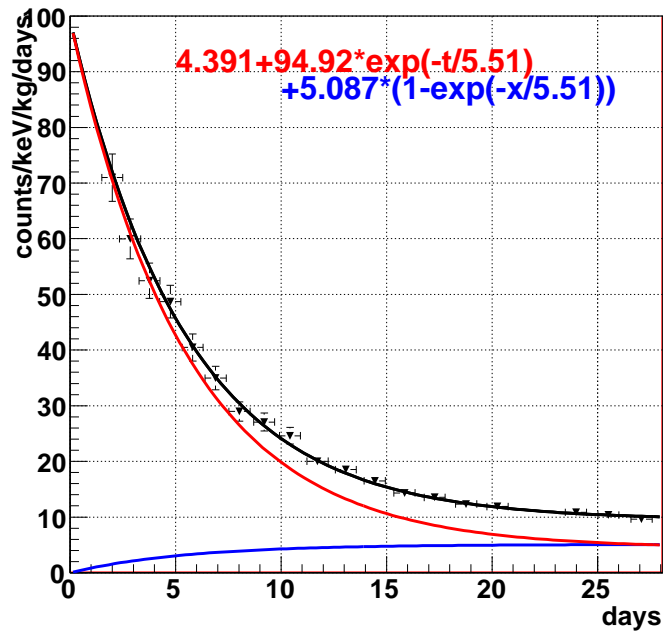
Figure 5.19: Time dependence of the count rate around 6 MeV in Kamioka RUN-II-1. X-axis is the days from a gas refill. A black line is the best fitted function of $C_2 + R_{\mathrm{init}} \times \exp(-t/5.5) + R_{\mathrm{out}} \times (1 - \exp(-t/5.5))$ where $C_2 = 4.4 \pm 0.29$ and $R_{\mathrm{init}} = 94 \pm 3.8$ were best fit parameters. $R_{\mathrm{out}} = 5.1$ was a fixed parameter. The blue line is the fitted function in Figure 5.18 as an expected component of ^{222}Rn emanations. The red line shows component of the initial ^{222}Rn decay and non ^{222}Rn components.

the time-dependence of the count rate shown in Figure 5.18 with a function of

$$R_{\text{peak}}(t) = R_{^{222}\text{Rn decay}}(t) + C_1 = ^{222}R_{\text{out}} \times (1 - \exp(-\frac{t}{T_2})) + C_1, \quad (5.2)$$

where C_1 is a constant component which does not have a variations in a time-scale of a day. C_1 should contains ^{220}Rn contribution but we were not able to measure the amount of ^{220}Rn contribution. Thus we defined this kind of constant component as a non-^{222}Rn component. We took $^{222}R_{\text{out}}$ and C_1 as free parameters and got the best-fit function as shown by a blue line in Figure 5.18 with parameters of $C_1 = 4.0 \pm 0.40$ and $R_{\text{out}} = 5.1 \pm 0.44$. The time variations of the peak around 6 MeV in Kamioka RUN-I were explained well with these parameters.

On th other hand, there were some radon in the gas volume just after the gas refill in Kamioka RUN-II (5.19). Measured peak around 6 MeV due to α-particles at the beginning of Kamioka RUN-II was ten times larger than that of the Kamoika RUN-I as described in Section 5.2.2. We assumed that R_{init} is the amount of ^{222}Rn at the time of gas refill($t = 0$) and R_{out} is the same as that in Kamioka RUN-I. We fitted the time-dependence of the count rate shown of Figure 5.19 with a function of

$$R_{^{222}\text{Rn decay}}(t) = R_{\text{init}} \exp(-\frac{t}{T_2}) + R_{\text{out}} \times (1 - \exp(-\frac{t}{T_2})) + C_2, \quad (5.3)$$

where C_2 is a non-^{222}Rn component in Kamioka RUN-II. We took R_{init} and C_2 as free parameters and fixed $R_{\text{out}} = 5.1$, which was the best fit parameter of the R_{out} in Figure 5.18. The best-fit function is shown by a black line in the Figure 5.19. This line consists of two component: a decreasing component (blue) due to the initial Rn and an increasing component (red) due to the emanation from materials. The C_1 in Figure 5.18 agrees with C_2 in Figure 5.19 within fitting errors. Thus the only difference between the 5.18 and Figure 5.19 is the term of the initial ^{222}Rn, $R_{\text{init}} \exp(-\frac{t}{T_2})$.

We note these characteristic time variations strongly support existence of ^{222}Rn although there still exist unidentified components such as ^{220}Rn around 6 MeV.

Correlation between the low energy and high energy count rates

We then studied a contribution of α-particles to the low energy spectrum. The calculated spectrum shown in Figure 5.17 has a flat component below 3 MeV and the measured one in Kamioka RUN-II has also a flat component around 200 keVα.e. shown in Figure 5.8. This similarity implies a contribution of the ^{222}Rn to the low energy spectrum. We therefore, studied the correlation between the low energy count rate with that of the peak around 6MeV in Kamioka RUN-II. The correlation was observed as shown in Figure 5.20. This correlation indicates that radon and its progeny contributed to the low energy spectrum as the calculated spectrum indicated.

We finally discuss how the ratio of the ^{222}Rn to ^{220}Rn affects the low energy spectrum. A simple assumption, that the contributions of ^{222}Rn to measured peak around 6 MeV was 100%, gives the contamination of ^{222}Rn of 3.8×10^{-15}g/g by fitting the measured in Kamioka RUN-I with the calculated spectrum around 6MeV. Figure 5.21 shows spectra measured in Kamioka RUN-I (red histogram) and calculated (black and blue) in the energy range of 100-400keVα.e. The calculated one has about 5 counts/keV/kg/days contribution above 200 keVα.e. and about 6 counts/keV/kg/days contribution at 100 keV without the contribution of gap region events. In the opposite where the case contribution ^{220}Rn was 100% results a 6 counts/keV/kg/days contribution above 200 keVα.e. and 6 counts/keV/kg/days contributions at 100 keVα.e. without the contribution of gap region events. Thus we es-
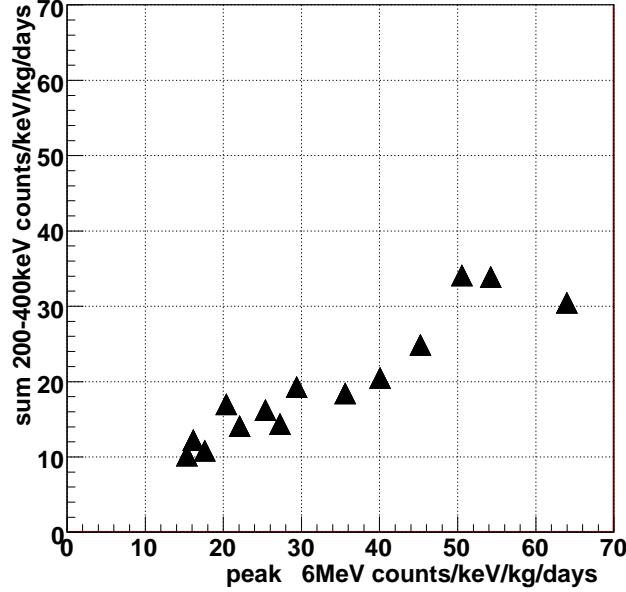
Figure 5.20: Correlation between the high energy (6 MeV) count rate and that of low energy(200-400keVα.e.) in Kamioka RUN-II.

timated contributions of the radons are dominant above 200 keVα.e. with a count rate of about 5counts/keV/kg/days and about 5counts/keV/kg/days at 100 keVα.e. independent of the ratio of ^{222}Rn to ^{220}Rn in the gas volume. Contribution of the gap region events is described in Section 5.6.

5.4.2 Contributions of U and Th in the drift plane Ⓑ

Calculated spectra for case Ⓑ are shown in Figure 5.22. Most of the α-particles deposit their energy in the drift plane classified as ③. The spectra are nearly flat in low energy under 400 keVα.e. in contrast to the measured spectrum in Kamioka RUN-I (See Figure 5.23). Since the expected contributions of radons (Ⓐ)at 400 keVα.e. (6±2 counts/keV/kg/days) dominated the measured count rate at 400 keVα.e.(6±1 counts/keV/kg/days), the upper limit of the contributions of case Ⓑ at 400 keVα.e. was estimated to be 3 counts/keV/kg/days. Thus we estimated the contributions of case Ⓑ at 100 keVα.e. is less than 5 counts/keV/kg/days, by the shape of spectrum.

5.4.3 Contributions of U and Th in the GEM and the μ-PIC Ⓒ Ⓓ

Simulated spectra for case Ⓒ and Ⓓ are shown in Figure 5.24 and Figure 5.25. Events between the μ-PIC and the GEM (③) contribute to the low energy spectrum as shown in the blue line in the figures. The count rate of these events is 100 times larger than that in the fiducial volume (②, black line in the figures). This characteristic distribution is caused by the suppression factor as described in the beginning of Section 5.4. We note that there are no α-particles in the U-chain which have energy high enough ($\sim$ 8.5 MeV) to penetrate both the gap region and the GEM, and reach to the fiducial volume, while ^{212}Po in the Th-chain emits an α-particle with energy of 8.785 MeV, which is high enough to bring the
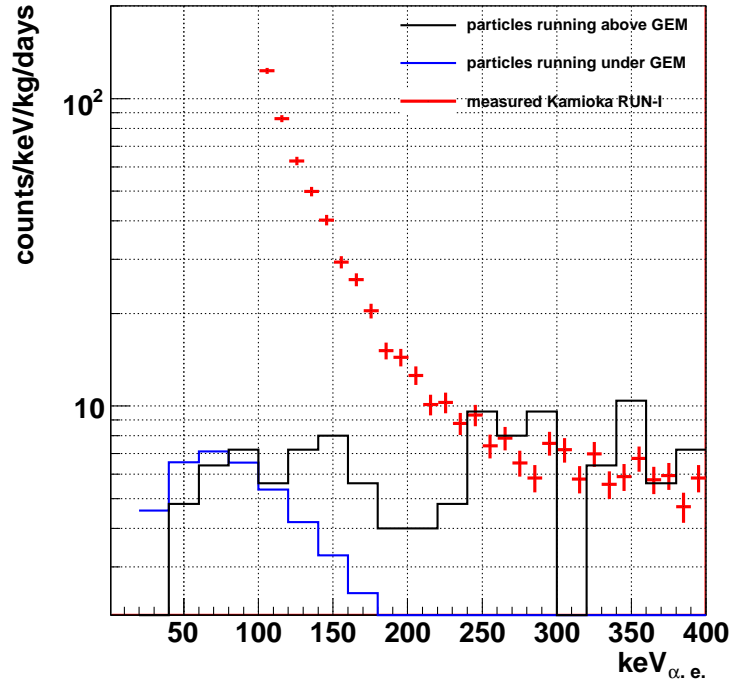
Figure 5.21: Measured Kamioka RUN-I spectrum (red) and a calculated contributions of ^{222}Rn (black and blue histogram). Th black line and the blue line are estimated contributions from ^{222}Rn with deposit positions of ① and ④, respectively. We assumed 3.81×10^{-15}g/g of ^{222}Rn in the gas volume to fit the peak around 6 MeV with that of the measured spectrum in Kamioka RUN-I.
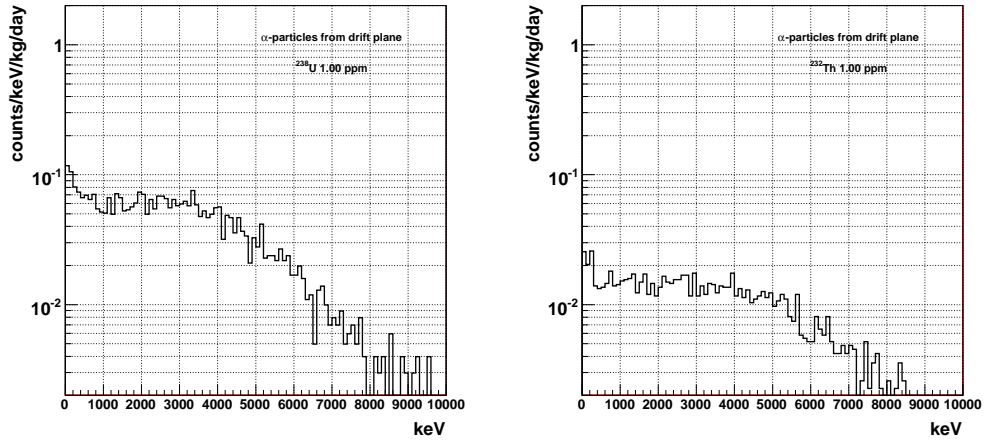
Figure 5.22: The results for ⑧: Expected spectra of α-particles emitted from ^{238}U- (left) and ^{232}Th- (right) progeny in the drift plane. We assumed that both of their contaminations are 1.0×10^{-6}g/g as references. All particles deposit energy as ③.
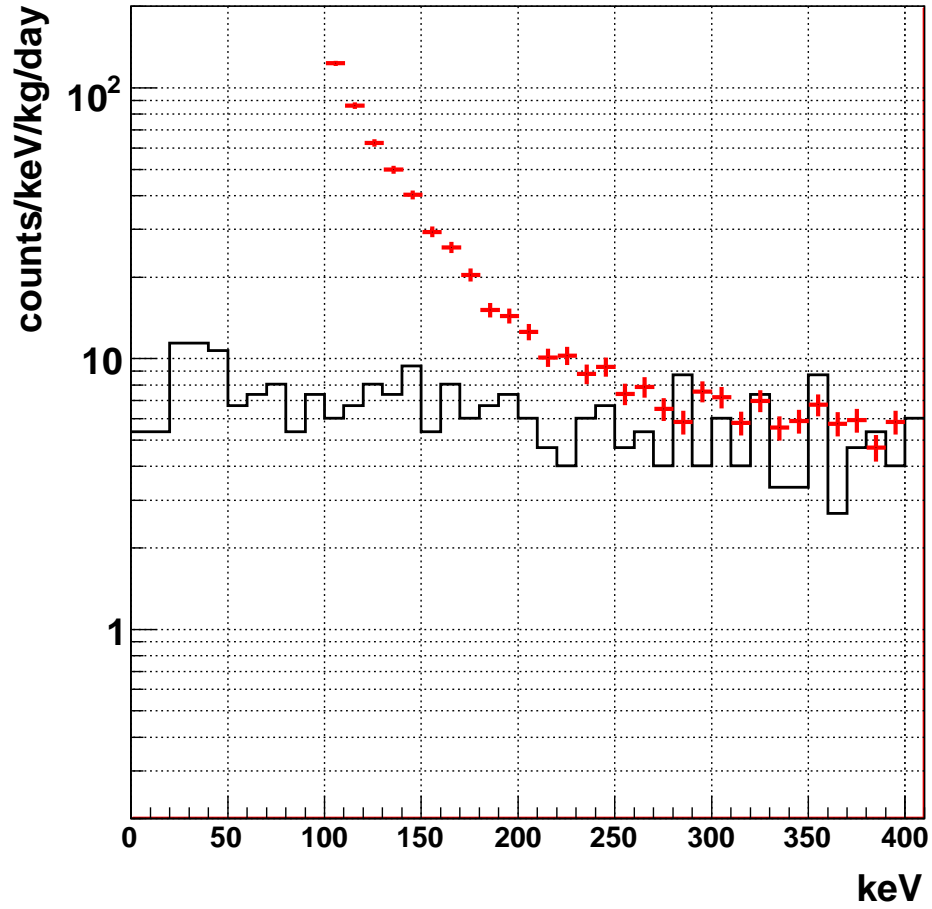
Figure 5.23: Comparison of shapes of calculated spectrum for case Ⓑ and measured spectrum in Kamioka Run-I.
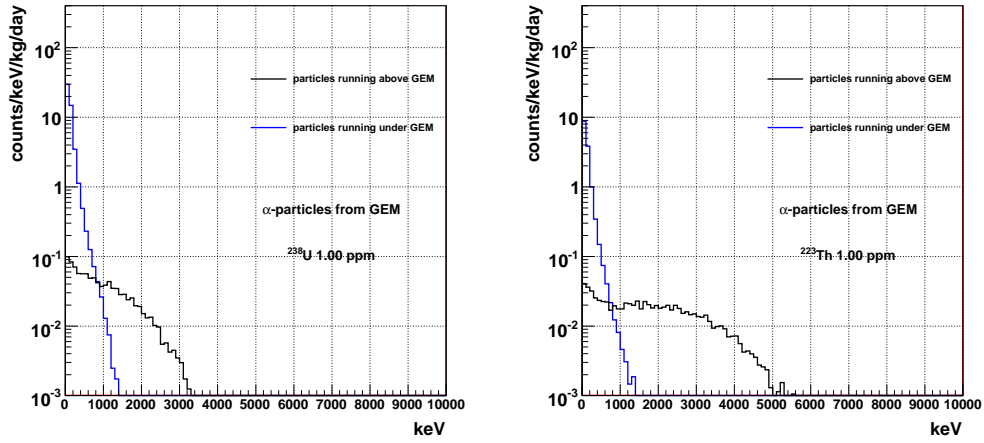
Figure 5.24: The results for Ⓒ: Expected spectra of α-particles emitted from ^{238}U- (left) and ^{232}Th- (right) progeny in the GEM. We assumed that both of their density are 1.0×10^{-6}g/g as references. Black and blue histograms show deposit energy above (the deposit position ③) and and under the GEM (the deposit position ④), respectively.

Figure 5.25: The results for Ⓓ. Expected spectra of α-particles emitted from ^{238}U- (left) and ^{232}Th- (right) progeny in the μ-PIC. We assumed both of their contaminations are 1.0×10^{-6}g/g as references. Black and blue histograms show the energy deposited above (the deposit position ③) and under the GEM, (the deposit position ④), respectively.

α-particle into the fiducial volume. Thus, there is no event of ② with black line in the left panel of Figure 5.25, but some events are in the right panel of Figure 5.25(right).

Since there are uncertain parameters of the suppression factor, and the amounts of ^{238}U and ^{232}Th in this calculation, the calculated spectrum around 100 keV also has much uncertainty. Actually, the shapes of the "suppressed" (blue) spectra are affected by the suppression factor. Figure 5.26 shows expected spectra with the suppression factor of 3, 5, 10, and 15 respectively. We simulated the spectra due to the α-particles from the ^{238}U chain in the μ-PIC assuming a ^{238}U density of 5×10^{-6}g/g. The red histogram shows measured background spectrum in Kamioka RUN-I. It was seen that larger suppression factor gave steeper spectra. In addition, since there might be a position-dependence of the GEM gas gain like the total gas gain, the spectrum might be a combined one of the spectra with various suppression factors. And these events possibly contribute to the significant amount of the low energy background spectrum in Kamioka RUN-I. As a result of studies in this section the contributions of the ③-Ⓒ and ③-Ⓓ have potential to explain the measured spectrum at 100 keVα.e.

5.5 β-ray from ^{40}K inside the vacuum chamber

We discuss β-rays from ^{40}K inside the vacuum chamber. Since the maximum energy of β-ray from ^{40}K is about 1.3 MeV, they can not penetrate the walls of the detection volume. Thus we consider inner parts that faced on the detection volume. For producing a count rate of 100 counts/keV/kg/days events at 100 keVα.e. in the NEWAGE-0.3a detector, ^{40}K needs the number of $O(10^{-5})$mol atoms in inner parts considered the detection efficiency of 10^{-5} at 100 keVα.e. This amount is equivalent to 300 g of the natural K assuming the natural abundance of ^{40}K is 0.0117%. The total mass of the considered parts was about 1.4kg (440g(wall)+140g(μ-PIC+GEM)+860g(Drift plane)). Since the typical K contamination was no more than 1% in those materials, the contribution of ^{40}K was less than 5 counts/keV/kg/days.
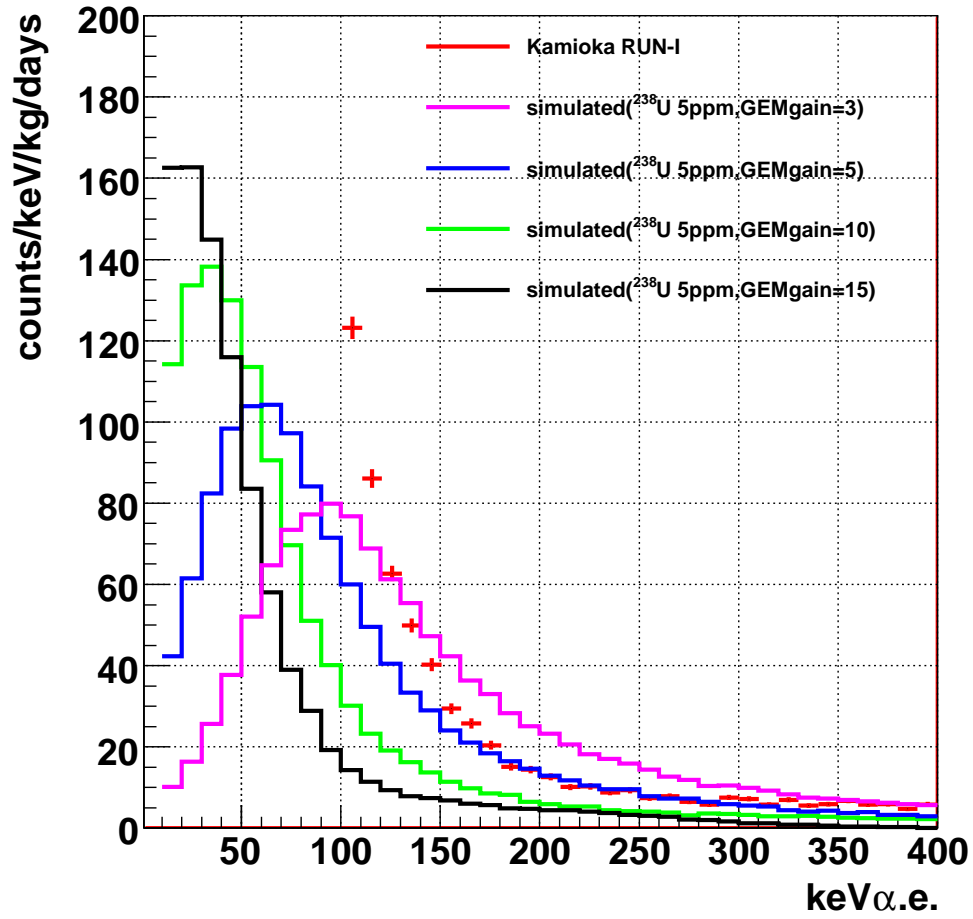
Figure 5.26: Measured spectrum of Kamioka RUN-I and some of calculated contributions of the μ-PIC contamination with 5.0×10^{-6}g/g ^{238}U for given suppression factors. (purple $\times 3$, blue $\times 5$, green $\times 10$, black $\times 15$), Contaminations in the GEM would make a similar contribution. This figure suggests the events in gap between the μ-PIC and the GEM can contribute to the low energy spectrum.

5.6   Summary of the background study

particle	counts/keV/kg/days at 100keV
γ-ray	~ 7
cosmic muon	$< \sim 10^{-1}$
fast neutron	$\sim 10^{-1}$
thermal neutron	negligible

Table 5.3: Estimated contributions of the background sources outside of the vacuum chamber at 100 keVα.e..

α-particles (counts/kg/keV/days)				
	gas volume(A)	drift plane(B)	GEM(C)	μ-PIC(D)
fiducial only(1)	none	none	none	none
fiducial+materials(2)(3)	~ 5	< 5	$\sim$X/100	$\sim$X/1000
gap region+materials(4)	$< \sim 5$	none	X	X
with veto region(5)	none	none	none	none
Section	(5.4.1)	(5.4.2)	(5.4.3)	
β-particles (counts/kg/keV/days)				
U-chains	negligible			
Th-chains	negligible			
^{40}K	< 5 (Section 5.5)			

Table 5.4: Estimated contributions to the measured spectrum at 100 keVα.e. of inside the vacuum chamber. Issues of columns show materials with contaminations which emit α-particles. Issues of rows show the positions of the energy deposition. X is unknown but can potentially to be as high as 100.

We summarize the effects of the background sources outside and inside the vacuum chamber in Table 5.3 and Table 5.4, respectively. Although a confirmation by a further measurement is still required, "X" in the table can potentially be as high as 100. We found that contributions of (C)-(4) and (D)-(4) could be the most dominant components of the measured spectrum at 100 keVα.e. in Kamioka RUN-I, and second dominant components were (A)-(2) and (A)-(3). The contribution of the outside sources was found to be less than that of internal sources. We have to reduce the internal background in order to achieve a lower background. Figure 5.27 shows one of example spectrum to explain the measured one in Kamioka RUN-I, where we assumed ^{222}Rn density in the gas volume region is 3.8×10^{-15}g/g from a count rate around 6 MeV and calculated ambient gamma-ray contribution in Section 5.3.2. ^{238}U density in the GEM is 4.0×10^{-6}g/g and the suppression factor of 15 were assumed to fit the measured spectrum in Kamioka RUN-I and other contribution were ignored.

Reducing the contaminations in the detector components is the most fundamental solution, however, a large amount of technical efforts are required to develop radio-pure GEMs and μ-PICs. Another approach is to realize a complete fiducial cut to reject all background in Table 5.4, by detecting the absolute Z position of each event. However, we need some technical breakthrough to pursue this approach.

A quick way to confirm the discussions above and reduce the background rate at 100 keVα.e. is to focus on the gap region (4). This region causes 100 times larger background than the fiducial regions as discussed in Section 5.4.3. The spectrum shapes of (C)-(4) and D-(4) could be controlled by the GEM gains as seen in Figure 5.26. A higher GEM gain would make the spectrum steeper and decrease the count rate at 100 keVα.e. If we can operate the GEM
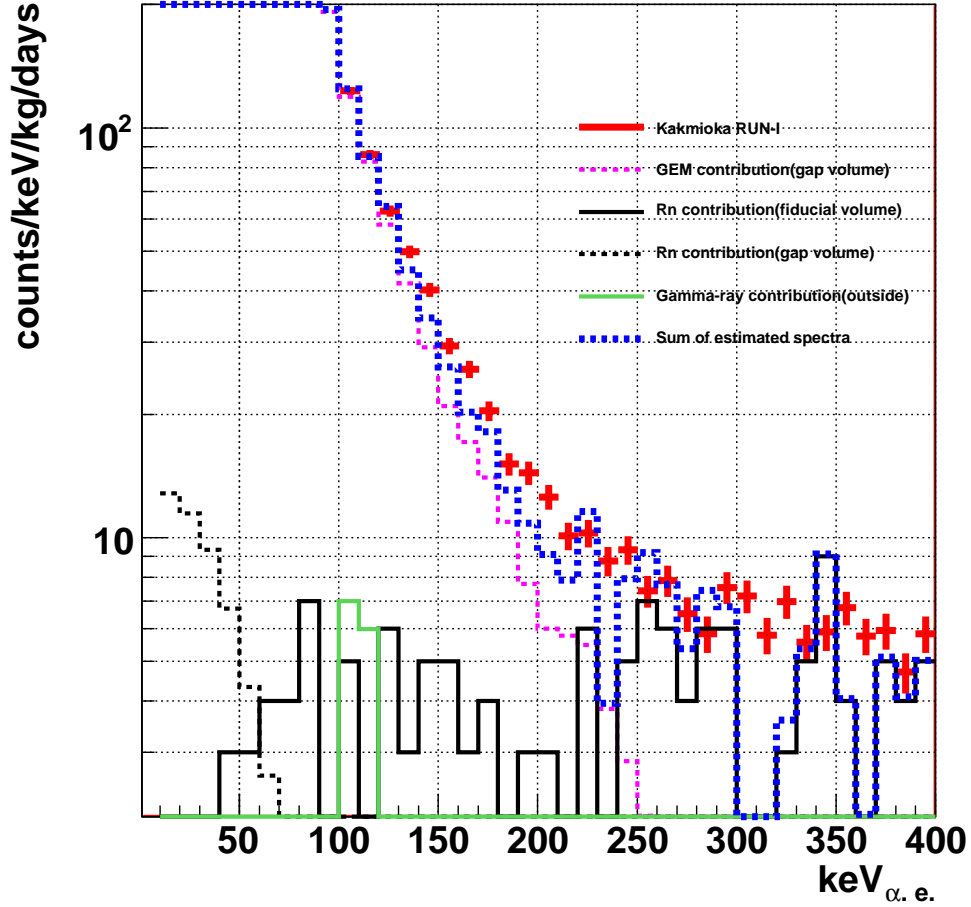
Figure 5.27: Example spectra explaining measured one in Kamioka RUN-I. We assumed ^{222}Rn contamination of 3.8×10^{-15}g/g in the gas volume (black solid and dotted lines), calculated ambient gamma-ray contribution (solid green line), ^{238}U contamination in the GEM of 4.0×10^{-6}g/g (blue lines), and the suppression factor of 15. Other contributions were ignored. The dotted lines strongly depends on the suppression factor, which was actually uncertain.

with a gain ten times higher than that of Kamioka RUN-I and RUN-II, the contribution of Ⓒ-④ should be comparable with Ⓒ-③. We had not confirmed a stable operation of GEM with such a high gain, and the risk of damaging the GEM might be too high. Thus we decided to operate the NEWAGE-0.3a detector with about twice lager GEM gain to confirm the contribution of Ⓒ-④ and Ⓓ-④ and to perform a lower background dark matter search.

Chapter 6

Dark matter search in Kamioka mine

6.1 Dark matter search run in Kamioka mine

Based on the results of the pilot runs and the background studies described in Chapter 5, we optimized the operation parameters and performed a dark matter search run (Kamioka RUN-III). Kamioka RUN-III was performed from September 11th, 2008 to Decsenmber 4th 2008. The position and alignment of the NEWAGE-0.3a detector were same as those in Kamioka RUN-I and RUN-II.(See Section 5.2.) We operated the GEM with a higher gain than that in Kamioka RUN-I in order to suppress the background α-ray events interacted in the gap between the GEM and the μ-PIC (events categorized as ④-Ⓐ, ④-Ⓒ and ④-Ⓓ in Table 5.4). Operation parameters and run properties of Kamioka RUN-III are listed in Table 6.1 and Table 6.2, respectively.

	RUN-I&RUN-II	RUN-III
μ-PIC anodes	515V	455V
μ-PIC gain	$\sim \times 700$	$\sim \times 300$
GEM_{up}	-915V	-915V
GEM_{down}	-650V	-605V
GEM_{up}- GEM_{down}	-265V	-310V
GEM gain	$\sim \times 3$	$\sim \times 8$
Drift field	240 V/cm	
Gas	CF_4	
Pressure	152 torr	
fiducial volume	$20 \times 25 \times 31 cm^3$	
Placement	36°25'N, 137°18'E 2700m w.e.	
X-axis direction	S87E	

Table 6.1: Operation parameter of μ-TPC.

The time dependencies of the drift velocity and the detection efficiency at 100keVα.e. were measured as shown in Figure 6.1, and Figure 6.2, by the method described in Section 4.2.1 and Section 4.2.5, respectively. The red points in the figures show measured values and black error bars show interpolated values used in the analysis. Decreases due to the gas impurity and recoveries due to the gas refills were observed in the both parameters.

run ID	date	live time [day]	effective mass [g]	exposure[kg days]
III-1	Sep.11th -Oct.1st, 2008	17.81	11.48	0.204
III-2	Oct.2nd -Nov.11th, 2008	10.01	11.48	0.115
III-3	Nov.13th -Dec.4th, 2008	17.90	11.48	0.205
	Kamioka RUN-III total exposure			0.524

Table 6.2: Properties of the dark matter search run (Kamioka RUN-III) in Kamioka mine.

We monitored the gas gain during Kamioka RUN-III using the peak around 6 MeV due to radons by the method described in Section 4.2.4, as shown in Figure 6.3. Furthermore, the count rate around 6 MeV was monitored as shown in Figure 6.4, as like in Chapter 5. We unintentionally contaminated the chamber gas with radon gas when we started Kamioka RUN-III-2. The radon-contaminated period (from October 2nd to October 24th, 2008) obviously seen in Figure 6.4 was eliminated from the dark matter search analysis.

All data obtained in Kamioka RUN-III except for the radon-contaminated period were analyzed by the same manner we did in the pilot runs described in Section 5.2. We applied the nuclear selection cut and the fiducial cut, then corrected calibration factors and detection efficiencies with the monitored parameters. Obtained energy spectrum is shown in Figure
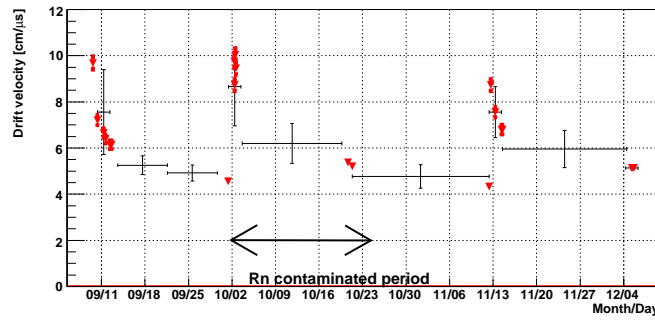
Figure 6.1: Drift velocities during the dark matter run (Kamioka RUN-III). Red points show measured values. Black error bars show interpolated values for the analysis.
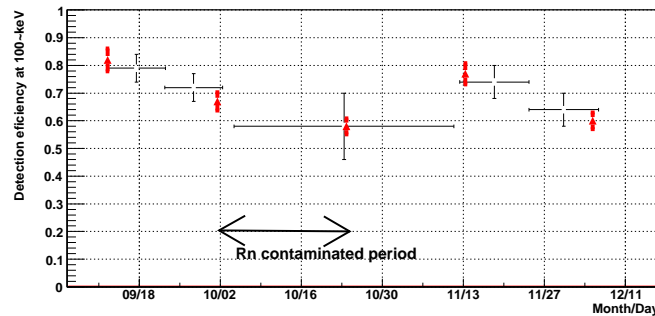
Figure 6.2: Nuclear detection efficiency at 100 keVα.e. during the dark matter run (Kamioka RUN-III). Red points show measured values. Black error bars show interpolated and extrapolated values for the analysis.
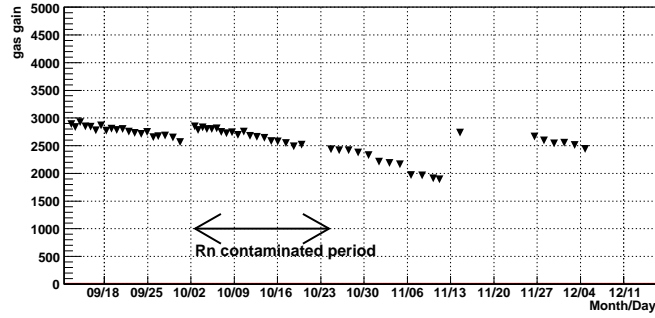
Figure 6.3: Monitored gas gain during the dark matter run(Kamioka RUN-III).
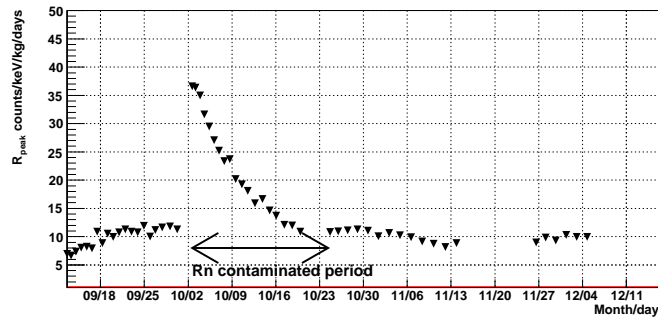
Figure 6.4: Monitored count rate around 6 MeV due to Rn progeny during the dark matter run (Kamioka RUN-III)

6.5. We also compared the energy spectrum in Figure 6.6 with those of the pilot runs. The count rate in Kamioka RUN-III was about 1/3 of that in Kamioka RUN-I at 100 keVα.e. We then plotted the directions of nuclear recoil tracks with an energy range of 100-400 keVα.e. with black points in Figure 6.7(top) and also directions of the Cygnus from which WIMP-wind are expected at each event time with purple circle marks as the same manner we have done in Chapter 5. We calculated θ, the angle between the recoil direction and the WIMP-wind direction for each event, and drew the $|\cos\theta|$ distribution shown in Figure 6.7(bottom). This direction result was divided into 15 distributions by the measured recoil energy of every 20 keVα.e. as shown in from Figure 6.8 to Figure 6.11.
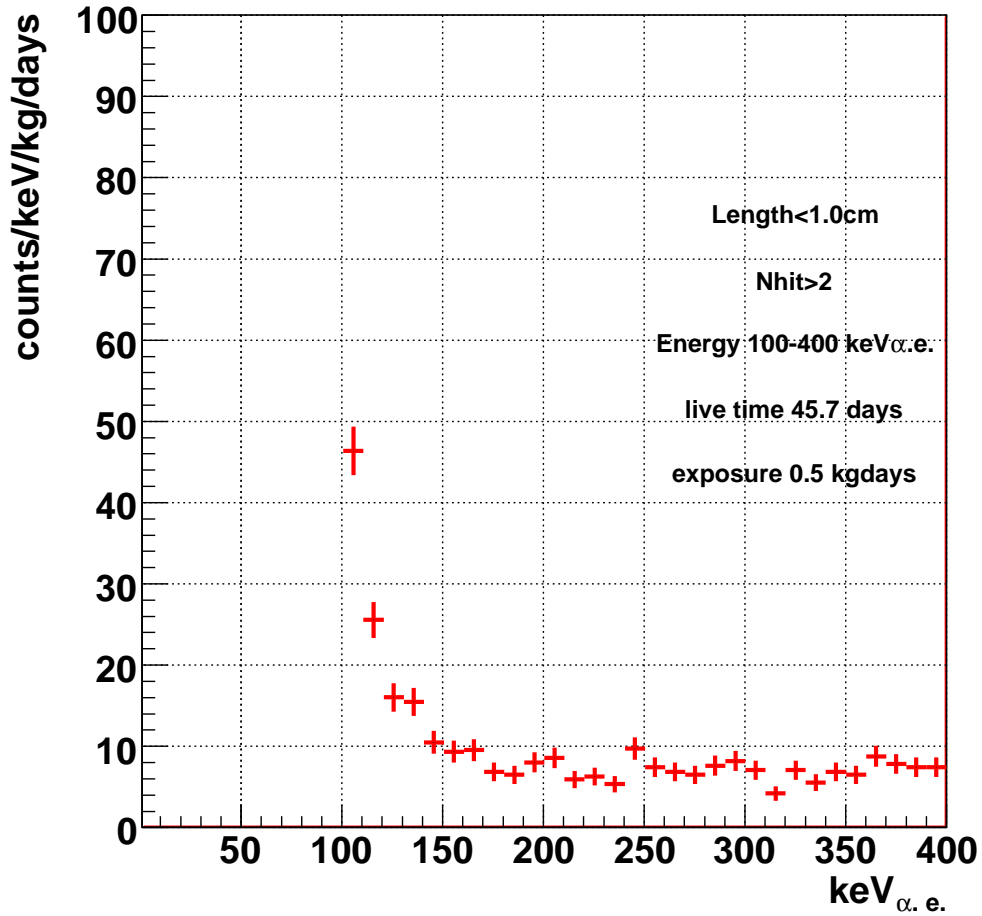
Figure 6.5: Obtained spectrum in Kamioka RUN-III.
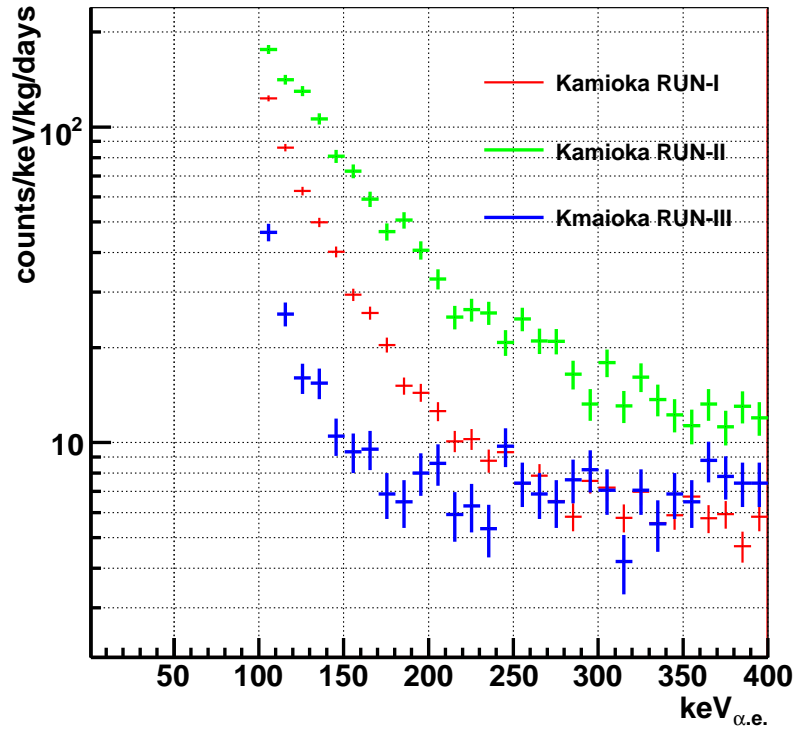
Figure 6.6: Obtained energy spectrum in the pilot and DM search runs (RUN-I, RUN-II and RUN-III)at Kamioka observatory. RUN-I is operated with the same parameters as the surface run, RUN-II is a radon-rich run and RUN-III is operated with optimized parameters listed in Table 6.1.
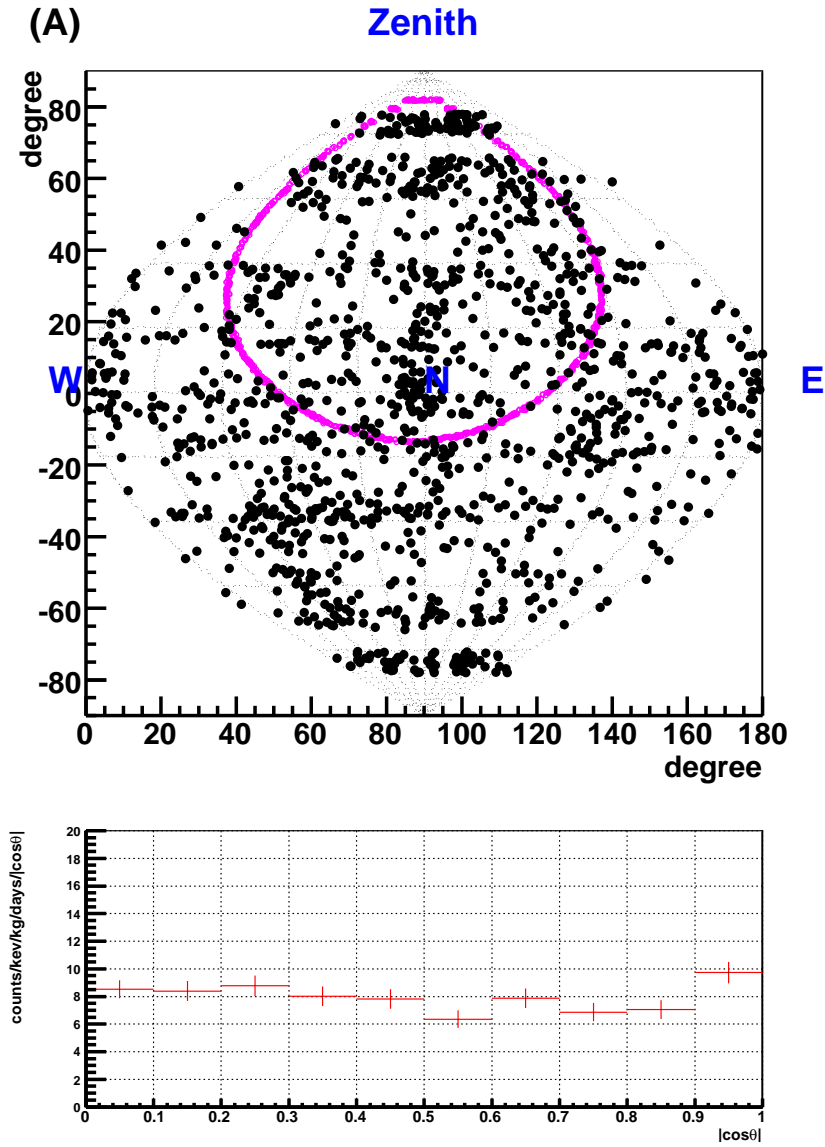
Figure 6.7: Obtained direction of the nuclear tracks plot (up) and $|\cos\theta|$ distribution(down) with energy range of 100-400 keVα.e. in Kamioka RUN-III.
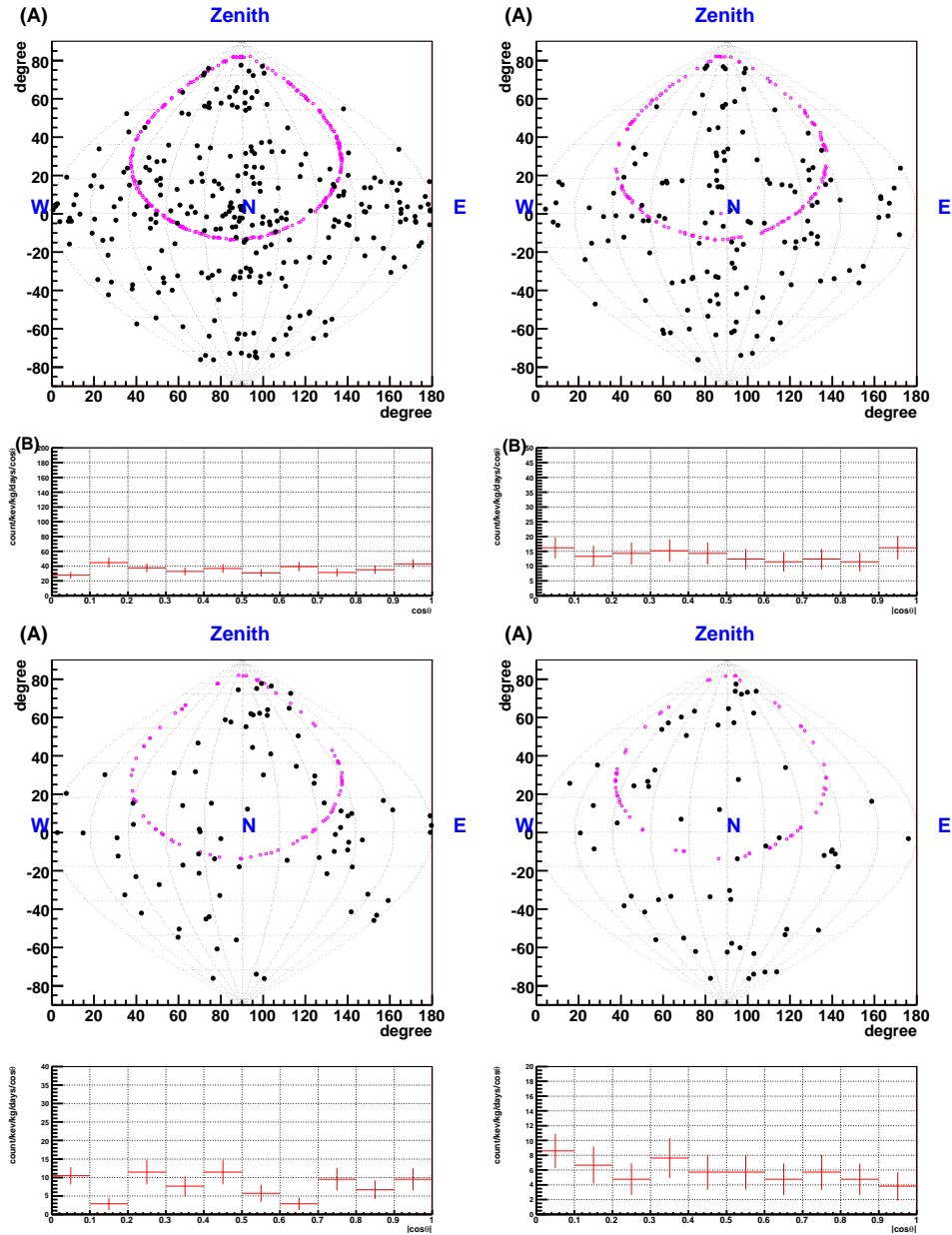
Figure 6.8:   The obtained direction of the nuclear tracks plots and $|\cos\theta|$ distributions with energy range of 100-120 keVα.e.(top left), 120-140 keVα.e.(top right), 140-160 keVα.e.(bottom left) and 160-180 keVα.e.(bottom right) in Kamioka RUN-III.
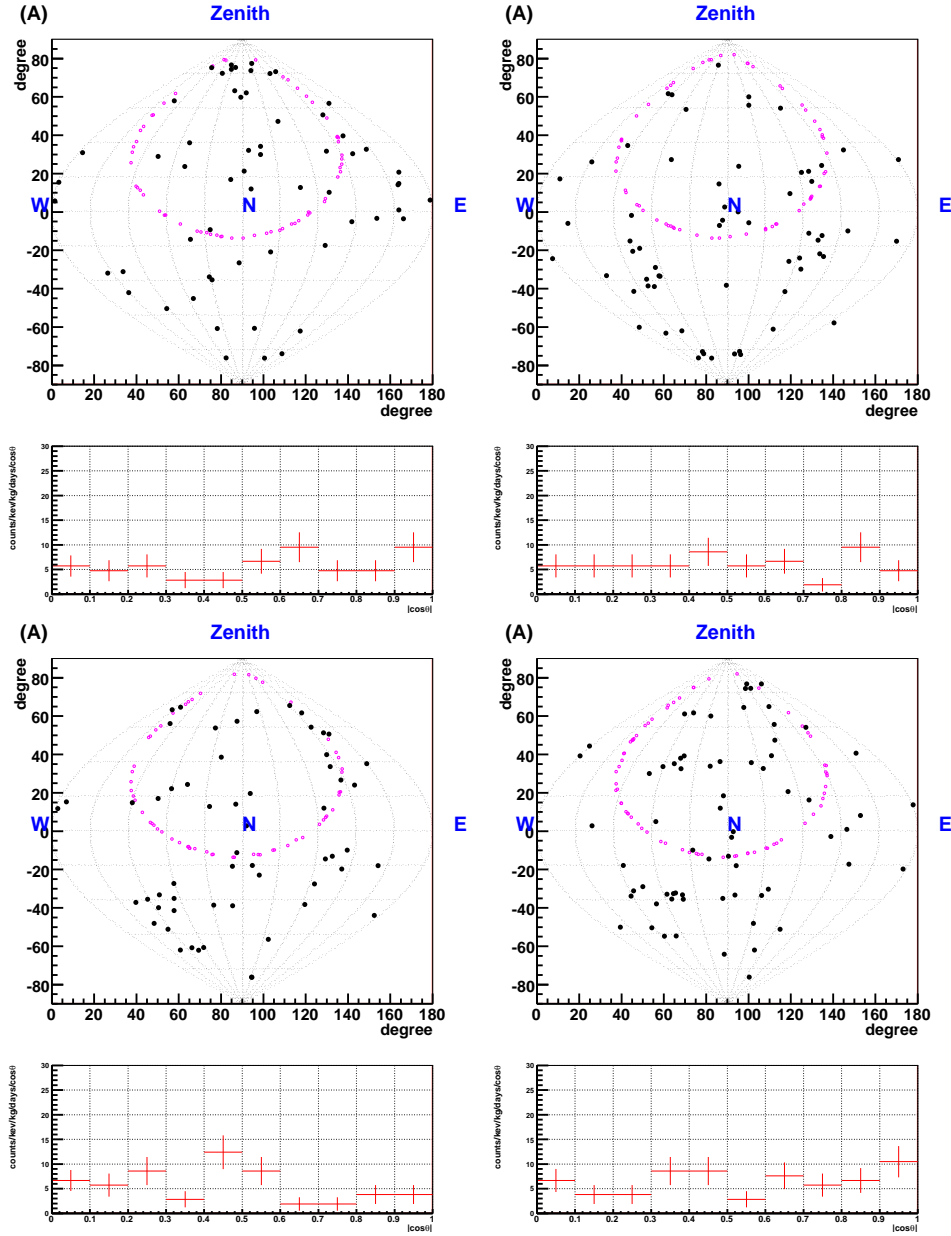
Figure 6.9: The obtained direction of the nuclear tracks plots and $|\cos\theta|$ distributions with energy range of 180-200 keVα.e.(top left), 200-220 keVα.e.(top right), 220-240 keVα.e.(bottom left) and 240-260 keVα.e.(bottom right) in Kamioka RUN-III.
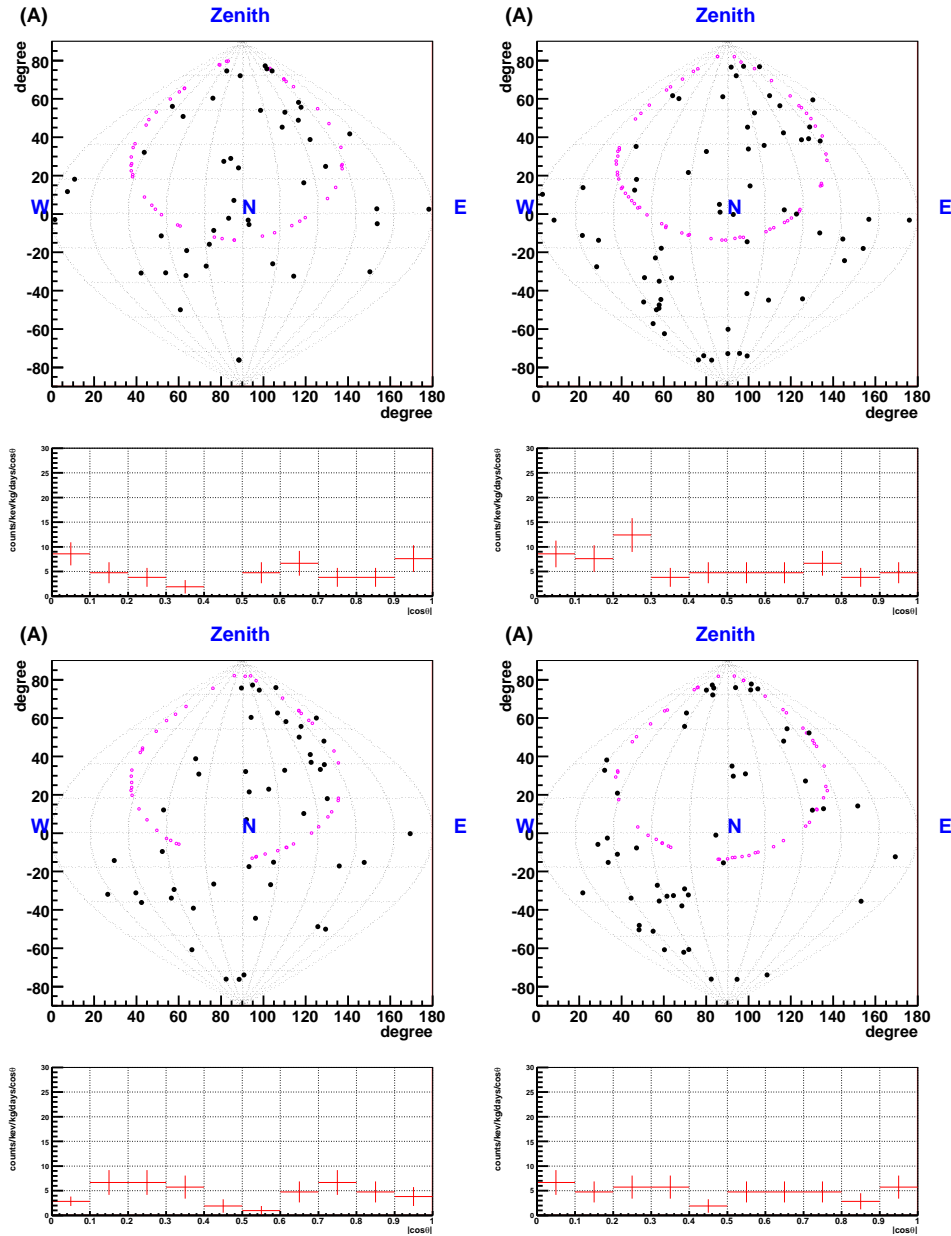
Figure 6.10:   The obtained direction of the nuclear tracks plots and $|\cos\theta|$ distribution with energy range of 260-280 keVα.e.(top left), 280-300 keVα.e.(top right), 300-320 keVα.e.(bottom left) and 320-340 keVα.e. (bottom right) in Kamioka RUN-III.

114
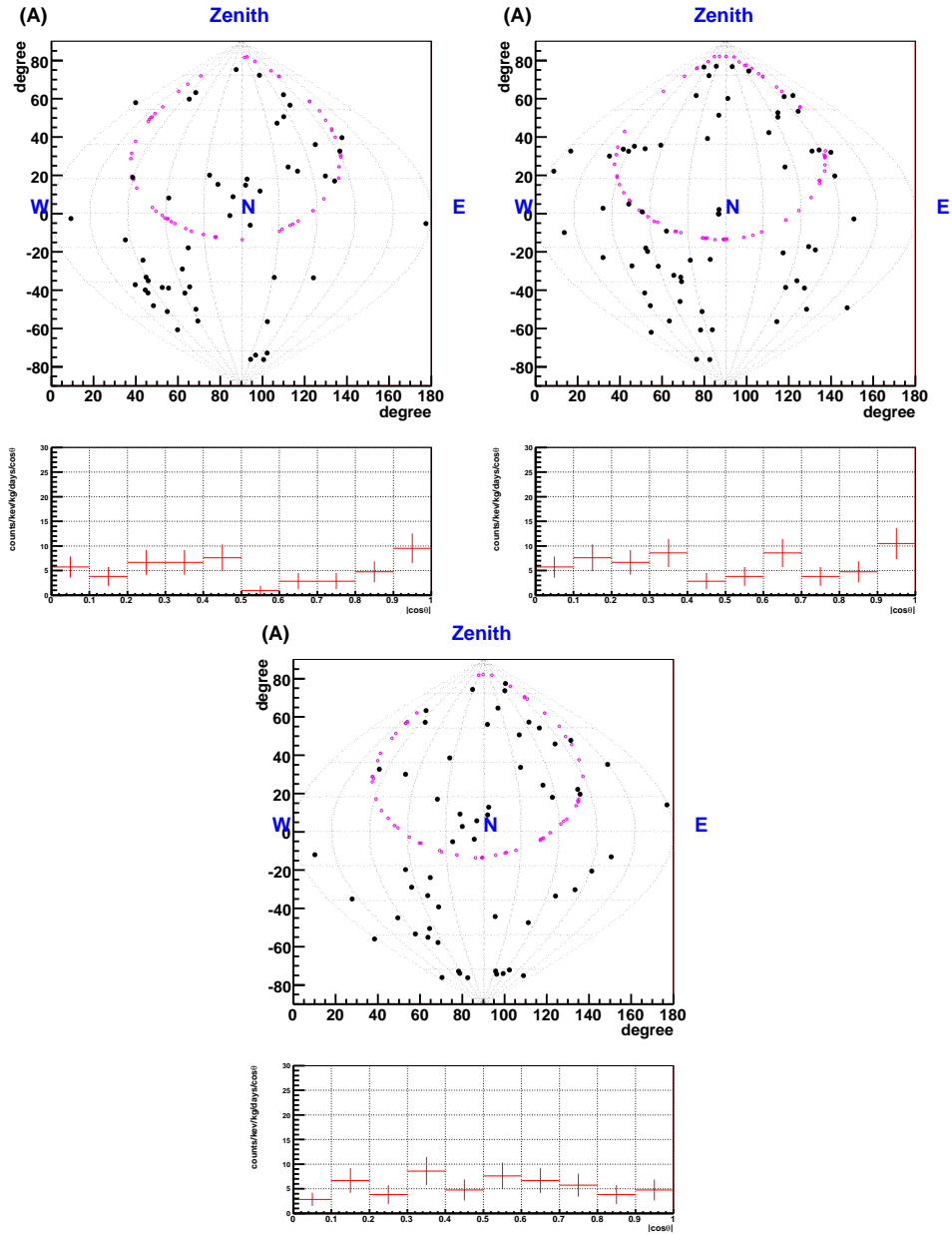
Figure 6.11: The obtained direction of the nuclear tracks plots and $|\cos\theta|$ distributions with energy range of 340-360 keVα.e.(top left), 360-380 keVα.e.(top right) and 380-400 keVα.e.(bottom)

6.2 Dark matter limits by a conventional method

WIMP velocity distribution	Maxwellian
Solar velocity	$v_s = 244 \mathrm{kms}^{-1}$
Maxwellian velocity dispersion	$v_0 = 220 \mathrm{kms}^{-1}$
Escape velocity	$v_{\mathrm{esc}} = 650 \mathrm{kms}^{-1}$
Local halo density	$0.3 \mathrm{GeVcm}^{-3}$
Spin factor of $^{19}\mathrm{F}$	$\lambda^2 J(J+1) = 0.647$
energy resolution at 100 keVα.e.	70%(FWHM)

Table 6.3: Astrophysical and nuclear parameters used to derive the WIMP-proton limit

We derived the limits of the WIMP-proton SD cross section only from the spectrum shown in Figure 6.5 (conventional method). We calculated the expected spectrum of the WIMPs as following. We used astrophysical and nuclear parameters given in Table 6.3, and followed Chapter 2. A spectrum of $^{19}\mathrm{F}$ recoil by WIMP via SD-interactions was calculated for each WIMP mass as shown in Figure 2.9. We then took account of the mass fraction of fluorine nuclei in CF_4 gas. We also then converted energy scale from keV to keVα. e. using the quenching factor of the fluorine as shown in Figure 4.11. The expected spectrum of SD interaction of WIMPs was derived by considering the detection efficiency of nuclear recoil and the energy resolution. Expected spectra for WIMPs masses of 50 GeV/c^2, 100 GeV/c^2, and 500 GeV/c^2, with WIMP-proton SD cross section of 1.0 pb are shown in Figure 6.12. We then conservatively assumed that all the remaining events were caused by the WIMPs, and the limit of $\sigma_{\chi-\mathrm{N}}$ was calculated by comparing these remaining events with the expected dark matter signal. We compared the measured spectrum with the expected ones by the same manner used in[89] and derived the limit for a given WIMP mass. WIMP-proton SD cross section limits are shown in Figure 6.16 by a blue thick dotted line. The upper limit of $\sigma = 8.7 \times 10^3$pb for WIMP mass of 180 GeV/c^2 was obtained from the analysis with the spectrum information only.

6.3 Dark matter search by a direction-sensitive method

We next analyzed the data of Kamioka RUN-III by a direction-sensitive method. We performed the direction-sensitive analysis to compare the measured $|\cos\theta|$ distribution with that expected in the WIMP SD interactions for given WIMPs masses. The expected $|\cos\theta|$ distribution is obtained from the expected recoil angle-energy distribution without the detector responses shown in Figure 2.14. We also used the astrophysical and nuclear parameters given in Table 6.3. We simulated WIMP-nucleus scattering events using the recoil angle-energy distribution, then make the $|\cos\theta|$ distributions for some detected energy bins, taking account the detector response as following procedure.

STEP 1: We prepared the distribution of Figure 2.14 and 15 $|\cos\theta|$ histograms for 15 energy bins The energy of 100-400 keVα.e. was divided into 15 bins.

STEP 2: We simulated a WIMP-nucleus scattering event for the given WIMP mass and the given Cygnus direction. A recoil angle θ_{R} and a recoil energy E_{R} keV were given from the distribution of Figure 2.14. The azimuth angle, ϕ_R, was given randomly from a flat distribution.

STEP 3: The unit of the recoil energy (E_{R} keV) was converted to keVα.e. using the quenching factor. The detection efficiency and the mass fraction of fluorine nuclei in CF_4 were
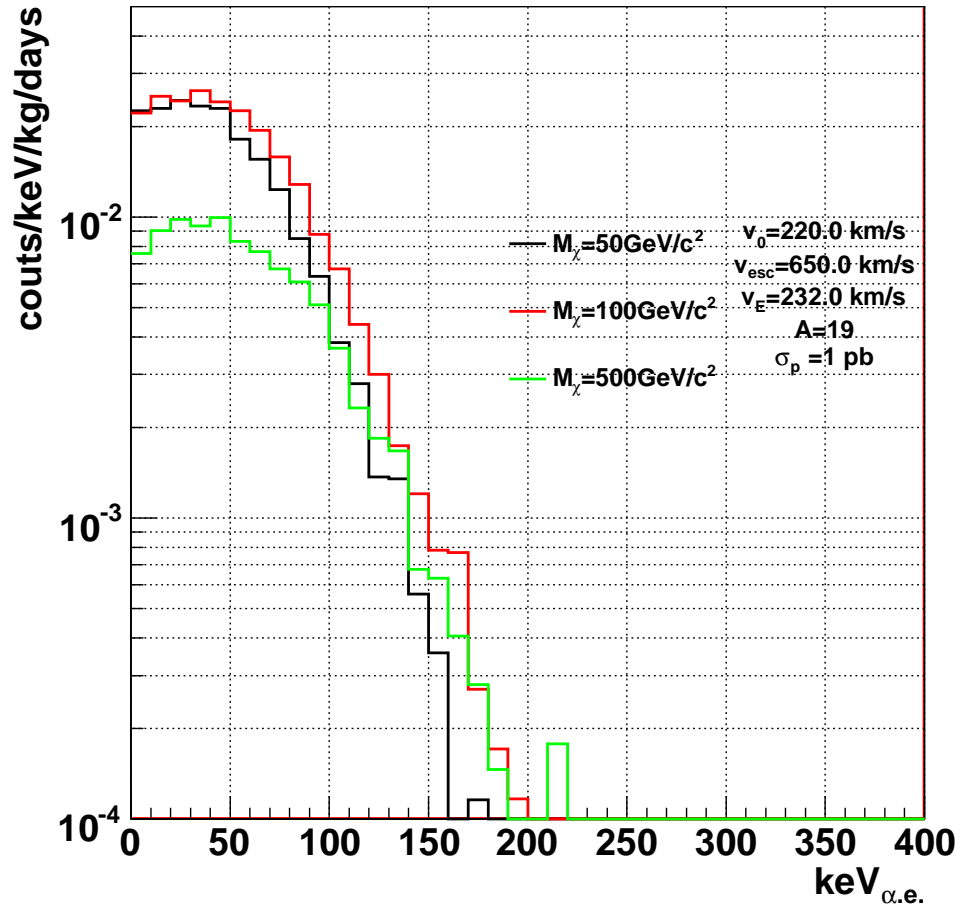
Figure 6.12: Expected energy spectra for the SD interaction of WIMPs in CF_4 with a $\sigma_{\chi-p} = 1$pb. Energy resolutions, quenching factors, and nuclear detection efficiencies are taken into account. Black, red, and green lines show the cases of M_χ=50, 100 and 500 GeV/c^2, respectively.

merged and applied as a directional independent efficiency ϵ. The energy fluctuation due to energy resolution was taken account of. Detected energy was expressed as E'_RkeVα.e.

STEP 4: We calculated the recoil vector, $\mathbf{e}_R$, in the detector coordinate from the Cygnus direction, $\mathbf{e}_C$, and the recoil angle, θ_R and ϕ_R. The *directional-dependent efficiency* $\eta(\mathbf{e}_R)$ was applied for $\mathbf{e}_R$ from Figure 4.22. The angular resolution was taken account for $\mathbf{e}_R$ with the two-dimensional gaussian. A vector, $\mathbf{e}_{\text{det}}$, was obtained as a detected direction.

STEP 5: $|\cos\theta_{\text{det}}| = |\mathbf{e}_{\text{det}} \cdot \mathbf{e}_C|$ was calculated. We filled a value of $|\cos\theta_{\text{det}}|$ into each $|\cos\theta|$ histogram for each obtained energy E'_R with a weight of the $\eta \times \epsilon$.

STEP 6: We repeated from STEP 2 to STEP 5 for many Cygnus directions to simulate the daily modulation.

STEP 7: We repeated from STEP 1 to STEP 6 for some WIMPs masses.

The calculated distributions by this procedure for some energy ranges and some WIMP masses are shown in Figure 6.13 and Figure 6.14, respectively.
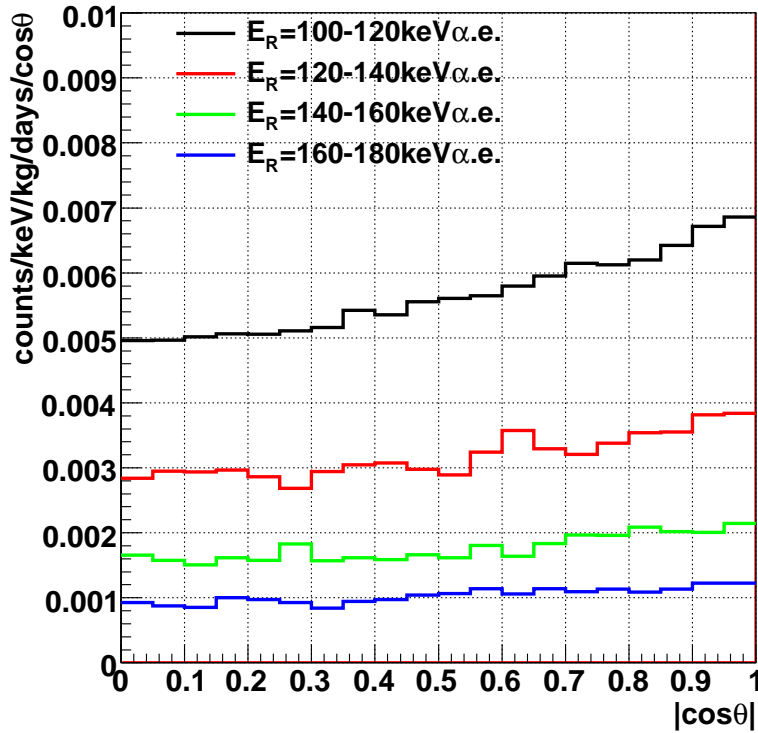
Figure 6.13: Expected $|\cos\theta|$ distributions for some recoil energies (black 100-120keVα.e., red 120-140keVα.e., green 140-160keVα.e., blue 160-180keVα.e.). We assumed the SD cross section of 1pb, WIMP mass of 100GeV/c^2, the tracking angular resolution of 55°(RMS), the energy resolution of 70%(FWHM) and "*directional dependent efficiency* " (Figure 4.21).
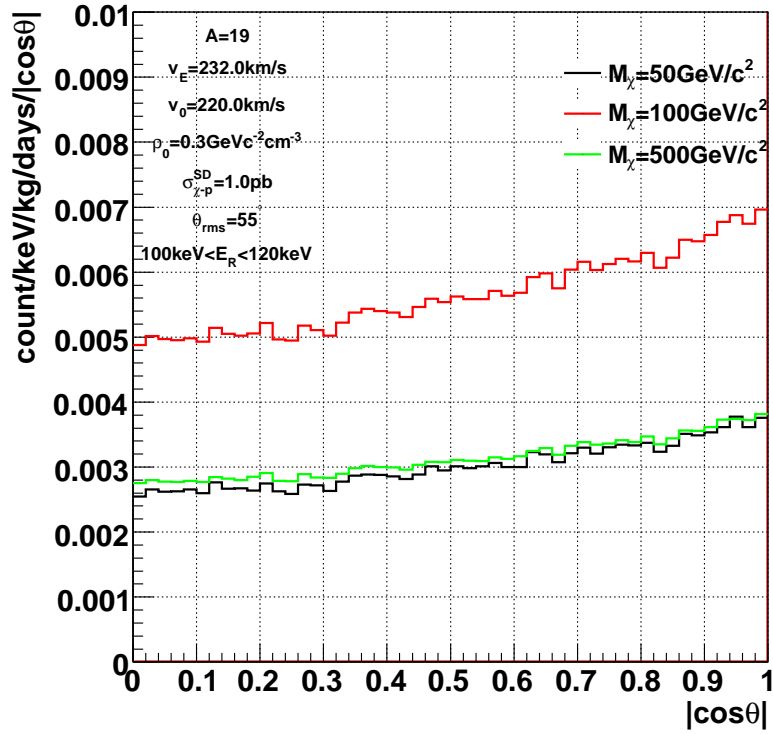
Figure 6.14: Calculated $|\cos\theta|$ distributions for the SD cross section of 1pb and WIMP masses of 50, 100, 500 GeVc^{-2}, where the tracking angular resolution of 55°, energy resolution of 70%(FWHM) and the direction dependent nuclear detection efficiencies(Figure 4.21) were considered. The histograms for the masses of 50 GeV/c^2 and of 500 GeV/c^2 are similar because count rates of them are nearly same in a range of 100-120 keVα.e. in Figure 6.12.

We then compared the measured $|\cos\theta|$ distribution of Kamioka RUN-III with these expected WIMP $|\cos\theta|$ distributions and the flat background model to the measured and drew the limit line for the SD WIMP-proton cross section. We rebined the $|\cos\theta|$ histograms into two bins because the measured distributions shown in from Figure 6.8 to Figure 6.11 has a poor statistics. We fitted the measured distribution with the calculated distributions with the cross section as a free parameter. Figure 6.15 shows the rebined histogram and the best-fit distribution calculated for $M_\chi = 100$GeV and 100-120 keVα.e. bin, The cross section that gave the minimum χ^2 was 5.5×10^3pb, where χ^2/d.o.f.=3.71/1. This best fitted
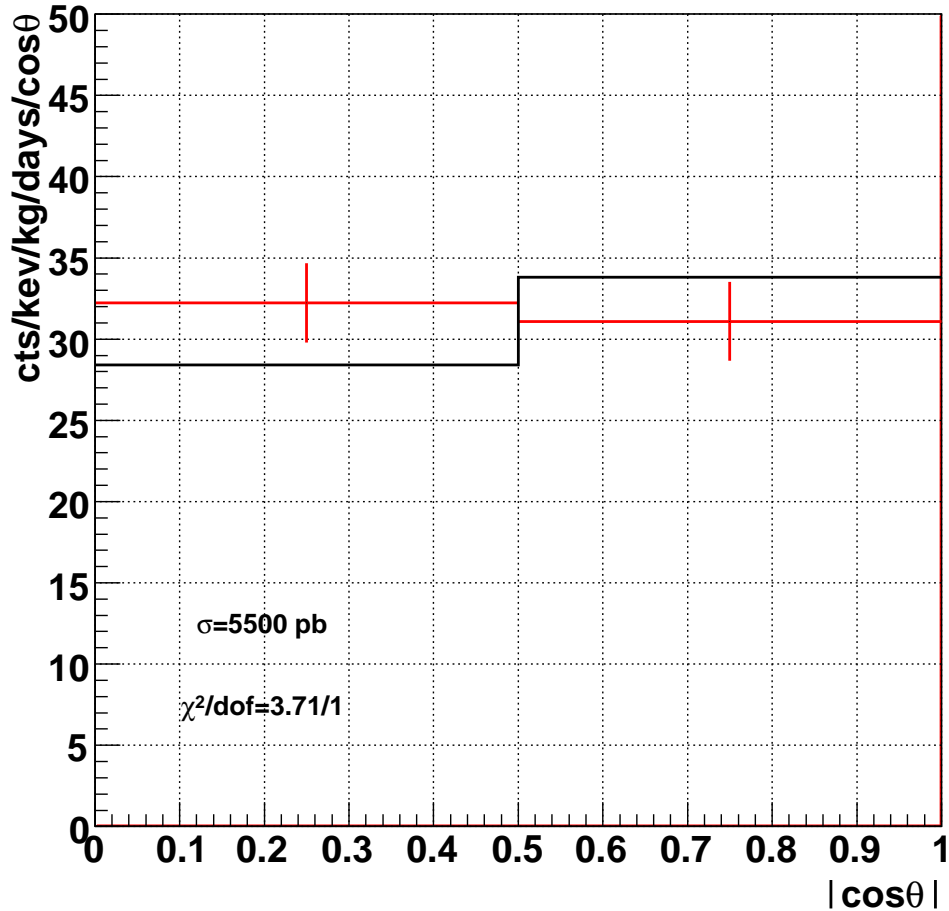
Figure 6.15: Measured $|\cos\theta|$ distributions of Kamioka RUN-III in the energy range of 100-120 keVα.e. and expected $|\cos\theta|$ distribution with a cross section of 5.5×10^3pb and WIMP mass of 100 GeVc^{-2}.

WIMP signal was rejected at the 90% confidence level by the χ^2 test. We also fitted the measured distribution with the flat background model, where we assume all events were due to an isotropic background. The fitting result gave χ^2/d.o.f. $= 0.110/1$ independent of the WIMP mass and the flat background model was not rejected at the 90% confidence level.

We then tested for other WIMP masses by the same manner. The cross section that would give the minimum χ^2 was calculated and the smallest cross section was taken as the limit for the given WIMP mass. The WIMP-wind model was rejected at a 90% confidence level for all the masses from 30 GeV/c^2 to 1000 GeV/c^2, while the flat background model was independent of the WIMP mass. The limits are shown with a thick-solid line (labeled "direction-sensitive") in Figure 6.16. Calculated values of minimum χ^2 with the WIMP model, and with the flat background model are shown as black, and blue points, respectively, in Figure 6.17. All black points are above 90% C.L. line. We obtained a 90% C.L. SD WIMP-proton limit of 5.4×10^3pb for WIMP with a mass of 150 GeV/c^2. This result marked new best sensitivity record for a SD WIMP search with the direction sensitive method, although its sensitivity was still far worse than that of the frontier of SD WIMP searches with other methods.

SD 90% C.L. upper limits and allowed region
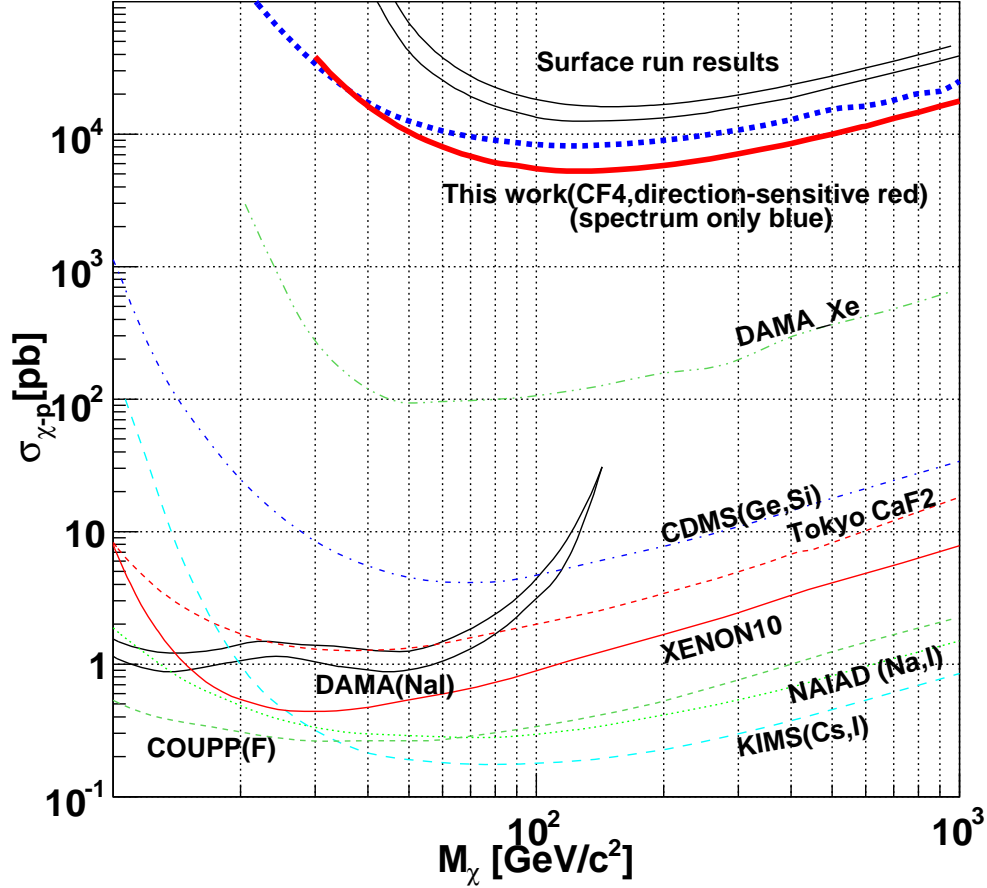
Figure 6.16: Limits of SD cross section, $\sigma_{\chi-\mathrm{p}}^{\mathrm{SD}}$, as a function of M_χ. The regions above the curves are excluded. A blue thick dotted line is a result of conventional method and a red thick solid line is a result of directional-sensitive method in this work. We obtained a 90% C.L. limit of 5.5×10^3pb for WIMP with a mass of 100 GeV/c^2. Two black lines labeled "Surface run result" are shown surface run results by the conventional methode (upper) and by the directional methode (lower). Allowed region(DAMA(NaI)[45]) and limits of other experiments (DAMA(Xe)[60], CDMS[56], Tokyo[49], NAIAD[47], KIMS[48], XENON10[64],COUPP[69]) are shown for comparison.
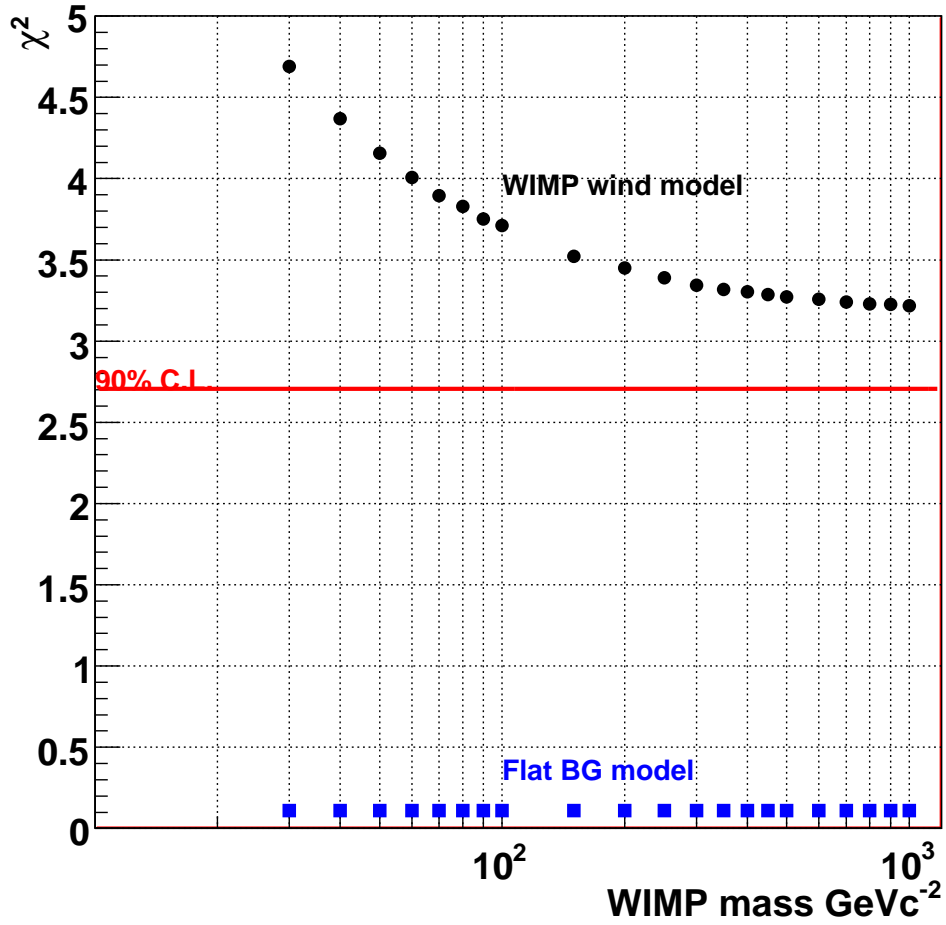
Figure 6.17: Minimum χ^2 values for some WIMP masses. Measured $|\cos\theta|$ distribution was fitted with expected distributions of the WIMP wind model (black circle) and the flat background model (blue square).

Chapter 7

Discussion

We performed a dark matter search in Kamioka mine with the NEWAGE-0.3a detector. Finally we set stricter upper limit for the WIMP-proton SD interaction than that of the surface run. However, there were some issues to resolve in order to search the WIMP-wind in the MSSM region.

In this chapter we discuss the remaining backgroud in Kamioka RUN-III and list the issues to imorove for the WIMP-wind search.

7.1   Remaining background

Although the background count rate in Kamioka RUN-III was about 1/3 of that in Kamioka RUN-I at 100 keVα.e. as shown in Figure 6.6, there still remained so many events which restricted the detector sensitivity for WIMP. We applied the discussions in Section 5.6 to the measured spectrum in Kamioka RUN-III. Figure 7.1 shows the measured spectrum and estimated spectra where we assumed ^{222}Rn density of 3.8×10^{-15}g/g (black solid and dotted lines) , calculated ambient gamma-ray contribution (solid gree line), ^{238}U density in the GEM of 4.0×10^{-6}g/g (blue lines), and other contribution are ignored. Those conditions are as same as in Figure 5.27, but the suppression factor was double of that in the previous discussion.

We succeed reducing backgound count rate at 100 keVα.e. by increasing the surpression factor in the gap region. We found that contributions of tha gap region between the μ-PIC and the GEM (the Ⓒ-④ and the Ⓓ-④ categolized in Table 5.4) were the most dominant component of the measured spectrum at 100 keV in Kamioka RUN-I, and could be still in Kamioka RUN-III.

7.2   Future work

The upper limit was restricted by the statistical error of background events in this work. Although this statistical error will decrease with longer operation, a prospect of the sensitivity with a exposure of 3kg·year is far away from even the DAMA region, not to say the MSSM region($< 10^{-3}$pb) (Figure 7.2). We need an exposure of 3000 kg·year to reach the DAMA region assuming zero systematic errors, however it is not a reasonable experiment to realize. So we propose to improve the following points of the NEWAGE-0.3a detector.

- Background rejection

- Improvement of the angular resolution
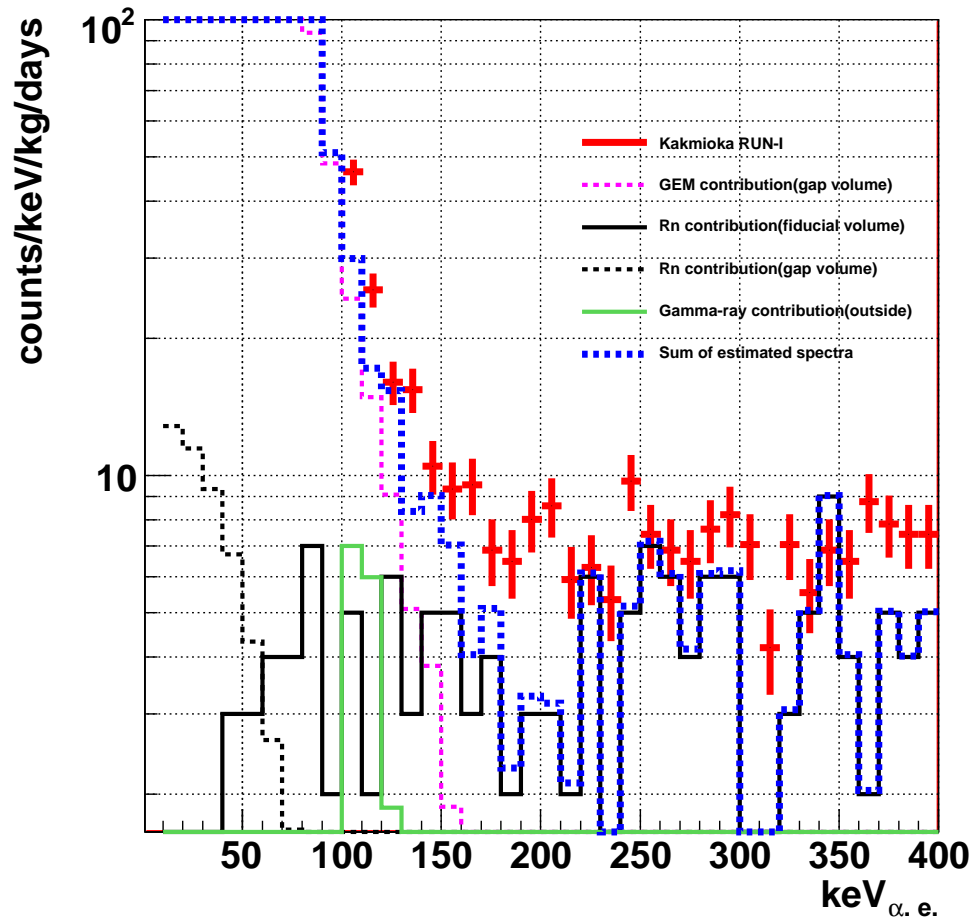
Figure 7.1: Measured spectrum in Kamioka RUN-III and estimated spectra.

SD Prospct Sensitivity
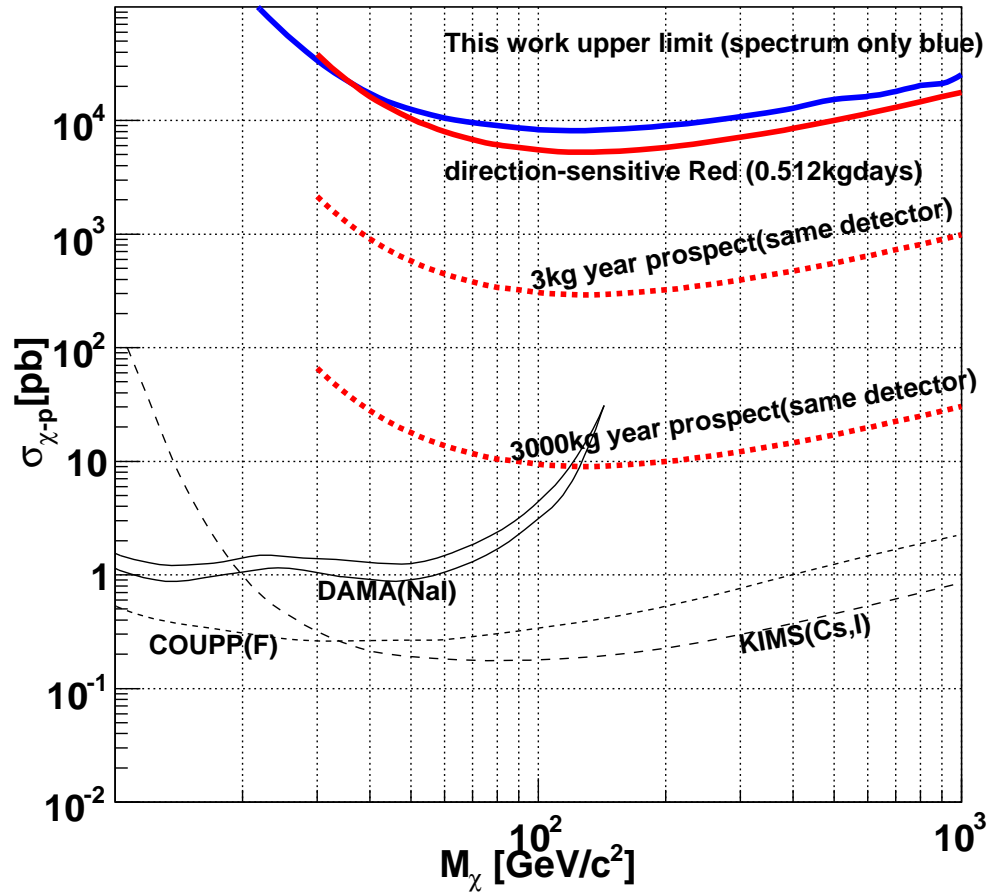
Figure 7.2: Prospect sensitivity of the NEWAGE-0.3a detector with the same performance and condition of this work for larger exposure operations.

- Lowering the threshold

We discuss each improvement plan in this section.

7.2.1 Background rejection

Dominant source of background events seemed to be α -particles in the μ-PIC-GEM gap ($\sim$30 counts/keV/kg/days), α -particles from ^{222}Rn and ^{220}Rn progeny ($\sim$5 counts/keV/kg/days), and ambient γ-rays($\sim$5 counts/keV/kg/days) although there still remain uncertainty factors. We have already found that the effect of the α-particles in the μ-PIC-GEM gap can be suppressed by high gain GEM operations. Operations with an even higher gains should be realized with a slight increase of possibilities of damaging the GEM. The background level due to the gap events should be reduced by a factor of 100 in these higher-gain operations. In addition to the gain control, we need to develop low radioactive-impurity μ-PICs and GEMs.

We have a plan to decrease α-particles from ^{222}Rn and ^{220}Rn progeny by eliminating radon gas with a charcoal filter. A circulating system for the purification with a charcoal filter will be reduce radons and the background event due to radons.

Misidentifications of γ-rays are not also negligible as shown in Section 5.3. We have to improve the γ-ray rejection power. Causes of misidentification are bad energy resolution and a bad tracking performance for electron tracks. They cause a bad dE/dx resolutions and thus as insufficient γ-ray discrimination power. New tracking FPGA codes which have potentials to detect more detail a shape of electron clouds are ready to improve the tracking performancs. This improvement also should be effective against muon background events.

As a result, we found that reducing the radio-impurites in the chamber and the improvement of the tracking performance of μ-TPC are equally important. With these efforts, we should achieve the background level $O(10^{-1}$ count/keV/kg/day), where an ambient neutron flux will dominate the background. Then we can reduce the neutron background by covering the detector with appropriate shieldings (water or polyethylene) another order of magnitude. The sensitivities should be improved by a factor of at least 100 when the background level is $O(10^{-2}$ count/keV/kg/day).

7.2.2 Improvement of the angular resolution

Angular resolution affect the sensitivities largely in a direction-sensitive dark matter search. Bad angular resolution decrease the characteristic excess around $\cos\theta = 1$ in the $|\cos\theta|$ distribution as shown in Figure 4.23 and thus the sensitivity for the dark matter interaction is worsened. Table 7.1 describes required signal-to-noise ratios (S/N) to reject the flat background model with a 90% C.L. for the calculated $|\cos\theta|$ distributions. The NEWAGE-

angular resolution	required S/N with $|\cos\theta|$	required S/N with $\cos\theta$
$\sigma = 10°$	2.14	1.89
$\sigma = 20°$	2.42	1.95
$\sigma = 30°$	3.37	2.00
$\sigma = 45°$	7.20	2.25
$\sigma = 55°$	14.27	2.65

Table 7.1: Required S/N for detecting dark matter signals in energy rage of 100-120 keV with 90% C.L. for M_χ=100GeV/c^2. We took account the energy resolution, detection efficiency of NEWAGE-0.3a detector and assumed zero background.

0.3a detector has a potential to improve the sensitivity more than 10 times by improving of

the angular resolution. As describe in Section 4.4.3, the angular resolution was restricted by the nuclear track length because the two-dimensional sampling pitch of the μ-PIC (400 μm) and the sampling clock (100 MHz) is not fine enough compared to the track length (ex. 1.1 mm for an 100 keVα.e. for a fluorine nucleus in 152 torr CF_4). We need to operate with lower pressure gas to get a longer nuclear track and higher angular resolution. Since tracking angular resolutions at 600 keVα.e., for which a fluorine nucleus runs 4.5mm, was 35°, the angular resolution should be improve to about 35° at 100 keVα.e. with 40 torr CF_4 gas. In addition, one of the new FPGA code should improve tracking performance for the vertical component against μ-PIC plane, which dominated the angular resolution. Thus angular resolution should be improved better than 30° at 100 keVα.e.

Furthermore, a gas detector with finer pitch than the μ-PIC, should realized much better angular resolution even for lower energy (ex. 50 keVα.e.). A μ-PIC has a potential to be fine as or finer than 300μm although some ptototype tests are needed to make the large size one ($\sim$30$\times$30cm^2).

7.2.3 Lowering the threshold

Since the shape of the dark matter spectrum rises exponentially at low energy as we described in Figure 2.9. We can expect more events with a lower threshold. If the detecor had lower the threshold down to 50 keVα.e., ten times more dark matter events are expected, while the number on neutron background events increases only a foctor of three. The threshold in this work, E_{th}=100keVα.e., was restricted by the efficiencies for nuclear tracks. The efficiencies near the energy threshold are restricted by the track length as we described in Section 4.4.1. Thus a lower pressure operation also improve the detector threshold. We will try to operate the μ-TPC with 40 torr CF_4 gas to achieve a threshold of 50 keVα.e.

7.2.4 Track-sense measurement

Since we did not measure the track sense; the head and tail of each track, in this work, the sensitivity for the dark matter was worse than a measurement using information of the track sense. If we can measure the track sense, a smaller signal-to-background ratio (S/N) is sufficient discriminate a flat cosθ distribution from dark matter signals than a measurement without sense as shown in Table7.1. The track sense is able to be determined by measuring dE/dx along track precisely. Since energy depositions of a fluorine in CF_4 gas decrease together with neclus energy along its track below 10 MeV, much more energy depositions detected at the tail of track than at the head of track. Figure 7.3 shows the number of produced ion-electron pair in unit length by nuclear recoils as a function of the recoil energy[83].

In fact, DMTPC group observed this effect of a recoil fluorine using gas multiplication mesh and CCD camera in 50 torr CF_4 as shown in Figure 7.4 although only in two-dimention projection plane [74].

In other hand, NEWAGE-0.3a detector need a much higher energy resolution and a much higher position resolution to measure the dE/dx variation along a track. The position resolution improvement is strongly related the improvement of the tracking angular resolution. Now it is studied that the methode to achieve much more performancis in this point.

7.2.5 Future of the NEWAGE

If we could achieve to reduce the background ($O(10^{-2})$), to improve the angular resolution ($\sim$ 30°) and to operate with lower threshold ($\sim$ 50 keVα.e.), (they should be realized with our current technology), we would get 10^3 times better sensitivity. Expected sensitivity
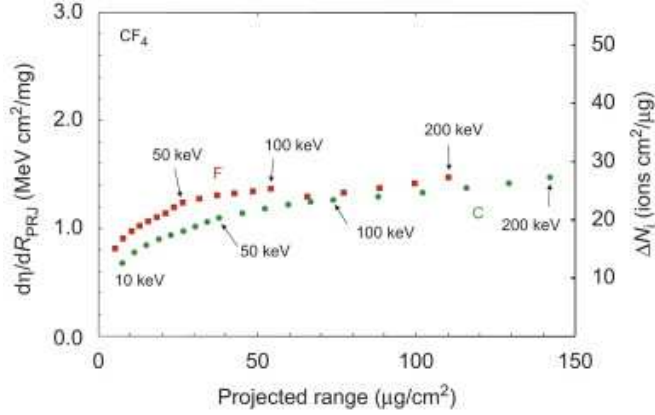
Figure 7.3: The Bragg-like curve estimated for recoil C and F ions in CF4. The area below each curve expresses the number of ions produced [83].

with this improved detector are shown in Figure 7.5. We should achieve a sensitivity of $\sigma_{\chi-p}$=1.5 pb for the dark matter mass of 100 GeV/c^2, which is the current frontier for the SD interaction search, with a exposure of 30 kg·year. Construction of the CF$_4$ detector with total mass of $O(10\text{kg})$, which needs $O(100\text{m}^3)$ fiducial volume with a pressure of 40 torr, is not impossible.

Furthermore, if we realize much lower threshold ($\sim$ 30 keVα.e.), much better angular resolution ($\sim$ 10°), and the measurement of the track sense with some technical improvements, we will get 10^2 much better sensitivity and achieve to search the MSSM regions as green lines in Figure 7.5 are shown.
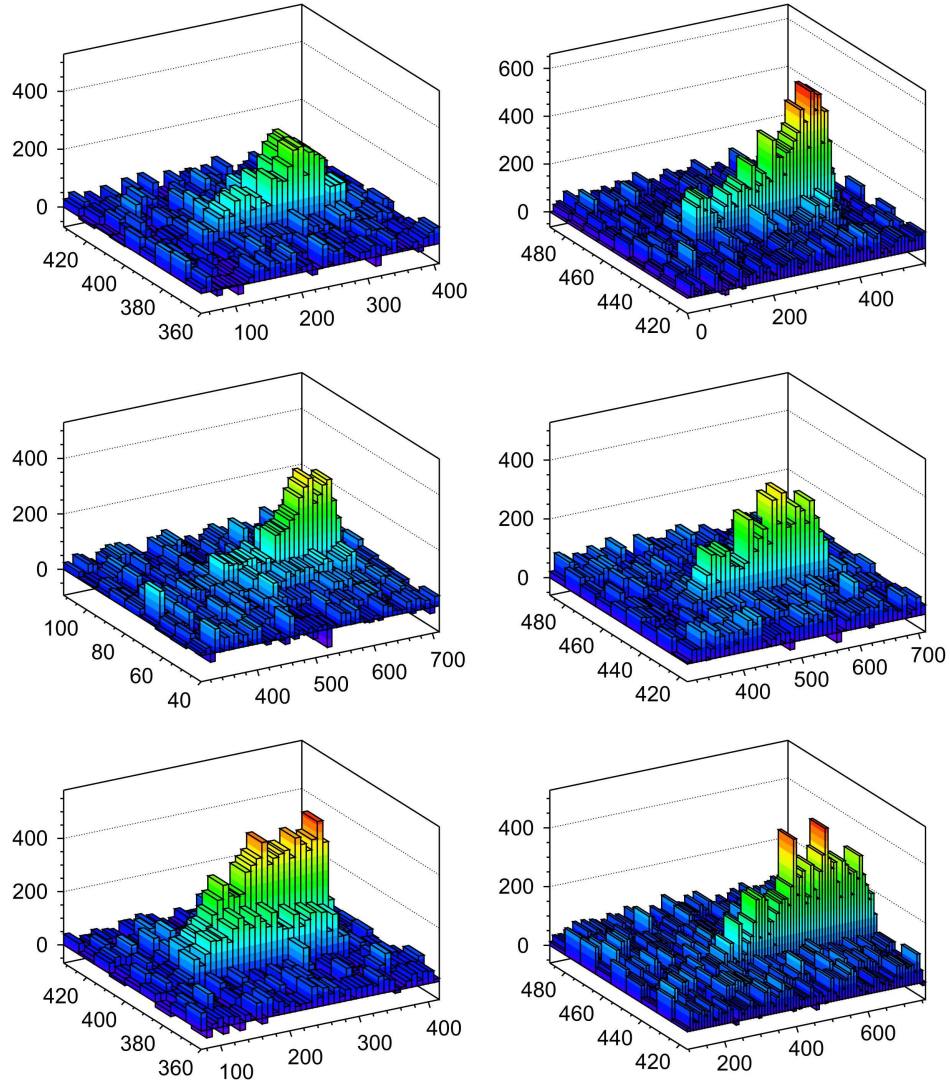
Figure 7.4: Images of recoil tracks reported by the DM-TPC group [74]. The figure show the CCD coordinates and pixel intensity. In all images neutrons are coming from the right. Images in the right column have the wire planes rotated by 180° operator. The noticeable asymmetry of the light yield along the wire indicates observation of the head-tail effect [74].

SD Prospct Sensitivity
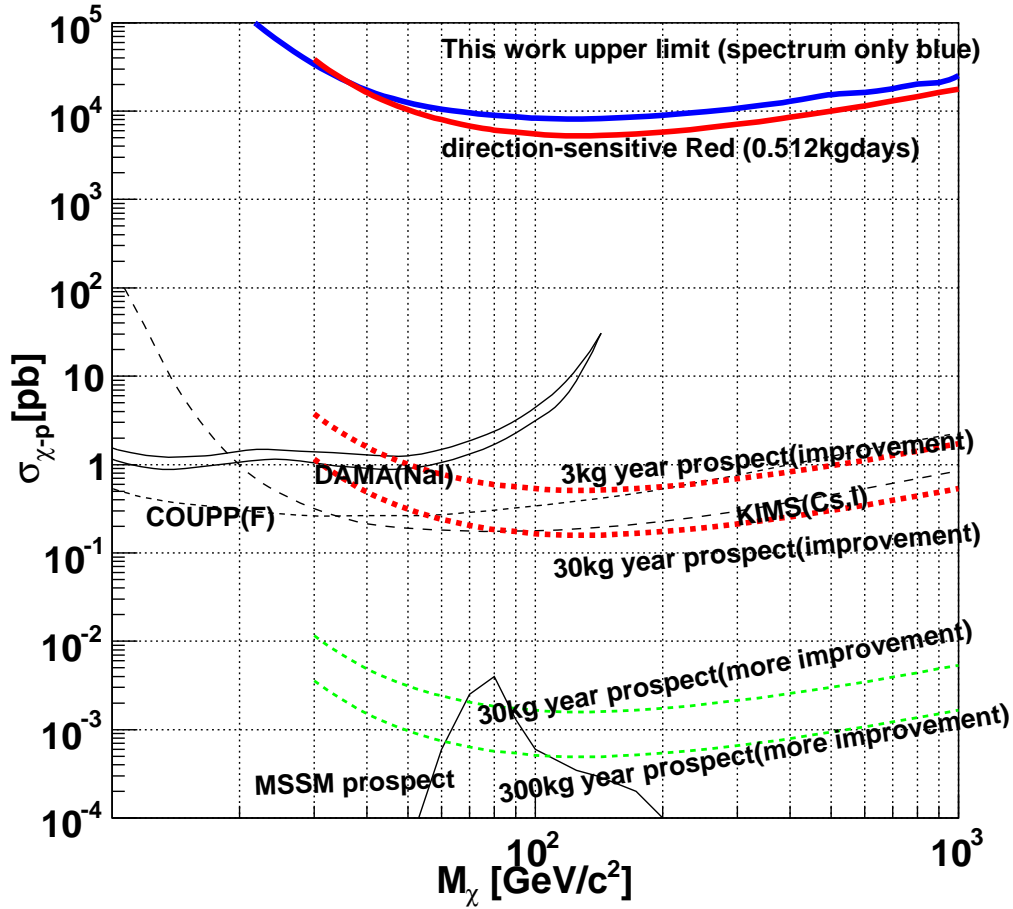
Figure 7.5: Prospect sensitivities of NEWAGE with current technical improvement (red dotted lines) and with next technical improvement (green dotted lines). "Current technical improvement" means 50 keVα.e. energy threshold, 30° angular resolution, 10^{-2} counts/keV/kg/days background level, and analysis without the track sense. "Next technical improvement" means 30 keVα.e. energy threshold, 10° angular resolution and analysis with the track sense. Black lines labeled "MSSM prospect" is a region predicted by the MSSM.

Chapter 8

Conclusion

In this thesis, we proposed the NEWAGE experiment for a direction sensitive dark matter search and developed a prototype detector (the NEWAGE-0.3a). We measured the performance of the NEWAGE-0.3a detector and operated it in Kamioka mine. In the first operation (Kamioka RUN-I), we found there were some unknown background origins other than the ambient neutron. We studied and estimated these unknown background origins from the data of Kamioka RUN-I and Kamioka RUN-II. Based on these background studies, the operation parameter of the NEWAGE-0.3a detector was optimized.

A dark matter search was performed with the optimized NEWAGE-0.3a detector. In this dark matter search run, we obtained a 90% C.L. spin-dependent WIMP-proton limit of 5.4×10^3pb for WIMP with a mass of 150 GeV/c^2 and 8.7×10^3pb for WIMP with a mass of 180 GeV/c^2 in the direction-sensitive and the conventional analysis method, respectively. This directional result marked the new best sensitivity record for a SD WIMP search with the direction sensitive method, although its sensitivity was still far worse than those of the frontier of SD WIMP searches with other methods. A directional sensitive dark matter search with some technical improvements and 30kg·year exposure will reach to the MSSM predict region.

Chapter 9

Acknowledgments

Appendix A

Radioactive isotpes in materials

We introduce major natural radioactive isotopes in this chapter. Most of data shown in this Chapter based on [90].

A.1 ^{238}U-chain

^{238}U has a long half life of $4,468 \times 10^9$ year, and it continuously decays into a stable nucleus, ^{206}Pb, as shown in Figure A.1. γ-rays emitted in this chain are shown in Figure A.2.

A.2 ^{232}Th-chain

^{232}Th has a longer half life than one of ^{238}U, 1.405×10^{10} year, and it continuously decays into a stable nucleus, ^{208}Pb, as shown in Figure A.3. γ-ray emitted in this chain are shown in Figure A.4

A.3 ^{40}K

The natural abundance of ^{40}K, is 0.0117%. ^{40}K has a lifetime of 1.27×10^9 years. ^{40}K decays with a β-decay (89.3%) or with an electron capture $\beta^+ + e^-$ (10.7%). The γ-ray with an energy of 1460.8 keV is emitted as a result of the electron capture.

$_{92}$U

^{238}U
4.468×10^{9} y

^{234}U
2.457×10^{5} y

β 2.269
(99.2%)

^{234}Pa
1.17 m

(0.16%)

β 0.472
(γ)

$_{91}$Pa

α
4.198

^{234}Pa
6.75 h

β 0.472
(γ)

α
4.775
(γ)

$_{90}$Th

^{234}Th
24.10 d

β 0.196
(γ)

^{230}Th
7.538×10^{4} y

$_{89}$Ac

α
4.687
(γ)

$_{88}$Ra

^{226}Ra
1.600×10^{3} y

$_{87}$Fr

α 4.784
γ 0.186

$_{86}$Rn

^{222}Rn
3.824 d

$_{85}$At

α
5.490
(γ)

^{218}At
1.5 s

$_{84}$Po

(0.02%)
^{218}Po
3.10 m
(99.98%)

β

α
6.694

^{214}Po
164.3 μs

^{210}Po
(RaF)
138.4 d

$_{83}$Bi

α
6.003

(99.98%)
^{214}Bi
19.9 m
(0.02%)

β 1.07
1.51
3.27

α
7.687
(γ)

(99+%)
^{210}Bi
(RaE)
5.013 d
$(1.3\times10^{-3}\%)$

β 1.16

α
5.304
(γ)

$_{82}$Pb

^{214}Pb
26.8 m

β
0.67
0.73

α 5.450
(γ)

(99+%)
^{210}Pb
(RaD)
22.3 y
$(1.9\times10^{-6}\%)$

β 0.0170
γ
0.0465

^{206}Pb
stable

$_{81}$Tl

^{210}Tl
1.30 m

α

^{206}Tl
4.199 m

β 1.53

$_{80}$Hg

^{206}Hg
8.15 m

β, γ

Figure A.1: Decay scheme of the uranium chain
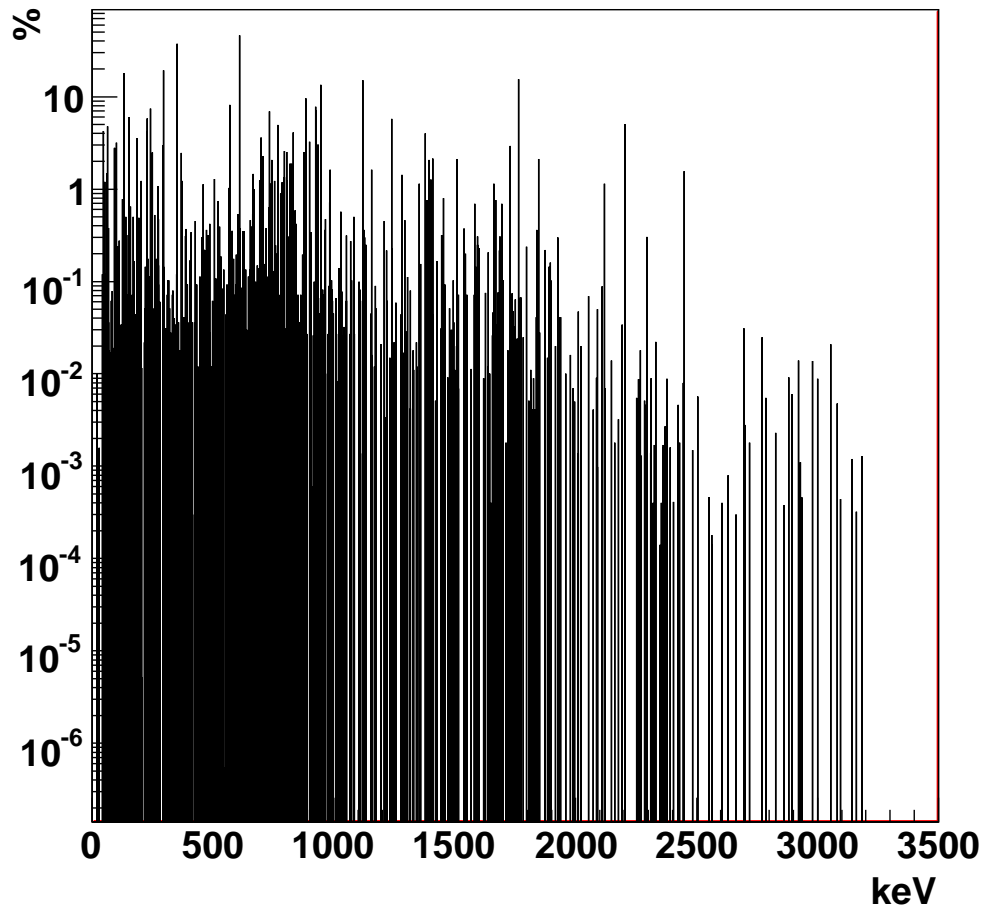
Figure A.2: Gamma rays emitted in the U-chain.
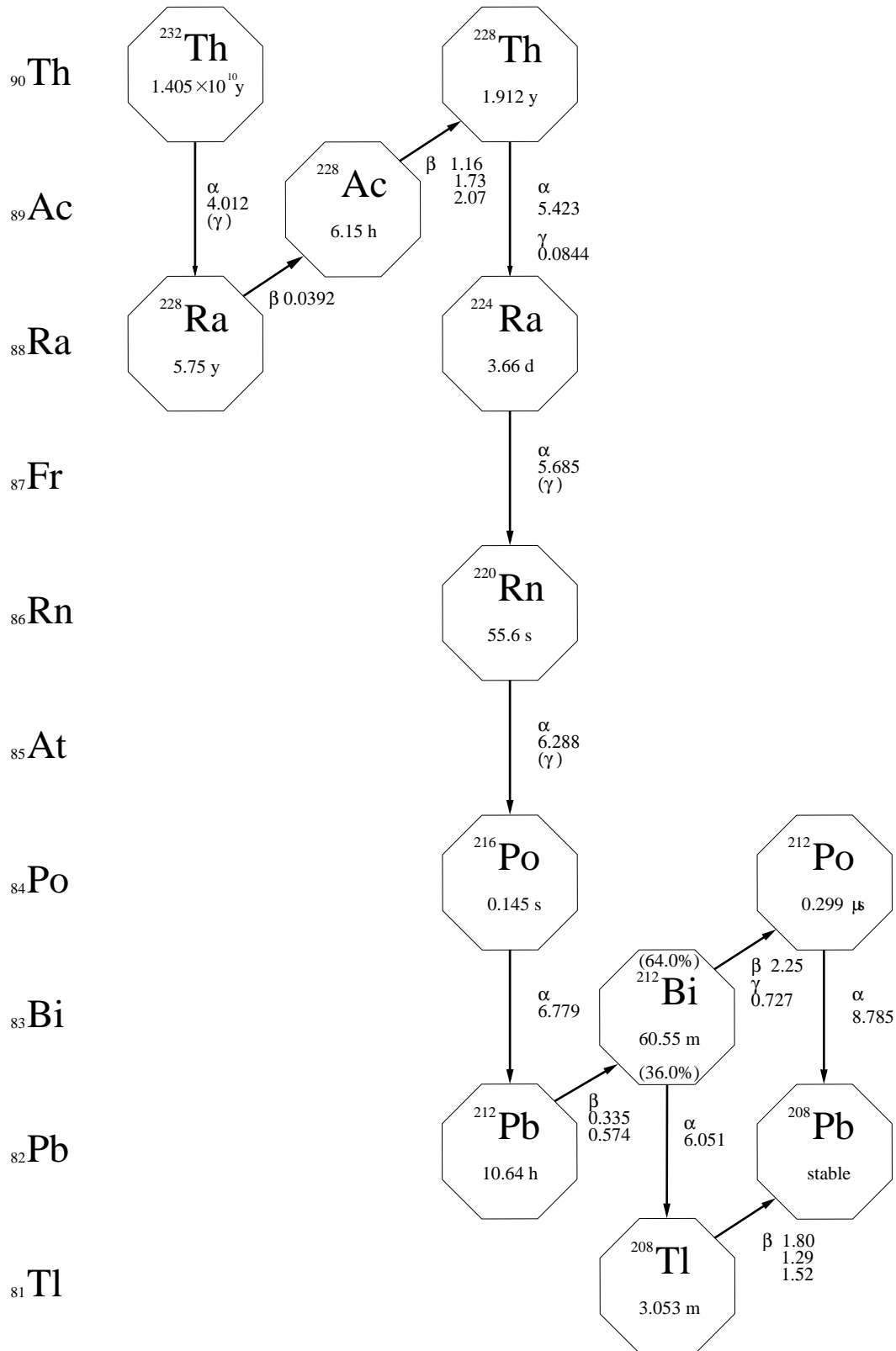
Figure A.3: Decay scheme of the thorium chain
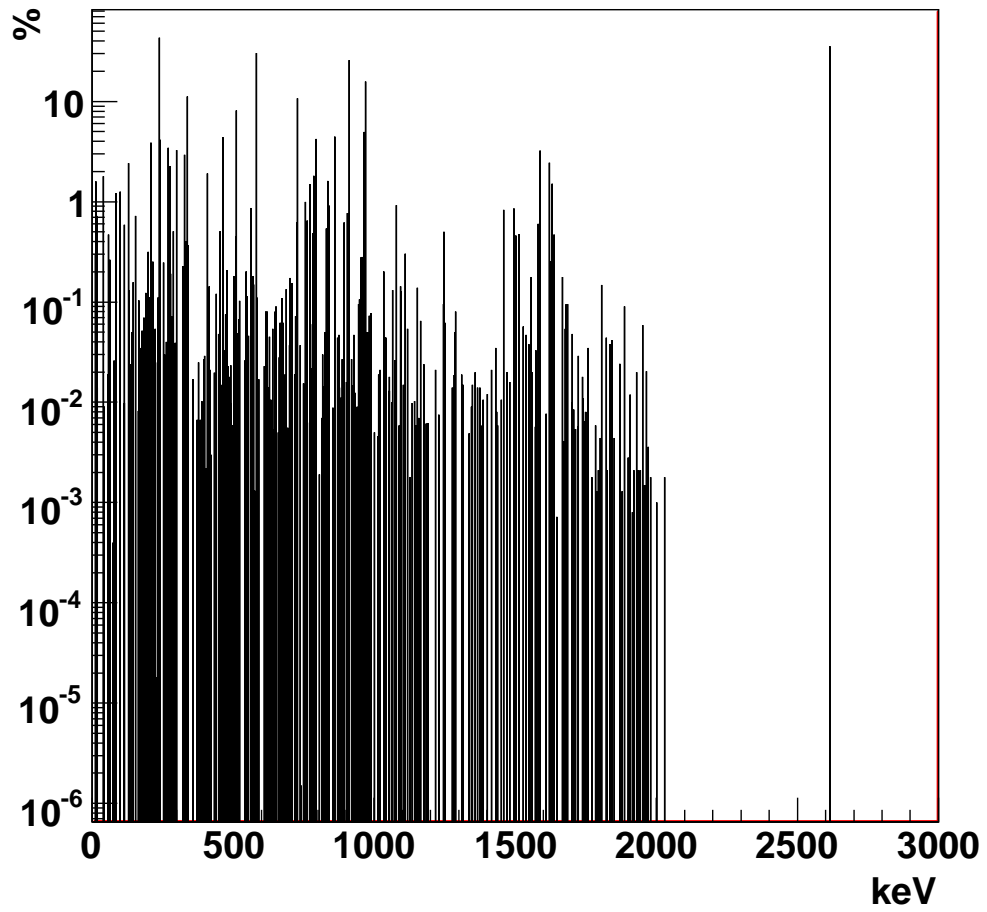
Figure A.4: Gamma rays emitted in the Th-chain.

Appendix B

μ-PICs and μ-TPC

A Micro Pixel Chamber(μ-PIC) was used in the NEWAGE-0.3a detector as a main gas-amplifier and a fine pitch read-out detector. In this chapter we introduce fundamental performances of the μ-PIC and the μ-TPC (micro-Time Projection Chamber).

B.1 μ-PIC

μ-PIC is a two-dimensional gaseous detector which has 256×256 pixels with a pitch of 400 μm in an area of 10×10 cm^2 [91], [92], or 768×768 pixels with a pitch of 400 μm in an area of 30×30 cm^2 [78]. The μ-PIC has anode strips formed on one side of a polyimide board with a pitch of 400 μm and cathode strips orthogonally formed on the other side with the same pitch. Cathode strips have holes of 260 μm diameter and anode electrodes of 70 μm diameter are formed at the center of these holes. The schematic structure and photograph of μ-PIC shown in Figure B.1 and Figure B.2, respectively.
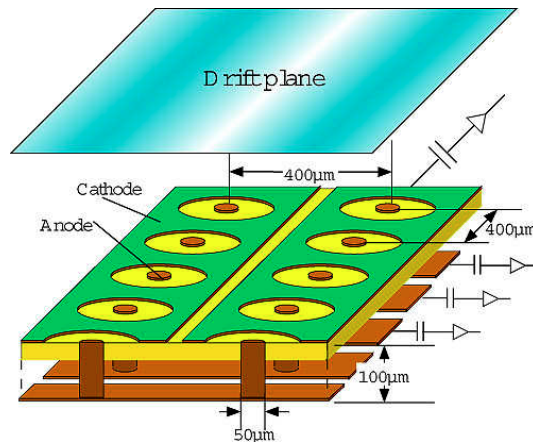
Figure B.1: Schmatic structure of μ-PIC.

Signals of pixels are read out through both anode strips and cathode strips. The μ-PIC is made by the PCB (Print Circuit Board) Technology so that it has a hardness against a discharge and a potential of mass production at a low cost. We achieved a maximum gas gain of 15,000 and a gas gain for a stable operation of 6,000 with a μ-PIC and a gas mixture of argon and ethane. The non-uniformity of the gas gain is about 5% by sigma in an area
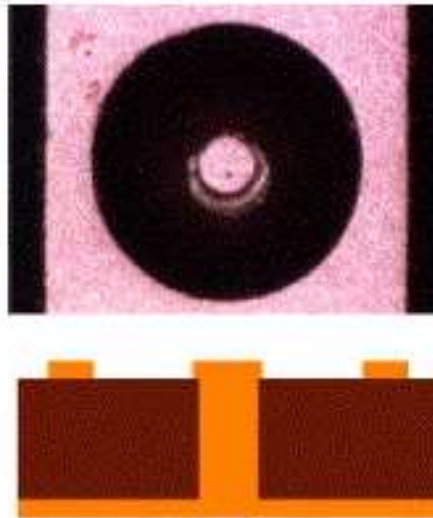
Figure B.2: Photograph (top) and sectional side view (bottom) of a pixel of μ-PIC.

of 10×10 cm^2. The energy resolutions for an X-ray are 23% and 30% (FWHM) at 5.9 keV with an area of 1.25×1.25 cm^2 and 10×10 cm^2, respectively. The best spatial resolution of the μ-PIC for taking an X-ray image was 120μm with a gas mixuture of Xe and CO$_2$.

B.2 μ-TPC

Miuchi et al. [93] reportsed performances of a μ-TPC with a detection volume of 232831 cm3 with a gas mixuture of argon and ethane. The μ-TPC was operated at a gas gain of 50,000, using the GEM as preamplifier, and an energy resolution of 60% FWHM at 60 keV was measured. A three-dimensional position resolution of against MIPs was 0.51 mm (FWHM). More deteails are described in [93]. For CF$_4$ gas a three-dimensional position resolution of 0.80 mm (FWHM) against α-particle was obtained in the NEWAGE-0.3a detector.

Bibliography

[1] C. L. Bennet, *et al.*, ApJ **583** (2003) 1; C. L. Bennet, *et al.*, ApJS **148** (2003) 1; J. Dunkley, *et al.*, ApJS, arXiv 0803.0586

[2] D. Tytler, J. M. O'Meara, N. Suzuki and D. Lubin, Physica Scripta **T85** (2000) 12

[3] R. A. Knop *et al.*, Astrophys. J. **598** (2003) 102

[4] A. W. Allen, R. W. Shmidt and A. C. Fabian, MNRAS **334** (2002) L11

[5] M. Tegmark *et al.*, Phys. Rev. D **69** (2004) 103501

[6] K. G. Begeman, A. H. Broeils and R. H. Sanders, MNRAS **249**(1991) 523

[7] R. P. Olling, MNRAS **311** (2000) 361

[8] J. Caldwell and J. P. Ostrinker, Astrophys. J. **251**(1981) 61

[9] R. A. C. Croft, W. Hu, and R. Dave Phys. Rev. Lett. **83** (1999) 001092

[10] R. D. peccei and H. R. Quinn, Phys. Rev. Lett. **38** (1977) 1440

[11] Astalos *et al.*, Phys. Rev. D **69** (2004) 011101

[12] P. Sikivie, Phys. Rev. Lett. **51** (1983) 1415

[13] C. Eleftheriadis *et al.*, arXiv:0706.0637

[14] Y. Inoue, et al, Phys. Lett. B **668** (2008) 93

[15] G. Jungman, *et al.*, Phys. Rep. **267** (1996) 195

[16] G. Servant *et al.*, New J. Phys., **4** (2002) 9

[17] D. Majumdar, Phys. Rev. D. **67** (2003) 095010

[18] J. D. Vergados, hep-ph/0610017

[19] U. Amaldi *et al.*, Phys. Lett. B **260** (1991) 447

[20] A. Bottino, *et al.*, Phys. Rev. D, **72** (2005) 083518

[21] F. Donato, *et al.*, Phys. Rev. D, **78** (2008) 043506

[22] K. Abe *et al.*, Phys. Lett. B, **670** (2008) 103

[23] H. Fuke, *et al.*, Phys. Rev. Lett. **95** (2005) 081101

[24] P. Picozza, *et al.*, PAMELA Astropart. Phys. **27** (2007) 296

[25] O. Adriani, *et al.*, astro-ph:0810.4995.

[26] T. Delahaye, *et al.*, Phys. Rev. D, **77** (2008) 063527

[27] J. E. Koglin, *et al.*, Journal of Physics Conference Series **120** (2007) 042011

[28] S. D. Hunter, *et al.*, Astrophys. J. **481** (1997) 205

[29] D. Elsaesser and K. Mannheim, Phys. Rev. Lett. **94** (2005) 171302

[30] GLAST Facility Science Team, Astropart. Phys. **11** (1999) 277

[31] The Super-Kamiokande Collaboration, Phys. Rev. D **70** (2004) 083523

[32] R. Matias *et al.*, Phys. Rev. D. **76** (2007) 033003

[33] Nucl. Phys. B. Pro.Suppl. 173 (2007) 79

[34] G. Abbiendi, *et al.*, Eur. Phys. J. C35 (2004) 1

[35] A. Gabutti, *et al.*, Astropart. Phys. **6** (1996) 1

[36] CDF Collaboration, Phys. Rev. Lett. **99** (2007) 121801

[37] M. Nojiri *et al.*, JHEP **0603** (2006) 063

[38] J. D. Lewin and P. F. Smith, Astropart. Phys. **6** (1996) 87

[39] K. M. Cudworth, Astron. J. **99** (1990) 590

[40] C. S. Kochanek, Astrophys. J. **457** (1996) 228

[41] J. Ellis, *et al.*, Phys. Lett. B **481** (2000) 304

[42] A. k. Drukier *et al.*, Phys. Rev. D **33** (1986) 3495

[43] D. N. Spergel, Phys. Rev. D **37** (1988) 1353

[44] C. J. Copi and L. M. Krauss Phys. Rev. D **63** (2001) 043507

[45] R. Bernabei *et al.*, Phys. Lett. B **424** (1998) 195; **450** (1999) 448; **480** (2000) 23; Riv. N. Cim. 26 n.1. (2003) 1-74

[46] B. Bernabei, *et al.*, Eur. Phys. J. C. **56** (2008) 56

[47] G. J. Alner *et al.*, Phys. Lett. B **616** (2005) 17

[48] H.S.Lee *et al.*, Phys. Rev. Lett. **99** (2007) 091301

[49] Y. Shimuzu *et al.*, Phys. Lett. B **633** (2006) 195

[50] P. F. Smith and J. D. Lewin, Phys. Rept., **187** (1990) 203

[51] P. F. Smith et al, Phys. Lett. B, **255** (1991) 454

[52] N. J. C. Spooner, *et al.* Phys. Lett. B, **273** (1991) 333

[53] T. Shutt *et al.*, Phys. Rev. Lett., **69** (1992) 3425

[54] D. Akerib *et al.*, Phys. Rev. Lett., **93** (2004) 211301

[55] V.Sanglard *et al.*, Phys Rev. D **71** (2005) 122002

[56] D. S. Akerib *et al.*, Phys. Rev. D **73** (2006) 011102;
D. S. Akerib *et al.*, Phys. Lett. **96** (2006) 011302

[57] Z. Ahmed *et al.*, astro-ph/0802.3530

[58] S. Cebrian *et al.*, Phys. Lett. B **563** (2003) 48

[59] C. Angloher *et al.*, Astropart Phys **23** (2005) 325

[60] R. Bernabei *et al.*, Phys. Lett. B, **436** (1998) 379

[61] G. J. Alner *et al.*, Astropart. Phys. **23** (2005) 444

[62] A. Minamino, Doctor thesis of Tokyo university (2008)

[63] G. J. Alner *et al.*, Astropart. Phys. **28** (2007) 287;
V. N. Lebedenko *et al.*, arXiv0812.1150L

[64] J.Angle *et al.*, Phys. Rev. Lett. **101** (2008) 091301;
J.Angle *et al.*, Phys. Rev. Lett. **100** (2008) 021303

[65] P. Betti *et al.*, astro-ph/0701286

[66] S. Navas *et al.*, J. Phys. Conf. Ser. **110** (2008) 062019

[67] D. N. McKinsey *et al.*, Nucl. Phys B Pro. Suppl. **173** (2007) 152

[68] M. G. Boulay and A. Hime, arXiv:astro-ph/0411358v1

[69] E. Behnke, etr al., Sci. **319** (2008) 933

[70] T. A. Grard *et al.*, Phys. Lett. B **621** (2005) 233.

[71] M. Barnabe-Heider *et al.*, Phys. Lett. B **624** (2005) 186.

[72] G. J. Alner *et al.*, Nucl. Instrum. and Meth. A **555** (2005) 173

[73] B. Moprgan *et al.*, Phys. Rev. D **71** (2005) 103507

[74] D. Dujmic et al, Nucl. Instrum. Meth. A **584** (2008) 327

[75] T. Tanimori *et al.*, Phys. Lett. B **578** (2004) 241;

[76] J. Ellis, A. Ferstl, and K. A. Olive, Phys. Rev.D **63** (2001) 065016.

[77] J. F. Ziegler, J. P. Biersack and U. Littmark, SRIM - The Stopping and Range of Ions in Matter, Pergamon Press, New York, 1985.

[78] A. Takada *et al.*, Nucl. Instr. Meth. A **573** (2007) 195.

[79] F. Sauli and Sharma, Ann. Rev. Nucl. Part. Sci. **49** (1999) 341.

[80] H. Kubo *et al.*, IEEE Nuclear Science Symposium Conference Record 371-375 (2005) .

[81] http://www.chukoh.co.jp

[82] http://consult.cern.ch/writeup/magboltz/;

[83] A. Hitachi, Rad. Phys. and Chem. **77** (2008) 1311

[84] S. Agostinelli *et al.*, Nucl. Instr. Meth. A **506** (2003) 250;
J. Allisom *et al.*, IEEE Transaction on Nuclear Science **53** No.1 (2006) 270.

[85] K. Miuchi *et al.*, Phys. Lett. B **654** (2007) 58.

[86] SK Collaboration, Nucl. Instrum. Meth. A **501** (2003) 418.

[87] Master thesis of Tokyo university Ishizuka (2001)

[88] Master thesis of Tokyo university Minamino (2005)

[89] A. Green, Phys. Rev. D **65** (2001) 023520

[90] D. C. Kocher and J. S. Smith, "Radioactive decay data table:A hand book of decay data for application to radiation dosimetry and radiological assessments", Springfield, 1981

[91] A. Ochi, *et al.*, Nucl. Instr. and Meth. A 471 (2001) 264

[92] T.Nagayoshi, *et al.*, Nucl. Instr. and Meth. A 513 (2003) 277;
T.Nagayoshi, *et al.*, Nucl. Instr. and Meth. A 525 (2004) 20

[93] K. Miuchi *et al.*, Nucl. Instr. Meth. A **576** (2007) 43

List of Figures

LIST OF FIGURES

List of Tables